

Dissertation

submitted to the

Combined Faculties of the Natural Sciences and Mathematics
of the Ruperto-Carola-University of Heidelberg, Germany

for the degree of

Doctor of Natural Sciences

Put forward by

Roman Follert

born in: Eisenhüttenstadt

Oral examination: November 14th, 2011

**The atmospheric piston simulator
for LINC - NIRVANA**

and

**Interferometric observations of
massive young stellar objects**

Referees: Prof. Hans - Walter Rix
Prof. Andreas Quirrenbach

Abstract

The scope of this dissertation is two-fold. The first part describes the design, construction and verification of the atmospheric piston simulator. The atmospheric piston simulator is a device which will allow the verification of the LINC-NIRVANA fringe tracking system under as realistic as possible conditions. The design of the atmospheric fringe tracker is based on optical fibers for light guiding and integrated optics components for the manipulation of the phase of the transmitted light. This fiber based setup allows on the one hand an easy and reliable way to introduce differential piston sequences, on the other hand integration into LINC-NIRVANA will be trivial.

The second part of this dissertation describes the application of interferometry in the case of the observation of massive young stellar objects. Two objects are presented and discussed in detail: the Kleinmann & Wright object and AFGL 2136. The interferometric measurements as well as the data reduction are described. The spectrally dispersed visibility curves and the differential phase data are fitted by analytical geometrical models. Then, the interferometric data and results from a spectral energy distribution analysis are combined and compared to Monte Carlo radiative transfer simulations. The results of this analysis indicate the existence of circumstellar disks similar to those found in low mass star formation. A detailed analysis of the mid-infrared silicate absorption features also indicates significant dust grain evolution in AFGL 2136.

Zusammenfassung

Der Inhalt dieser Dissertation ist zweigeteilt. Der erste Teil beschreibt das Design, den Aufbau und die Verifikation des atmospheric piston simulator. Der atmospheric piston simulator ist ein Instrument mit dessen Hilfe die fringe tracking Einheit von LINC-NIRVANA unter möglichst realistischen Bedingungen im Labor getestet und verifiziert werden soll. Sein Design beruht auf optischen Glasfaserkabeln zur Lichtleitung und aktiven integrierten Optiken zur Manipulation der Phase des übertragenden Lichtes. Diese Konfiguration erlaubt es auf der einen Seite, direkt und zuverlässig differentielle Phasensequenzen zu erzeugen. Auf der anderen Seite erlaubt das Glasfaser basierte Design eine unkomplizierte Integration des atmospheric piston simulators in LINC-NIRVANA.

Der zweite Teil dieser Dissertation beschäftigt sich mit der Anwendung der Interferometrie im Falle der Beobachtung von jungen massereichen sternähnlichen Objekten. Zwei Objekte werden hierbei im Detail beleuchtet: Das Kleinmann & Wright Objekt und AFGL 2136. Es werden die interferometrischen Messungen sowie die Datenreduktion beschrieben. Zunächst werden analytische, geometrische Modelle an die spektral dispergierten Visibility Kurven und die differential phase Daten angepasst. Dann werden die interferometrischen Daten und die Ergebnisse einer Analyse der spektralen Energieverteilung kombiniert um sie anschließend mit Monte Carlo Strahlungstransportmodellen zu vergleichen. Die Ergebnisse legen die Existenz zirkumstellarer Scheiben nahe, ähnlich denen, die im Falle der Entstehung masseärmerer Objekte gefunden wurden. Eine detaillierte Analyse der Silikat Absorptionsbande legt außerdem eine Entwicklung der Staubteilchen in der Umgebung von AFGL 2136 nahe.

Contents

1	The atmospheric differential piston simulator - an Introduction	1
1.1	Atmospheric turbulence - Theory	1
1.2	Atmospheric differential piston and optical interferometry	3
1.3	Additional OPD variations - instrument vibrations	6
1.4	The Large Binocular Telescope	8
1.5	LINC-NIRVANA	9
1.5.1	Overview	9
1.5.2	The fringe tracking system	10
2	The atmospheric piston simulator for LINC-NIRVANA	12
2.1	The atmospheric piston simulator - Requirements	12
2.2	The atmospheric piston simulator - Concept	14
2.3	The piston simulator lab setup	16
2.3.1	General description	16
2.3.2	Detailed description of Parts	18
2.4	Control and readout of the atmospheric piston simulator	25
2.4.1	Software control of the EO-PMs and fiber stretchers	25
2.4.2	Software to create the piston sequences	25
2.4.3	Camera readout	26
2.4.4	Post-processing the detector frames	26
2.5	Calibration and verification of the lab experiment	30
2.5.1	Description of the calibration / verification experiments	30
2.5.2	A word on the achievable precision	31
2.5.3	Power spectra of noise floor	32
2.5.4	Stress induced birefringence by the fiber stretcher	33
2.5.5	Results	35
2.5.6	Verification of overall operations	37
2.6	Conclusions of the lab experiment	42
3	Fringe tracking verification	43
3.1	Improvements to the lab experiment	43
3.2	Preliminary experiments on the LINC-NIRVANA bench	44
3.3	Interfaces on the LINC-NIRVANA optical bench	45
3.3.1	LINC-NIRVANA MAPS	45
3.3.2	LINC-NIRVANA calibration unit	46
3.3.3	A distinct opto-mechanical post	47
3.4	Verification scenarios	47
3.5	Fringe tracking verification - the end?	48

4	Massive young stellar objects and interferometry	49
4.1	Formation of high mass stars	49
4.2	IR interferometry for assessing small spatial scales	50
4.3	Review of recent results	52
4.3.1	MWC 297	52
4.3.2	IRAS 13481-6124	52
4.3.3	NGC 2264 IRS1	52
4.3.4	M8E-IR	54
4.3.5	W33A	54
5	The Kleinmann - Wright object	55
5.1	Introduction to the Kleinmann - Wright object	55
5.2	Observations and data reduction	56
5.3	Analysis of the spectral and interferometric data	60
5.3.1	SED fitting	60
5.3.2	Radiative transfer modeling and synthetic visibilities	62
5.3.3	Interferometric observations	64
5.4	Discussion	65
5.4.1	Statistical reduction of the parameter volume for the SED fits	65
5.4.2	Object models from the SED Fitting	67
5.4.3	General discussion of the visibilities	68
5.4.4	Comparison between modeled and measured visibility curves	72
5.5	Conclusions	75
6	AFGL 2136	76
6.1	Introduction to AFGL 2136	76
6.2	Observations and data reduction	77
6.2.1	Interferometric observations	77
6.2.2	Spectra and SED compilation	81
6.3	SED fitting and statistical interpretation	84
6.3.1	SED fitting	84
6.3.2	Object models from the SED Fitting	85
6.3.3	Statistical reduction of the parameter volume	88
6.4	Dust growth in AFGL 2136	90
6.4.1	Fitting the silicate absorption features	90
6.4.2	Grain growth in the circumstellar environment of AFGL 2136	91
6.5	Interpretation of the interferometric observations	96
6.5.1	Fitting simple geometric shapes	96
6.5.2	Radiative transfer modeling and synthetic visibilities	96
6.5.3	Results from simple model fitting	97
6.5.4	Shift of the photo center	101
6.5.5	Comparison between modeled and measured visibility curves	103
6.6	Conclusions	106
7	Outlook	107
	Acknowledgments / Danksagung	115

List of Figures

1.1	Median C_n^2 profile for Mt. Graham.	2
1.2	Median wind speed for Mt. Graham.	2
1.3	Power spectra of differential atmospheric piston.	5
1.4	Preliminary results from the OVMS.	6
1.5	The Large Binocular telescope.	8
1.6	Picture of the LBT dome.	8
1.7	Mechanical design of LINC-NIRVANA	9
1.8	Model of LINC-NIRVANA	10
1.9	Mechanical design of the LINC-NIRVANA fringe tracker system.	11
2.1	Conceptual layout of the lab setup.	14
2.2	Schematics of the atmospheric piston simulator lab setup.	16
2.3	Panoramic picture of the lab setup.	16
2.4	Filter system of the LINC-NIRVANA fringe tracking system.	18
2.5	Measured fringe contrast versus OPD.	18
2.6	The semiconductor laser light source.	18
2.7	Picture of the Y-coupler	19
2.8	The polarization controller.	19
2.9	Picture of the electro-optical phase modulators	21
2.10	The two fiber stretchers.	21
2.11	One of the fiber collimators.	22
2.12	Fiber collimator attached to a linear stage.	22
2.13	The 90°reflective prism.	22
2.14	Customized aperture mask.	22
2.15	Reflective prism, aperture mask and first lens.	23
2.16	Overview of the imaging optics.	23
2.17	Front of the “Blinking diode”.	24
2.18	The infrared detector.	24
2.19	Screen shot of the full detector area.	24
2.20	Subframe as obtained by the Camera Link data acquisition.	27
2.21	Fit of the incoherent PSF.	27
2.22	Sequence of the mean intensity of the blinking diode.	28
2.23	Example of fringe fitting.	28
2.24	Fitted phase sequence.	29
2.25	Example of a Fourier amplitude spectrum.	29
2.26	Amplitude spectra of the noise floor.	32
2.27	Comparison between parallel and crossed linear polarization filters.	34
2.28	Pixel variation for the polarizing experiment.	34
2.29	Calibration of the amplifier gain.	35

2.30	The calibration curves for the two EO-PMs.	36
2.31	The calibration curves for the two fiber stretcher.	36
2.32	The calibration curves for two devices operating in parallel.	38
2.33	Comparison of two piston sequences.	38
2.34	Comparison of two Fourier amplitude spectra.	39
2.35	Comparison of the anticipated and the measured piston sequence (theoretic power spectrum).	39
2.36	Comparison of the Fourier power spectra of the anticipated and measured sequence (theoretic power spectrum).	40
2.37	Comparison of the anticipated and the measured piston sequence (measured power spectrum).	40
2.38	Comparison of the Fourier power spectra of the anticipated and measured sequence (measured power spectrum).	41
3.1	Concept of the “zero OPD” preliminary experiment.	44
3.2	Concept of LINC-NIRVANA MAPS.	45
3.3	Design of MAPS.	46
3.4	MAPS and the calibration unit on the LINC-NIRVANA optical bench.	46
3.5	LINC-NIRVANA calibration unit.	47
3.6	Concept for a zero OPD absolute reference.	48
4.1	Zoom in on IRAS 13481-6124.	53
5.1	iJHKs images of the KW region.	55
5.2	Photometry of the KWO.	56
5.3	Correlated fluxes KWO.	58
5.4	Radial cuts of image profiles of the KWO and the calibrator star.	59
5.5	Best SED fits.	61
5.6	RGB composite model image.	63
5.7	Calibrated visibility curves (KWO).	64
5.8	Distribution of the stellar mass.	65
5.9	Distribution of the stellar temperature.	65
5.10	Distribution of the envelope accretion rate	66
5.11	Distribution of the disk mass.	66
5.12	Distribution of the Disk inner radius.	67
5.13	Fit of a 1D Gaussian to the visibility amplitudes.	69
5.14	Comparison of the observed and synthetic visibilities (I).	70
5.15	Comparison of the observed and synthetic visibilities (II).	71
6.1	RGB composite images of AFGL 2136.	76
6.2	Correlated fluxes (AFGL2136).	79
6.3	Calibrated visibility curves (AFGL2136).	79
6.4	Uncalibrated differential phases (AFGL 2136).	80
6.5	Data from the Keck segment tilting experiment.	81
6.6	N- band spectra of AFGL 2136.	82
6.7	Compiled SED for AFGL 2136.	82
6.8	Best fitting SEDs (AFGL2136).	84
6.9	Distribution of the stellar mass.	88
6.10	Distribution of the stellar temperature.	88

6.11	Distribution of the envelope accretion rate.	89
6.12	Distribution of the disk mass.	89
6.13	Distribution of the disk inner radius.	89
6.14	Distribution of the inclination angle.	89
6.15	The spectrum of AFGL 2136 between $7 \mu\text{m}$ and $27 \mu\text{m}$	90
6.16	Fit of the $10 \mu\text{m}$ silicate absorption feature.	91
6.17	a_{min}/p probability plane ($10 \mu\text{m}$ feature).	92
6.18	a_{max}/p probability plane ($10 \mu\text{m}$ feature).	92
6.19	a_{min}/a_{max} probability plane ($10 \mu\text{m}$ feature).	93
6.20	Fit of the $18 \mu\text{m}$ silicate absorption feature.	93
6.21	a_{min}/p probability plane ($18 \mu\text{m}$ feature).	95
6.22	a_{max}/p probability plane ($18 \mu\text{m}$ feature).	95
6.23	a_{min}/a_{max} probability plane ($18 \mu\text{m}$ feature).	95
6.24	RGB composite model image for AFGL 2136.	97
6.25	Fit of 2D- Gaussian to MIDI data.	98
6.26	(u, v)- plane fits of simple analytic models.	99
6.27	Photo center shift of AFGL 2136.	101
6.28	Concept of photo center shift.	102
6.29	Comparison of interferometric data with MC RT models.	103
6.30	Comparison of the observed and synthetic visibilities.	105

Chapter 1

The atmospheric differential piston simulator - an Introduction

The first part of this thesis covers the design, integration and verification of an atmospheric differential piston generator to be used as a tool for the verification of the fringe tracking system of LINC-NIRVANA. This chapter gives a general introduction to atmospheric induced aberrations, with differential piston as a special case and its theoretical description. Since the atmospheric differential piston simulator will be used to test the capabilities of its fringe tracking system, there is as well a brief introduction to this system and to LINC-NIRVANA.

1.1 Atmospheric turbulence - Theory

The light emitted by distant objects astronomers want to observe - be it galaxies, stars or even the planets around other stars - can be considered to consist of perfectly plane-parallel wavefronts (planes of common phase). Then, the light has to pass through Earth's atmosphere, if the objects in question are to be observed with ground-based observatories. The atmosphere has a highly inhomogeneous and fluctuating temperature, pressure and density distribution. Thus, the index of refraction varies temporarily as well as spatially. Due to this inhomogeneous nature of the atmosphere, the wavefront is distorted during transmission, which leads to optical aberrations in the imaging system (i.e. the telescope and its systems). However, the real problem is, that the atmosphere is not only inhomogeneous on the respective spatial scales, but also evolves in a turbulent way. Thus, in order to achieve diffraction-limited images on long integration times (to see fainter objects), an active compensation of this effect is required.

To describe this effect theoretically, a statistical description of its spatial and temporal properties is necessary. To describe the spatial statistics of the turbulence, Kolmogorov ([Tatarskii 1971](#)) came up with a simple concept: energy is introduced to the system at large scales, cascades down to smaller and smaller spatial scales and finally dissipates as heat. The Kolmogorov model is valid only in between the outer and inner spatial scale. Extensions of the model, e.g. the von Karman model ([Glindemann 2011](#)) and references therein), take into account specific inner and outer spatial scales (l_0 and L_0 , respectively), and introduce smooth transitions at these boundaries to alleviate discontinuities ([Conan et al. 1995](#); [Glindemann 2011](#)). Assuming Kolmogorov turbulence, equation 1.1 gives the phase spatial power

spectrum (Conan et al. 1995; Glindemann 2011):

$$W_{\Phi}(\mathbf{k}) = 0.033(2\pi)^{-\frac{2}{3}} \left(\frac{2\pi}{\lambda}\right)^2 C_n^2(h) dh k^{-\frac{11}{3}}, \quad (1.1)$$

where \mathbf{k} is the spatial frequency in a horizontal, turbulent layer of the atmosphere. The factor $C_n^2(h)dh$ describes the turbulence strength of a particular layer of the atmosphere at a height h and of thickness dh . $C_n^2(h)$, also known as the refractive index structure function, is an empirical measure, and differs for each observatory site. Fig. 1.1 depicts the median $C_n^2(h)$ for measurements at Mt. Graham (Masciadri et al. 2010). Two main distributions can be identified: the ground layer and an extended region in the upper Troposphere. The existence of separate layers of turbulence was found for various observatory sites.

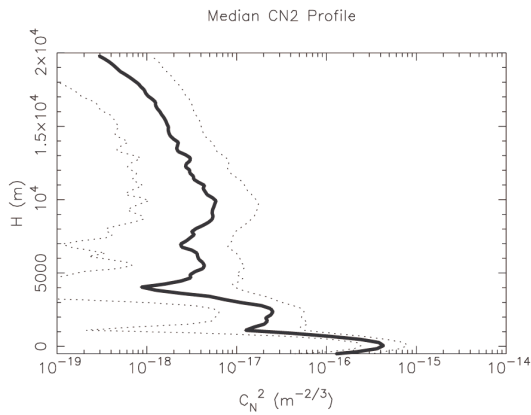


Figure 1.1: Median C_n^2 profile for Mt. Graham (Masciadri et al. 2010).

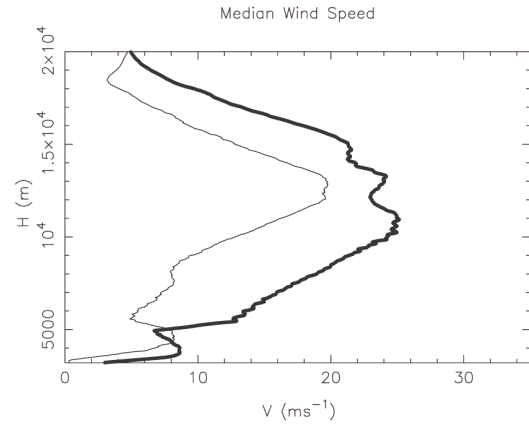


Figure 1.2: Median wind speed for Mt. Graham (Masciadri et al. 2010). The bold line depicts the median wind speed for the winter period, the thin line the median wind speed for the summer period.

To describe the temporal behavior of the turbulence, one applies the Taylor hypothesis of frozen turbulence. The Taylor hypothesis assumes that the phase screen as a whole is moved by a wind with speed \mathbf{v} without changing its apparent shape. Applying the Taylor hypothesis, one can show that $\omega_G(\nu)$, the temporal power spectrum as a function of frequency ν , is a function of $C_n^2(h)dh$, \mathbf{v} , and the shape of the aperture of the imaging optical system.

$$\omega_G(\nu) = \frac{1}{\bar{v}} \int_{-\infty}^{\infty} \left| \tilde{M}_G\left(\frac{\nu}{\bar{v}}, f_y\right) \right|^2 W_{\Phi}\left(\frac{\nu}{\bar{v}}, f_y\right) df_y, \quad (1.2)$$

$$\bar{v} = \left[\frac{\int v^{\frac{5}{3}}(h) C_n^2(h) dh}{\int C_n^2(h) dh} \right]^{\frac{3}{5}} \quad (1.3)$$

where $W_{\Phi}(\frac{\nu}{\bar{v}}, f_y)$ is the spatial power spectrum as defined above, \bar{v} is the effective wind speed and $\tilde{M}_G(\frac{\nu}{\bar{v}}, f_y)$ is the Fourier transform of a function describing the aperture of the system.

Fig. 1.2 shows measurements for the median wind speed above Mt. Graham. There is a layer with wind speeds above 25 m/s at a height of ≈ 12 km. On the other hand, the wind speed in the ground layer, which contributes more to the effective turbulence (see Fig. 1.1)

is less than 10 m/s on average.

Formula 1.2 gives a very general description of the temporal power spectrum of the distortion of the wavefront as seen by an aperture. For practical purposes, the shape of the wavefront is expanded in a set of orthogonal functions in the analysis of optical systems. The most common choice for this orthogonal basis are the Zernike polynomials (Born & Wolf 1999). A great advantage of Zernike polynomials is that the lowest order modes can be directly interpreted as commonly known optical monochromatic aberrations. For example, the two first orders are associated with the tip and tilt of the wavefront, the next higher modes are associated with defocus, spherical aberration, coma and astigmatism. The 0th order is called the piston mode, and it describes a general phase shift of the wavefront as whole.

For a single aperture system, only the orders > 1 are important, since a general phase shift will not be recognized by the detector. In modern astronomical observatories (like the Large Binocular Telescope or LBT), adaptive optics (AO) systems try to control the aberrations induced by the turbulent atmosphere. A dedicated wavefront sensor (Shack-Hartmann (Hardy 1998), curvature (Hardy 1998) or pyramid (Ragazzoni 1995)) measures the distortion of the incoming wavefront. The resulting information is then sent to a deformable mirror, which is bent such that the wavefront after reflection is flattened. Thus, the optical aberrations are reduced and almost diffraction limited images are possible.

1.2 Atmospheric differential piston and optical interferometry

As described above, the distortion of the wavefront induced by the turbulent atmosphere can be reduced with AO systems such that diffraction limited images are possible. Yet, all of the above wavefront sensing systems (Shack-Hartmann, curvature and pyramid sensors) do have in common that they are not able to track the first order Zernike mode - the piston mode. While this mode does not affect single dish imaging instruments, it has a serious effect on interferometry.

In optical interferometry in astronomy, the light emitted by an object is observed by two or more telescopes simultaneously. The light of the two telescopes is then directed to an optical lab, where it is brought to interference. The differential atmospheric piston describes the difference in piston mode between the two apertures introduced by the turbulent atmosphere. Thus, it represents an additional, temporally-varying phase component. This additional phase term leads to a spatial (or temporal in the case of Michelson (coaxial) interferometers) shift of the interferometric fringes. Due to the temporal variability, this leads to a blurring of the interferometric image in image plane interferometers like the LBT, or to a degradation of the coherent flux, which is the main observable in Michelson interferometers like the Very Large Telescope Interferometer (VLTI). Vibrations of the telescope and observatory structure are another source of differential piston variations (see section 1.3)

Therefore, modern optical interferometers need not only to be equipped with an AO system (in order to reduce the higher order Zernike modes), but also with a system that is capable of tracking differential piston. Such systems are called fringe trackers. A short introduction to the fringe tracking system for LINC-NIRVANA at the LBT will be given later (see section 1.5.2).

Conan et al. (1995) derive as a temporal power spectrum for the differential piston of a 2

aperture system:

$$\omega_{piston}(\nu) = \frac{4}{v} \int_{-\infty}^{\infty} \left[\frac{J_1(\pi D q)}{\pi D q} \right]^2 W_{\Phi}(q) df_y, \quad (1.4)$$

$$q = \sqrt{(\nu/v)^2 + f_y^2},$$

$$\omega_{\text{fringe motion}}(\nu) = 4 \sin^2\left(\frac{\pi B \nu}{v}\right) \omega_{piston}(\nu), \quad (1.5)$$

where D is the diameter of a single aperture, ν is the temporal frequency, \bar{v} is the effective wind speed and f is the spatial frequency. Equation 1.4 describes the temporal power spectrum of the piston mode for a single aperture system, $W_{\Phi}(q)$ is the spatial power spectrum of the turbulence (here: Kolmogorov) and equation 1.5 finally describes the temporal power spectrum of the differential piston mode for an optical interferometer with two circular apertures. B is the baseline called amplitude of the spatial vector connecting the centers of the two apertures.

Equation 1.5 can be approximated by three asymptotic power laws (Conan et al. 1995):

$$\omega_{\text{fringe motion}}(\nu) \propto \begin{cases} \nu^{-\frac{2}{3}} & \nu < \nu_{c1} \\ \nu^{-\frac{8}{3}} & \nu_{c1} < \nu < \nu_{c2} \\ \nu^{-\frac{17}{3}} & \nu > \nu_{c2} \end{cases} \quad (1.6)$$

The cutoff frequencies ν_{c1} and ν_{c2} are determined by the aperture geometry and the effective wind speed:

$$\nu_{c1} \approx 0.2 \frac{\bar{v}}{B} \quad (1.7)$$

$$\nu_{c2} \approx 0.3 \frac{\bar{v}}{D} \quad (1.8)$$

Thus, one can approximately describe the atmospheric differential piston knowing only 4 quantities: the baseline of the interferometer B , the single aperture diameter D , the effective wind speed \bar{v} and some power ω_{c1} at some minimum frequency ν_{c1} . Note that this approximate solution averages over all possible wind directions. This solution has a discontinuity for $\nu \rightarrow 0$ due to the fact that the Kolmogorov spatial power spectrum has been used in the derivation. Glindemann (2011) notes that by introducing an outer scale of turbulence (e.g. by using the von Karman spatial power spectrum), equation 1.6 becomes:

$$\omega_{\text{fringe motion}}^{L_0}(\nu) \begin{cases} = 0.8 \left(1 + \left(\frac{\bar{v}}{\nu L_0} \right)^2 \right) \omega_{\text{fringe motion}}(\nu) & \text{if } \bar{v} \parallel B \text{ \& } \nu \ll \nu_{c1} \\ \propto L_0^{2/3} & \text{if } \bar{v} \perp B \text{ \& } \nu \ll \nu_{c1} \end{cases}$$

But, since a typical continuous integration for an interferometric observation does not exceed a few minutes (and thus a minimum frequency of 10^{-3} Hz), this effect usually does not effect normal observations (see also Glindemann 2011).

Fig. 1.3 depicts a comparison between observational data for the differential piston and theoretical predictions. The black curve depicts data taken by Walter Jaffe (private communication) of the differential piston signal obtained with the MIDI (**MID**-infrared **Interferometric** instrument) instrument installed at the VLTI observatory. The blue curve depicts a theoretical prediction of the differential piston power spectrum assuming a single aperture diameter

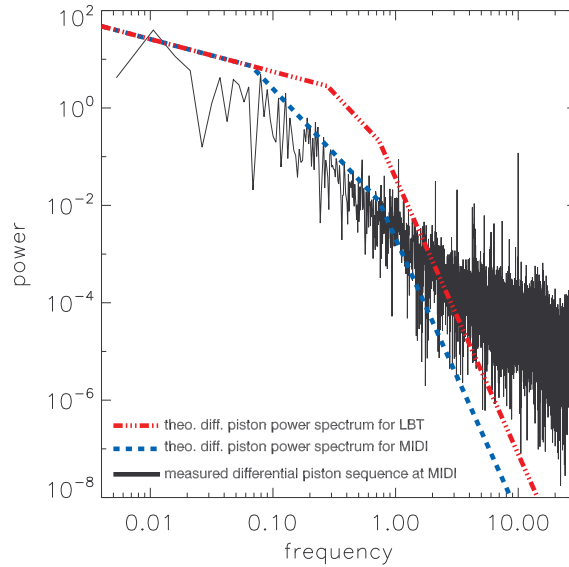


Figure 1.3: Power spectra of differential atmospheric piston. The black line depicts data taken with the MIDI instrument at the VLTI (W. Jaffe, private. communication), the red line a theoretical prediction for LBT and the blue line a theoretical prediction for the VLTI.

of $D=8.2$ m (the diameter of the unit telescopes at VLTI), a projected baseline of $B=60$ m and a moderate wind speed of $v=20 \frac{m}{s}$. The red line depicts a similar prediction for the LBT ($D=8.4$ m, $B=14.4$ m and $v=20 \frac{m}{s}$). The single dish aperture sizes of the LBT and the VLTI are approximately the same; thus, ν_{c2} is comparable for both observatories: $\nu_{c2}=0.73$ Hz. Since the aperture separation is larger for the VLTI, ν_{c1} is correspondingly smaller. Thus, according to theory, the VLTI would be less affected in general by atmospheric differential piston. On the other hand, Fig. 1.3 also shows the power spectrum of a measured piston sequence for comparison. At low frequencies, the theoretical predictions do fit the measurements quite well. For frequencies greater than $\nu_{c2}=0.73$ Hz though, the measured power spectrum shows significantly higher amplitudes. This might be partially due to vibrations as an additional source of differential piston variations. Nevertheless, the true origin of this remains unclear. This discrepancy led to the decision, that the atmospheric piston simulator should be capable of accepting both real piston measurements and theoretically modeled sequences.

1.3 Additional OPD variations - instrument vibrations

As mentioned in section 1.2, there is an additional source for OPD (**O**ptical **P**ath **D**ifference) variations: vibrations in the telescope structure. Any mechanical vibration of the optics can introduce a variation of the OPD, depending on the projection of the vibration direction onto the optical axis. Although the telescope and instrument structures are mechanically decoupled from the observatory building, there are still several sources which can induce vibrations. These include: changing wind load on the telescope structure, which is especially problematic if the main mirrors are pointing to a low elevation. In the case of the LBT (see section 1.4) one major source of instrumental vibration will be the adaptive secondary, which is attached to a moveable swing arm spider, presents a serious source of structural vibrations parallel to the light beams. Fans and pumps in cooling systems represent an additional source. For example, it was observed that the closed cycle coolers of LUCI I exhibit vibrations to the telescope structure as a whole. Finally, the movement of the telescope itself when changing the pointing can excite vibrations. The problem with mechanical vibrations is that their temporal power spectra are not limited to low frequencies (in which case they should be correctable by the fringe tracker and AO systems) as with the atmospheric turbulence induced effects. Instead, they can excite eigenvibrations of certain instrument structures with fairly high eigenfrequencies and amplitudes.

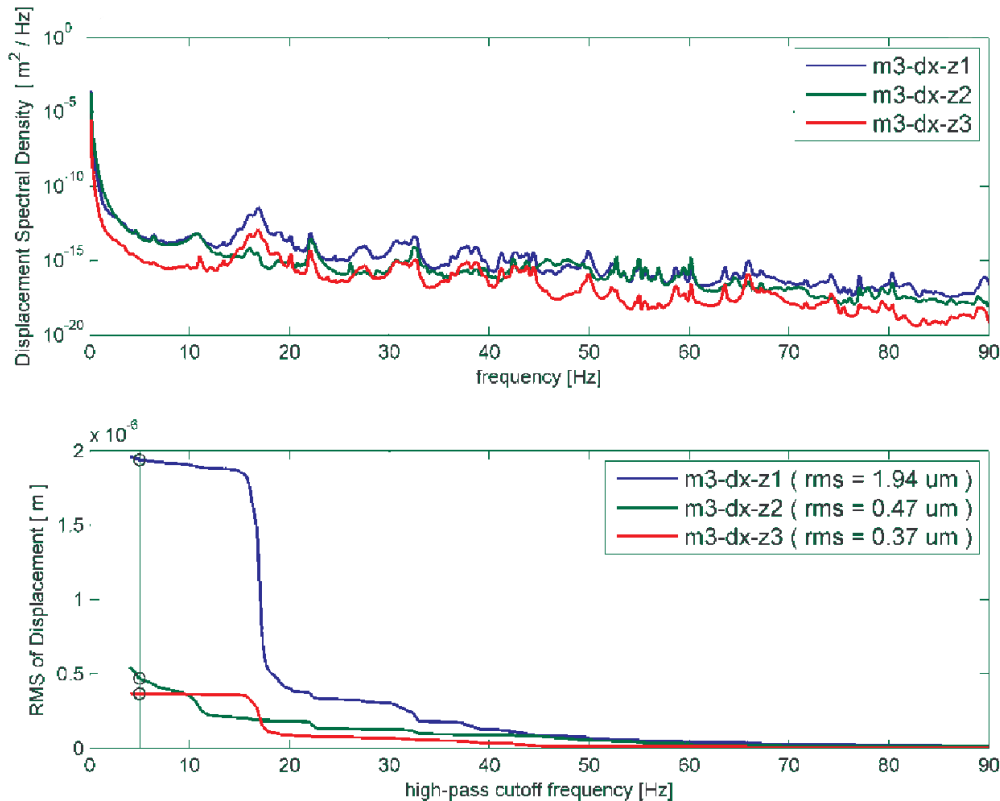


Figure 1.4: Preliminary results from the OVMS (J.U. Pott, private communication) of M3. Note that the associated power drops very quickly. High frequency modes can still be identified (e.g. at ≈ 18 Hz, $\approx 10^{-12} \frac{m^2}{Hz}$).

To identify the potential risk caused by telescope and instrument structure vibrations, an

OPD and Vibration Monitoring System (OVMS) is currently installed in a combined effort of the two interferometers of the LBT and the LBT observatory itself. For that purpose, 45 accelerometers in total will be attached to various positions on the telescope (e.g. 5 each primary, 5 to each secondary and tertiary). These accelerometers measure the acceleration in several axes of the telescope substructures. In fact, three of the accelerometers on each mirror are positioned such that their measurements allow to deduce the displacement of the mirror in the direction that is most critical for OPD changes. OPD changes in the frequency domain from 1 Hz to 250 Hz can then be derived from the sensor network. The special positioning and the capability to read out all accelerometers synchronously allows us to identify and quantify in real time the OPD variations due to vibrations. The OVMS will then serve as a feed-forward system for the LINC-NIRVANA fringe tracker system. The most recent discussion of the system can be found in Kürster et al. (2010). Fig. 1.4 depicts preliminary results from an internal technical note (J.U. Pott, private communication, 2011).

High frequency modes can be identified from Fig. 1.4. If one considers for example the peak at ≈ 18 Hz, then its spectral power density of $\approx 10^{-12} \frac{m^2}{Hz}$ can, in the worst case, be interpreted to cause an OPD variation of $\approx 2 \mu m$ (see as well lower inset of Fig. 1.4), which is significant at this high frequency (high observational frequencies with respect to fringe tracking). Note that this peak corresponds closely to the eigenfrequencies of the swing arm spiders.

Since the atmospheric piston generator is capable of generating its OPD control sequences from input power spectra, it will be possible to verify the response of the LINC-NIRVANA fringe tracking system to these effects by simply adding power spectra describing the atmospheric and vibrational effects.

The instrumental vibrations are an important source of OPD variations. The results obtained from OVMS will serve as an input for atmospheric piston simulator. This will allow us to take the effect of instrumental vibrations into account during the fringe tracking system verification.

1.4 The Large Binocular Telescope



Figure 1.5: The Large Binocular telescope. Picture taken by R. Follert April 2011.



Figure 1.6: Picture of the LBT dome (courtesy of Marc-André Besel), taken 2008. One can identify the two primaries and the two prime focus cameras LBTC blue and red. The central focal station was not populated in 2008. Currently, LUCI I is installed in the front left bent focal station and LBTI in the central part. LINC-NIRVANA will go in the rear part (front in the picture).

The Large Binocular Telescope (LBT) is one of the most modern optical observatories. It is situated on Mt. Graham (Arizona, USA) at an altitude of 3221 m. First light was obtained in October 2005 with the LBC blue prime focus camera. The LBT is unique due to its design: the two 8.4 m monolithic mirrors are mounted to a common alt-azimuth mount with a center-to-center separation of 14.4 m. This allows for various unique observation strategies. The primary mirrors were manufactured from boro-silicate glass in a novel spin cast technique and they can be aluminized in situ. In contrast to many other telescopes, the secondary mirror ($d=0.911$ m) acts as the deformable mirror for the adaptive optics system. There are five main focal stations for each primary: the prime focus, the direct Gregorian focus and three the bent Gregorian stations situated in between the primaries. Six first generation instruments are foreseen: LBC, LUCI, MODS, LINC-NIRVANA, LBT-I and Pepsii.

LBC consists two prime focus cameras, one optimized for operation in the blue part of the visual spectrum, and one optimized for the red part. LUCI comprises two identical multi-object near-infrared spectrometers / cameras, residing on the fixed LBT instrument platform. MODS also consists of two identical multi-object spectrographs-imagers but is optimized for operation in the visual and near-UV spectral range. The MODS units will be installed in the direct Gregorian focii of LBT. LINC-NIRVANA and LBT-I are the interferometric units working in the near-infrared (LINC-NIRVANA) and mid-infrared (LBT-I). They will ultimately make use of the specific two mirror design of the LBT by combining the light

from both primaries coherently. This will allow them to synthesize a telescope with $d=12$ m collecting area and the resolution of a 23 m primary. Finally, Pepsi is a high resolution Echelle spectrograph and polarimeter which is mainly intended to obtain very high resolution spectra from nearby stars. Currently (mid 2011), the 2 LBC units and one LUCI unit are installed, operational and open to the science community. One MODS unit and LBT-I are installed, but not yet open to science operation.

1.5 LINC - NIRVANA

Since one of the aims of this thesis is the development and verification of the atmospheric piston simulator, a device which will be used for the verification of the fringe tracking system of LINC - NIRVANA , this section gives a short introduction to LINC - NIRVANA and the fringe tracking system.

1.5.1 Overview

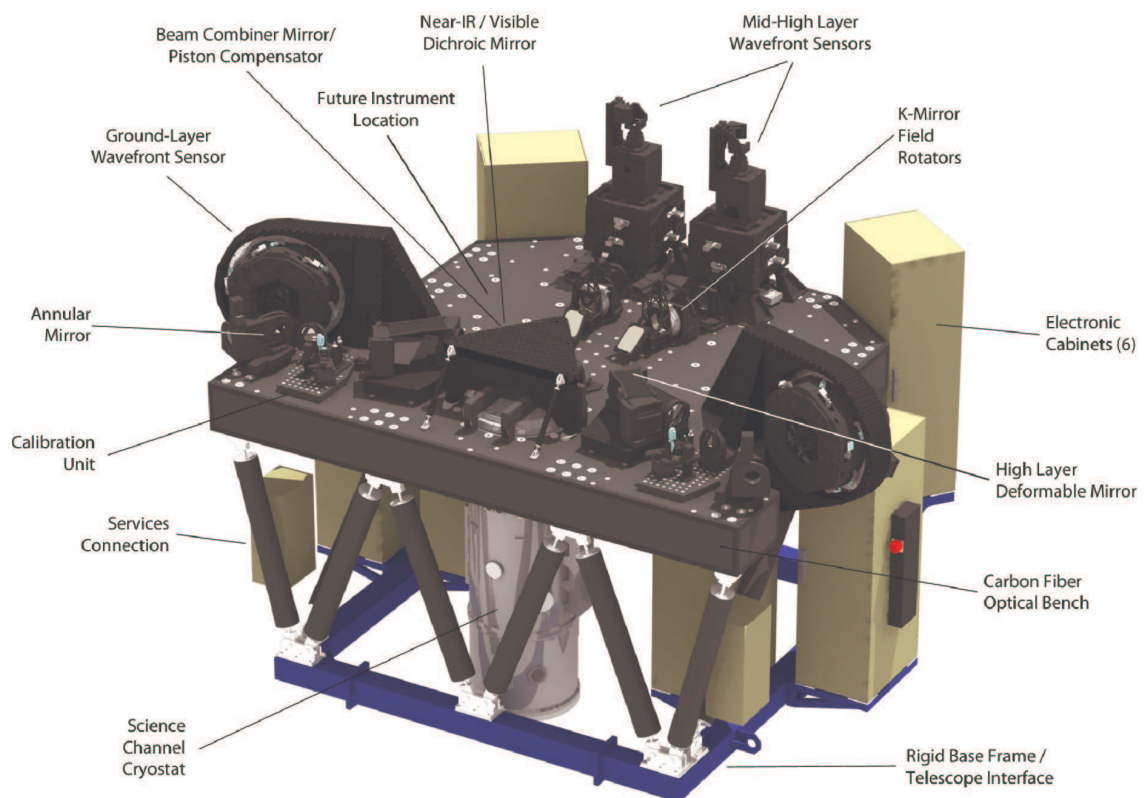


Figure 1.7: Mechanical design of LINC - NIRVANA (internal review document).

LINC - NIRVANA - principles of operation (**L**BT **I**nterferometric **C**amera - **N**ear - **I**R / **V**isible **A**daptive **i**nterferometer for **A**stronomy) will combine the light from both telescopes of the LBT in an image plane interferometer design in conjunction with advanced Multi-Conjugate Adaptive Optics (MCAO). Fig. 1.7 depicts LINC - NIRVANA . The light from the two LBT sides will enter LINC - NIRVANA through the annular mirrors, which redirect light from a field of view between 2 and 6 arcminutes to the Ground layer Wavefront Sensors (GWS).

The central 2 arcminutes are “quasi” collimated (resulting in an almost parallel beam with a very long focal length) by a lens system and directed toward the piston mirror. This mirror is capable of moving parallel to the beam direction and serves two purposes: To redirect the light downward toward the cryostat and to control the differential piston as measured by the fringe tracker. After reflection from the piston mirror, the light is split by a dichroic. The cold mask is inside the cryostat, which hosts a reflective Cassegrain camera and the fringe tracker detector. The visible part is reflected towards the Mid - high layer wavefront sensor.

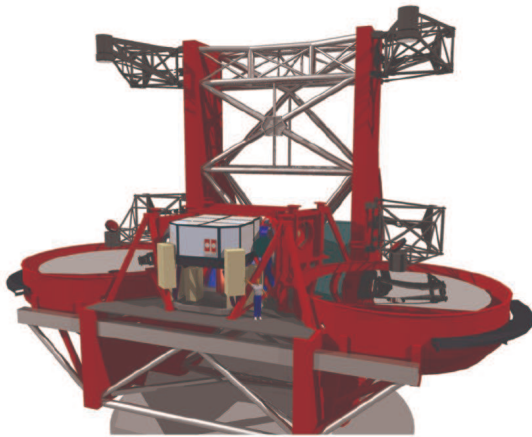


Figure 1.8: Model of LINC-NIRVANA on the shared instruments platform of the LBT (Herbst et al. 2010). Note the size of the human figure for scale.

the multi-conjugate, two layer adaptive optic system of the NIRVANA mode will allow a very homogeneous AO correction over the whole field of view. In addition, since it will make use of several natural guide stars at once, the sky coverage for observations will increase significantly. This will make wide field images with the spatial resolution of a 23 m aperture possible by attaining a very good sky coverage.

LINC-NIRVANA is currently in the AIV (Assembly, Integration and Verification) phase at the Max-Planck institute for astronomy (MPIA) in Heidelberg. LINC-NIRVANA is a collaborative project of the MPIA, INAF (Istituto Nazionale di AstroFisica, specifically Padova, Bologna, Arcetri and Roma), the MPI for Radio Astronomy (Bonn) and the University of Cologne.

1.5.2 The fringe tracking system

The fringe tracking system is crucial for stable interferometric operations of LINC-NIRVANA. It will freeze the fringe movement due to differential atmospheric piston and vibrations. The LINC-NIRVANA fringe tracker system is currently being built at the University of Cologne (Bertram et al. 2008; Bertram 2007). Delivery to the Max-Planck institute in Heidelberg is foreseen in 2012. After its integration into the LINC-NIRVANA cryostat, its performance in conjunction with the entire LINC-NIRVANA optics and mechanics will be tested and verified using the atmospheric piston simulator described in this thesis.

The fringe tracking detector will be integrated into the LINC-NIRVANA dewar (see Fig.

LINC-NIRVANA makes use of the LBT adaptive secondary while providing its own adaptive optics systems and is intended to produce images in the spectral range from $1.0 \mu\text{m}$ to $2.4 \mu\text{m}$. Due to its unique aperture, image reconstruction will be possible with only a few observations during a night. LINC-NIRVANA will synthesize a telescope with the sensitivity of a 12 m telescope and the spatial resolution of a 23 m telescope, over a field of view approximately 10 arcseconds square. LINC and NIRVANA are two different steps of implementation. First, the LINC mode will be implemented. It will only use the mid-high layer wave front sensor in a classical single guide star mode. This results in a spatially varying AO correction over the field of view and very limited sky coverage. In a second implementation phase,

1.9). In order to be able to use the full interferometric field of view of LINC - NIRVANA , the detector head must be able to move in the curved focal plane. This will increase the sky coverage for LINC - NIRVANA considerably as well. A filter wheel on the fringe sensor provides various filters for different operating modes (for the filter bands see section 2.3.2). The detector will regularly operate with frame rates of 200 Hz (up to 1 kHz) on a window that allows to sample the PSF (32×32 pixels). Since micro positioning at sub - pixel accuracy ($\approx 18 \mu\text{m}$) would be unfeasible in the cold over the required large travel range, the positioning mechanics are kept warm. They are placed underneath and are separated from the dewar environment by a moving baffle (Bertram 2007).

The fringe tracker will operate in a cophasing mode. The fringe motion is controlled such that the position of the zero OPD fringe, the so-called “white light fringe”, will be fixed on the science detector of LINC - NIRVANA . The resulting control signal is sent to the piston mirror, the actuator of the OPD control loop (Brix et al. 2010) (see also section 1.5).

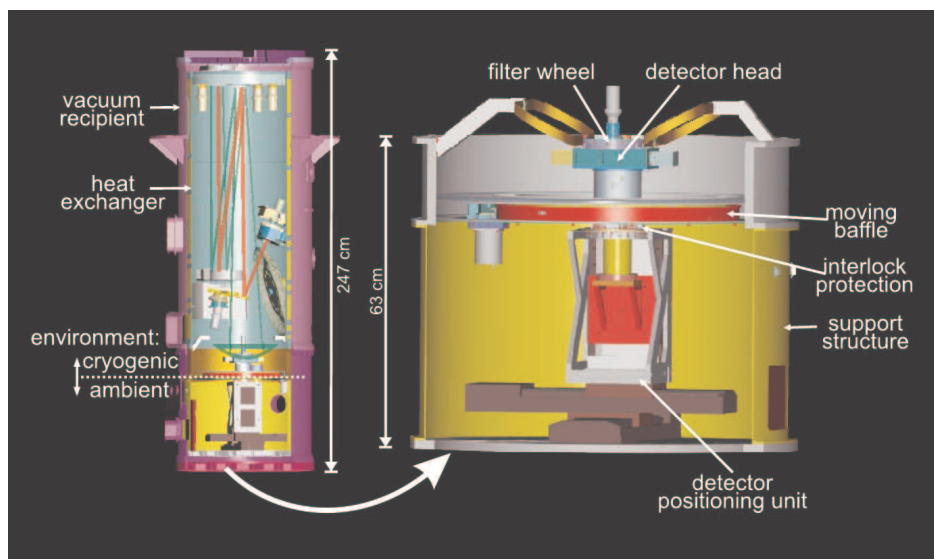


Figure 1.9: Mechanical design of the LINC - NIRVANA fringe tracking system and its position in the LINC - NIRVANA dewar (Bertram 2007).

Chapter 2

The atmospheric piston simulator for LINC - NIRVANA

The atmospheric piston simulator is a device which is designed and built as a tool for the verification of the fringe tracking system of LINC-NIRVANA . First, the general concept is presented which led to the design of the piston simulator. Then, the atmospheric piston simulator lab setup is described in detail. There is a summary of the control, data acquisition and data reduction software. The calibration of the atmospheric piston simulator is described and the results are presented. Finally, the operation of the atmospheric piston simulator is verified by specific experiments, and the performance is discussed in the conclusions section of this chapter.

Parts of this chapter have been published in [Follert et al. \(2010a\)](#).

2.1 The atmospheric piston simulator - Requirements

The atmospheric piston simulator is a device which shall serve as a tool for lab verification of the fringe tracking system of LINC-NIRVANA . It has to be able to simulate the atmospheric piston conditions on Mt. Graham as realistically as possible. At the same time, it should be flexible enough to permit the inclusion of other effects like piston variations caused by instrumental vibrations (see section 1.3). In order to conclusively verify the operations of the fringe tracking system, the atmospheric piston simulator should only generate differential piston sequences without introducing higher order optical aberrations. Finally, it is desirable to allow easy integration of the final setup into LINC-NIRVANA . This will permit the verification of the fringe tracking system operations in an advanced integration state of LINC-NIRVANA . These considerations lead to the requirements of the atmospheric fringe simulator.

There are no measurements of the atmospheric differential piston for the site of the LBT. Thus, the requirements presented here have to rely on a comparison to other observatory sites. The atmospheric piston simulator should be capable of modulating the differential phase with a maximum modulation amplitude of $\gtrsim 50 \mu\text{m}$ at low ($f \lesssim 1 \text{ Hz}$). The minimum required precision in generating the piston sequences is defined by the requirements posed on the fringe tracking system. The fringe tracking system has to be able to stabilize the fringe phase to better than $\Delta\Phi \approx \frac{\lambda}{10}$. Therefore, the atmospheric piston simulator needs to be able to introduce reliably phase shifts as small as $\Delta\Phi \approx \frac{\lambda}{50}$ to serve as a tool for the fringe tracking

system verification.

The atmospheric differential piston has only significant power below $f_{max} = 10 Hz$. But in order to be able to simulate other effects like instrumental vibrations, the atmospheric piston simulator has to operate at higher bandwidth. The requirements on the fringe tracking system (internal technical note) state that it has to be able to deal with vibrations up to 30 Hz. Thus, the atmospheric piston simulator should have an operating bandwidth of at least 300 Hz.

To summarize the requirements on the atmospheric piston simulator operations:

- min. addressable phase shift $\Delta\Phi = 0.02\lambda$
- max. achievable phase shift $\Delta\Phi \geq 50\lambda$
- modulation bandwidth $\Delta f = 300 Hz$

AO systems are routinely tested using rotating transparent phase screens in conjunction with additional optics (for example the PRIMA testbed (Abuter et al. 2006) or the atmospheric turbulence generator for LINC-NIRVANA s AO system (Meschke et al. 2010)). These plates, made from fused silica, are etched in a way that the thickness varies along the plate. Thus, the optical path through different sections of the plates varies. The optical path variations resemble those introduced by fluctuations of the index of refraction in the atmosphere. Although this concept has been proven to be successful in several experiments, it has a distinct drawback for testing the fringe tracking system of LINC-NIRVANA . Since the etched patterns vary smoothly across the plate surface, various orders of optical aberrations beyond pure piston will be introduced into the optical system. For a comprehensive, separate verification of the fringe tracking system, such behavior is not favorable. The number of modes introduced in this way could in principle be reduced by spatial filtering, but stable injection of light into the spatial filter (pinhole aperture mask or a single mode fiber) requires at least tip/tilt control, which requires the use of an AO system.

A fiber based setup is capable of providing all the desired general design aspects. Here, fiber based means that the light is transmitted throughout the setup by means of optical fibers. The modulation of the differential phase, the control of the output intensity, as well as the control of the polarization state of the transmitted light will be achieved by fiber optics components as well.

Integration on the LINC-NIRVANA optical bench will be trivial. There are various possible interfaces which are part of the general layout of the LINC-NIRVANA optical bench. The atmospheric piston simulator will not interfere with any of the structures on the LINC-NIRVANA optical bench, since no bulk optics are required.

Fiber based systems allow an accurate control of the phase of an optical system in a fiber. There are several devices which can achieve phase control, the most commonly used being fiber stretchers. Fiber stretchers usually consist of a central piezo element around which optical fibers are coiled up. If a voltage is applied to the piezo element, it will expand, thereby stretching the fibers slightly. This produces a change in OPD. These systems are, on the other hand, known to exhibit various problems due to the use of piezo elements, e.g. hysteresis effects, temperature sensitivity, and overshoot. An alternative to fiber stretchers are a new class of devices which just recently became publicly available: electro-optical phase modulators (EO-PMs). Details on the working principles of electro-optical phase modulators will be provided later (see 2.3.2). The phase modulation is achieved without the use of any

mechanically moving part. Thus, these devices can be controlled at up to GHz frequencies very accurately while achieving a very good repeatability.

2.2 The atmospheric piston simulator - Concept

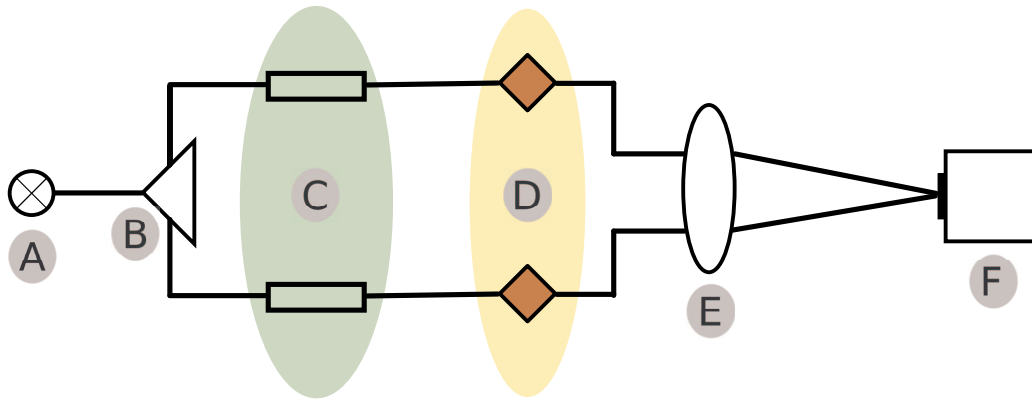


Figure 2.1: Conceptual layout of the lab setup.

- A Light source
- B Light splitter
- C High frequency / Low amplitude phase modulator
- D Low frequency / High amplitude phase modulator
- E Imaging optics
- F Detector

Figure 2.1 is a schematic representation of the anticipated design of the atmospheric piston simulator for LINC-NIRVANA. It consists of 2 major components. First, there is the light source and the fiber optics part (A, B, C, D). These components of the lab experiment should be designed to allow an easy integration onto the LINC-NIRVANA optical bench. They form the actual atmospheric piston simulator. The second component consists a bulk optics simple imaging system (E) and an infrared camera (F). This component is necessary for calibration and verification of the piston simulator in the lab. Eventually verification of the fringe tracking system of LINC-NIRVANA will be conducted with the optics of LINC-NIRVANA and the fringe tracking camera.

The following paragraphs provide additional details on the conceptual design of the piston simulator shall be described here in a little more detail. The actual atmospheric piston simulator lab setup will be presented in the appropriate section (see section 2.3.2).

There are only a few prerequisites concerning the light source. For the verification of the LINC-NIRVANA fringe tracking system, the warm and cold optics of LINC-NIRVANA will be used. Since the light has to pass through the LINC-NIRVANA filter system, there are in principle only few prerequisites upon the spectral composition of the light source. The light

sources should exhibit a tunable and continuous spectrum over the required near-infrared (JHK) bands. On the other hand, the LINC-NIRVANA filter system is not available for the calibration and verification of the atmospheric piston simulator in the lab. A light source with a sufficient coherence length (few tens of microns) will be needed for the verification of the piston simulator.

There are design prerequisites for the fiber optics components. First, it is desirable to set up the two interferometric arms symmetrically. This will reduce differential effects, e.g. differential chromatic dispersion. In addition, any static intrinsic optical path difference can only be actively adjusted within narrow limits (up to a few hundred micrometer). Thus, due to the limited coherence length of the light source (see Fig. 2.5), an equal optical path in the fiber in each arm is necessary in order to bring the light to interference. Finally, it is beneficial to be able to control and maintain the polarization state of the light in the fiber. In the worst case, the light which is ejected from the two fiber arms will have perpendicular polarization states and, therefore, does not interfere. Any other than an identical polarization state will degrade the fringe contrast within the coherence length.

It is worth mentioning that a fiber optics based setup also helps control cost of the piston simulator. Since the telecommunication industry has standardized on optical fibers at $1.3\ \mu\text{m}$ and $1.5\ \mu\text{m}$ (which suits J and H band operation, respectively), many of the parts can be purchased off-the-shelf from various companies.

2.3 The piston simulator lab setup

2.3.1 General description

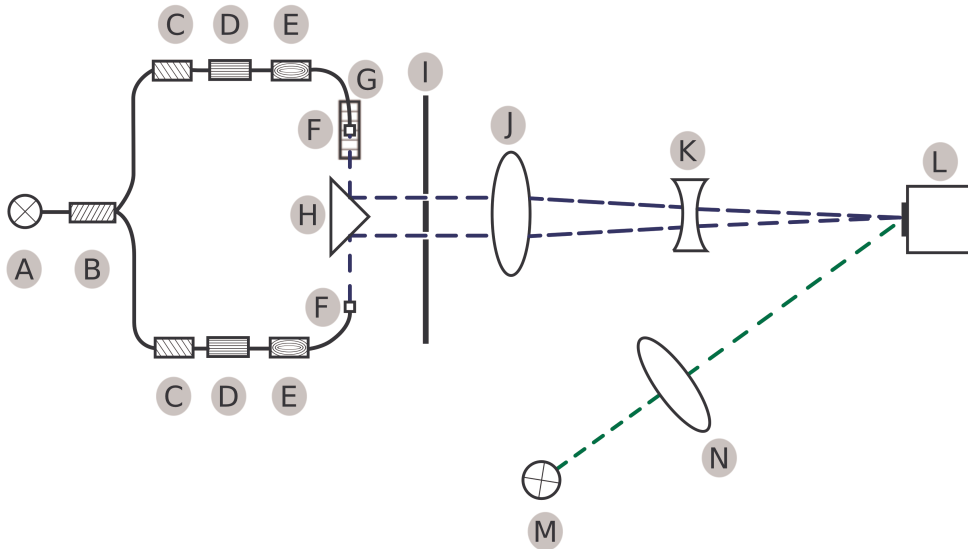


Figure 2.2: Schematics of the atmospheric piston simulator lab setup.

A	Light source	H	90°prism (reflective coating)
B	Fiber Y-coupler	I	Aperture mask
C	Fiber polarization controller	J	Lens, $f=500$ mm
D	Electro-optical phase modulators	K	Lens, $f=-50$ mm
E	Fiber stretcher	L	Detector
F	Fiber collimator	M	Blinking diode
G	Linear stage	N	Lens, $f=120$ mm

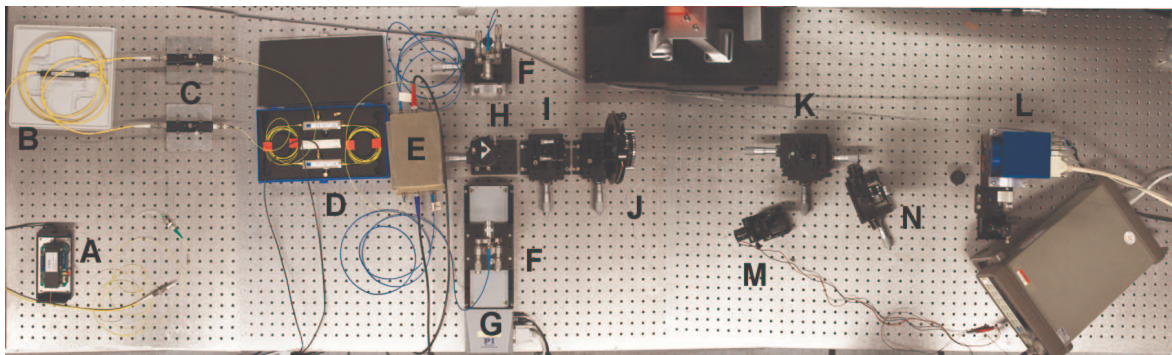


Figure 2.3: Panoramic picture of the lab setup. Note that the labels are same as in the schematics above (Fig. 2.2)

Figure 2.2 shows a schematic view of the lab setup, while Fig. 2.3 gives a panoramic view of the actual lab setup.

After injection of the light into the fiber by the light source (**A**), the light is directed by means of single mode fibers towards the 50/50 Y-coupler (**B**). Next, there is a fiber polarization controller (**C**) in each arm. The fiber polarization controller defines the polarization vector of the light prior to the input of the electro-optical phase modulators (**D**). From this point, all fibers are polarization maintaining. After the electro-optical phase modulators follow the fiber stretchers (**E**). The fiber stretchers output is prolonged by a single mode, phase maintaining patch cables of a few meters length. Finally, the light is ejected from the fibers by means of a pair of fiber collimators (**F**).

The ends of the optical fibers reside in the focii of fiber collimators. One of the fiber collimators is attached to a motorized linear stage (**G**), which can move along the beam axis. In this way, undesired intrinsic optical path mismatches can be accounted for in a quick and straightforward way. The collimated beams are reflected from a 90°prism with a reflective coating (**H**). Next, there is a custom aperture mask, which resembles the relative geometry of the LBT (**I**). This aperture mask defines the aperture stop of the system. The collimated beams then pass through a simple two lens imaging system (**J**, **K**) and are thereby focused on a common focal plane. In the focal plane resides the near-infrared detector (**L**), which is used for data acquisition.

In addition to the imaging optics, there is an extension to the lab setup. Using a single lens (**N**), an LED (**M**) behind a pinhole aperture is imaged onto the detector. The LED is driven by a frequency generator using a triangular wave pattern of 10 Hz. In this way, a physically-independent and precise time stamp is associated with each frame by later fitting a triangular wave to the mean intensity of the blinking diode.

2.3.2 Detailed description of Parts

The light source

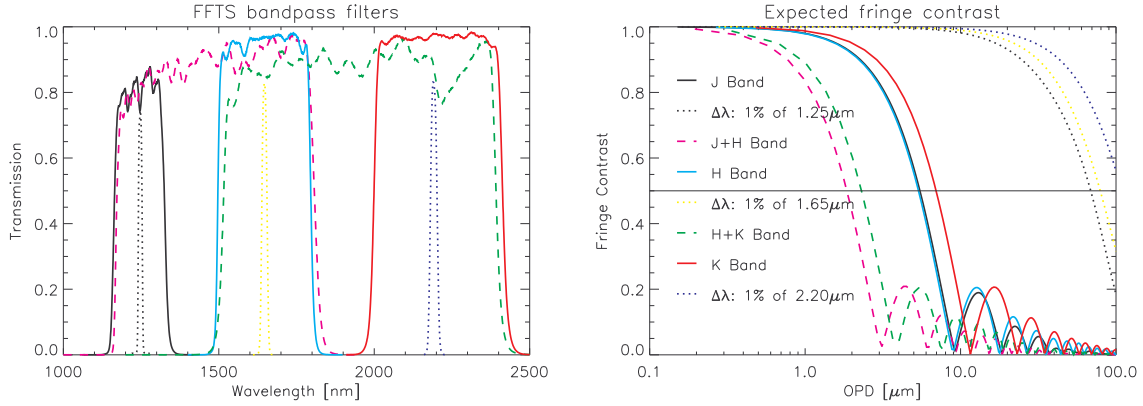


Figure 2.4: Filter system of the LINC-NIRVANA fringe tracking system and associated coherence length (Bertram et al. 2008).

The main light source used for the lab experiment is a semiconductor laser. The light is internally injected into a fiber, which eases the integration into the setup. Fig. 2.6 shows a picture of the light source. The light source is custom made by Exalos, and it operates at a central wavelength of $\lambda_c \approx 1.3 \mu\text{m}$.

There was minimal information on this light source provided by the manufacturer in the form of data sheets. Thus, it was characterized prior to the lab setup verification. In order to determine the coherence length of the light source, the degree of coherence (i.e. the visibility) was measured for different OPD shifts introduced by the fiber stretchers. The degree of coherence is determined by fitting equation 2.4 to the interference pattern. Fig. 2.5 shows the result. The coherence length was found to be approximately $28 \mu\text{m}$ (FWHM). Thus, its bandpass is $\approx 60 \text{ nm}^1$, i.e. in between the narrow J-band and the full J-band filter, see Fig. 2.4 (right inset).

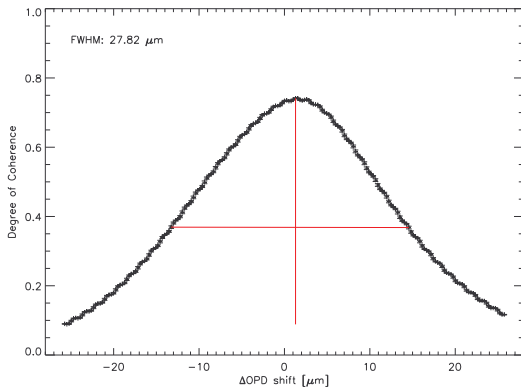


Figure 2.5: Measured fringe contrast versus OPD.

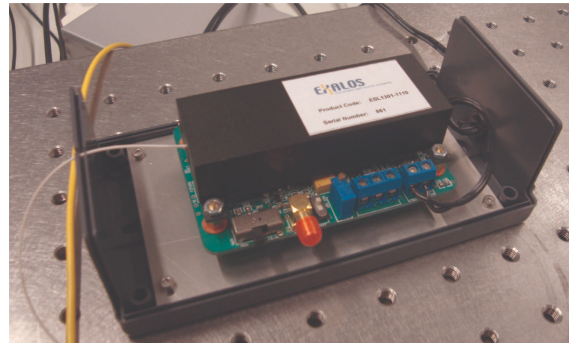


Figure 2.6: The semiconductor laser light source (cover removed).

¹ $\Delta\lambda = \frac{\lambda_{mean}^2}{FWHM}$, where $\lambda_{mean}^2 = 1.31 \mu\text{m}$ is the assumed central wavelength of the light source

The fibers

Two different types of fibers are used within the setup. In between the light source (A) and the polarization controllers (C), simple single mode fibers are used. They are reliable and easily available. Note that the use of multi mode fibers would not be beneficial in any way: The coupling efficiency between multi mode and single mode fibers is very low in general, while polarization maintaining fibers are only available as single mode fibers. Beyond the fiber polarization controllers (C), polarization maintaining (PM) fibers are used. All fibers are optimized for transmission of light with a wavelength of 1300 nm. The fibers are all equipped with FC/PC connectors (FC Physical Contact).

Y - coupler

Fig. 2.7 shows the non-polarization maintaining Y-coupler from Newport (F-CPL-F12135-FCUPC). Since the intensity of the beams can be adjusted independently (see below), the precise splitting ratio is unimportant, yet it was confirmed that the splitting ratio is close to 50% / 50%.



Figure 2.7: This Y-coupler splits the light injected at the fiber input on the left equally onto the two output ports on the right.

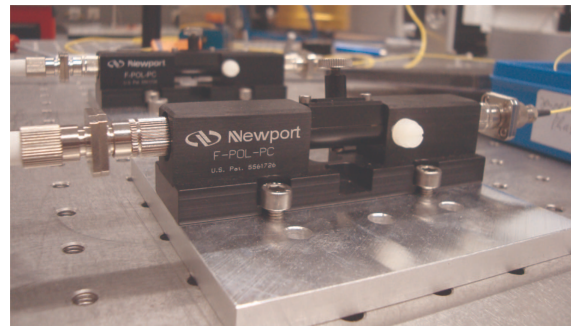


Figure 2.8: The polarization controller. A polarization maintaining fiber is fixed within the device. Using the screw on top of the central part, one can apply stress to the fiber. The central part can be rotated, which applies a torque on the fiber. By carefully adjusting the torque of the screw and the position angle of the central part, this device can control the output polarization state.

Polarization controller

The polarization controllers (C in Fig. 2.2) were purchased from Newport (F-POL-PC, see Fig. 2.8). These devices work by applying stress induced birefringence in a controlled way to a polarization maintaining internal fiber. In this way, one can in principle achieve any polarization state on the output. It is very important to have a defined polarization state on the input of the EO-PMs, since they act as linear polarization filters (see below). On the other hand, the combination of the polarization controller and the EO-PMs (acting as

a linear polarization filter) can be used to control the beam intensity at the fiber collimator outputs in each arm independently, since the EO-PMs will only transmit the part of the light with the correct polarization direction.

Electro-optical phase modulators

The electro-optical phase modulators (D in Fig. 2.2) are an integral part of the setup. They work by applying the inner electro-optic effect (also known as the Pockels effect). This effect describes the change of the index of refraction when an external electric field is applied. They are commonly constructed as integrated optics made from a specific material. Usually, lithium niobate (LiNbO_3) is used, since it exhibits a large electro-optic effect. This effect is anisotropic. Thus, these devices work most efficiently for a particular polarization state. On the other hand, integrated optics from LiNbO_3 are highly polarizing, i.e. they act as a linear polarizing filter. Since no mechanically moving parts are involved, these devices can be operated at very high frequencies (up to GHz bandwidth) without losing efficiency.

The electro-optical phase modulators used in the setup were purchased from Jenoptik. They are equipped with FC/PC-connector-terminated, polarization-maintaining fibers on the input and output. Jenoptik does not guarantee the specified performance for operations with input voltages higher than 100 V (private communication). Therefore, the input control signal is restricted to 80 V maximum when creating the control sequences in software.

The phase shift exhibited is linear to the applied voltage. Jenoptik gives the following formula in a technical note:

$$\Delta\Phi = -\frac{\pi L}{\lambda} n_3^3 r_{33} \frac{V}{g} \Gamma, \quad (2.1)$$

where L is the length over which the homogeneous electric field is applied, n_3 the respective part of the refractive index vector, r_{33} the respective component of the electro optic tensor, V the applied voltage, g the distance between the electrodes and Γ a measure of efficiency accounting for deviations from a homogeneous electric field.

For the operation of the atmospheric piston simulator, the optical path modulation is of primary interest. The OPD modulation can be simply estimated by: $\Delta OPD = \lambda \Delta\Phi$, where $\Delta\Phi$ is the phase modulation introduced in equation 2.1 and λ the wavelength of the transmitted light.

$$\Delta OPD = -\pi L n_3^3 r_{33} \frac{V}{g} \Gamma \quad (2.2)$$

where the quantities are the same as in equation 2.1. Equation 2.2 gives the OPD modulation by the EO-PMs as a function of the applied signal (V). Note that the OPD modulation is achromatic. This is true (within single atmospheric transmission windows) for the atmosphere too. That is, the temporal power spectrum of the OPD variation is not a function of wavelength.

The efficiency of EO-PMs is usually summarized and described by a half-wave voltage. It denotes the voltage which has to be applied to shift the phase by π for the specified central wavelength of the device. A half-wave voltage of $V_\pi=8$ V was specified by Jenoptik for the purchased devices for a central wavelength of 1300 nm (eff. bandwidth $\Delta\lambda=100$ nm). Thus, given the 80 V limit, these devices can provide a maximum phase shift of $\approx 10\pi$. Fig. 2.9 depicts the two EO-PMs used for the atmospheric piston simulator.

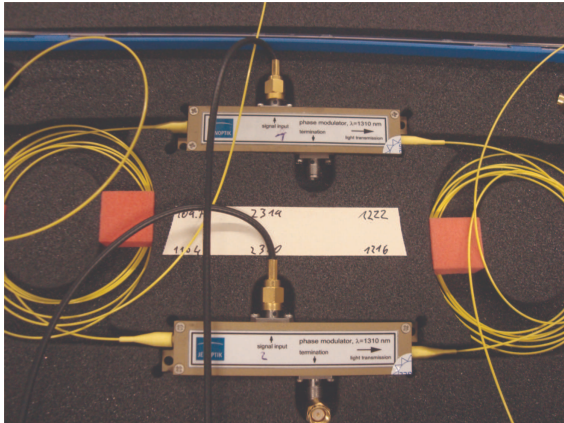


Figure 2.9: Picture of the EO-PMs.



Figure 2.10: The two fiber stretcher devices. The inputs and output can be seen on the bottom device, while the other device is rotated by 180° for easier fiber cabling.

Fiber stretchers

Since the atmospheric differential piston has a maximum amplitude of a few $10 \mu\text{m}$ at low frequencies, the EO-PMs cannot provide sufficient range in OPD to accurately simulate the atmosphere. Therefore, fiber stretchers are implemented as well (E in Fig. 2.2). Fiber stretchers consist of a piezo element, which literally stretches the fiber inside the device. They are commonly built as a spool setup, where several tens of meters of fiber are wrapped around a piezo core (see Fig. 2.10).

There are two main limitations commonly associated with fiber stretchers. First, by stretching the fiber in this way, anisotropic stress is applied to the fiber, which usually will, depending on the amount of stretching, not only vary the internal OPD, but also the polarization state at the output. Second, they usually exhibit all problems which piezo elements are known to possess, e.g. hysteresis effects, overshoot, temperature sensitivity etc.

The custom made devices were purchased from OptiPhase. They are both made from 41 m of Corning polarization maintaining fibers (optimized for transmission at $\lambda = 1300 \text{ nm}$). The distributor built them to be equal in length, with a tolerance of a few millimeters. After integration, the difference in optical path was found to be only $\approx 1 \text{ mm}$. The difference in length was determined by measuring the required additional OPD offset introduced by moving the linear stage.

Imaging optics

Here, the entire system of bulk optics is summarized. These will not be used for the verification of the fringe tracking system. For on-bench tests, the optics and detectors of LINC-NIRVANA will be used instead. The light is ejected from the fibers by means of a fiber collimator from Newport (F-H10-IR-FC, F in Fig. 2.2). These fiber collimators can be adjusted to the numerical aperture of the fibers and deliver a parallel beam approximately 7 mm in diameter, depending on the numerical aperture. One of these fiber collimators is mounted on a linear stage (driving range 15 cm, G in Fig. 2.2). The driving direction of

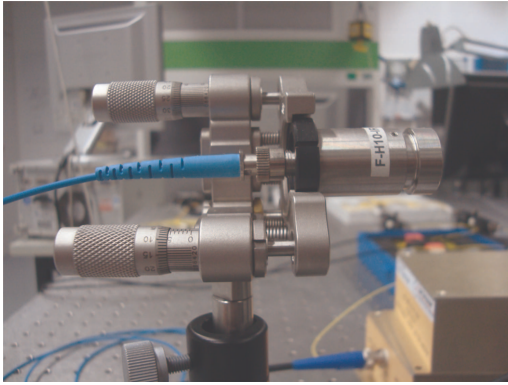


Figure 2.11: One of the fiber collimators. The beam can be tip/tilt corrected by the micrometer screws on the left. The collimator can be adjusted to the fiber numerical aperture by adjusting the position of the front part with respect to the fiber end.

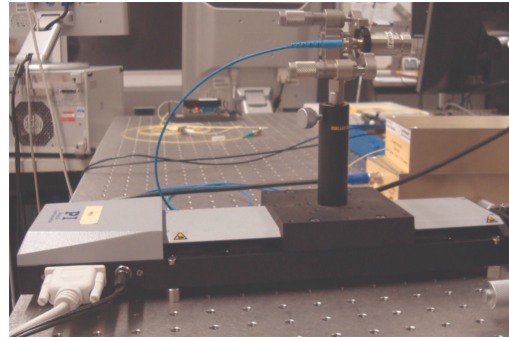


Figure 2.12: One of the fiber collimators is attached to a linear stage, which can be moved with sub μm precision parallel to the optical axis. This lets us adjust intrinsic static large OPDs.

the linear stage is parallel to the beam direction. The two arms of the interferometer do not precisely form the same optical path, and the coherence length of the light source is only a few tens of micrometers. Thus, an independent means of adjusting the OPD is necessary for operations in the lab. Since the linear stage will not be available for the fringe tracking verification, other means of controlling the static OPD have to be introduced at this stage (see section 3.1). One of the fiber collimators is presented in Fig. 2.11. The fiber collimator attached to the linear stage is shown in Fig. 2.12.

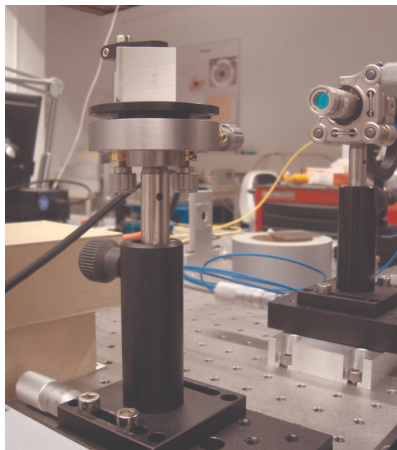


Figure 2.13: The 90° reflective prism. The positioning can be controlled by the micrometer screws. Note the fiber collimator to the right.

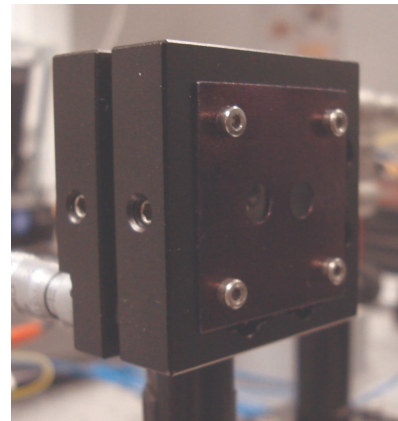


Figure 2.14: Customized aperture mask which defines the pupil of the optics. The single apertures have a diameter of $d \approx 4.9 \text{ mm}$ and a separation of $b \approx 8.8 \text{ mm}$ (center-to-center).

The beams are then reflected from a 90° prism (Fleige optic, H in Fig. 2.2) which was treated with a reflective coating (see Fig. 2.13). In this way, a fixed angle of 90° is achieved between the two reflective surfaces, while at the same time assuring a very good optical quality of the

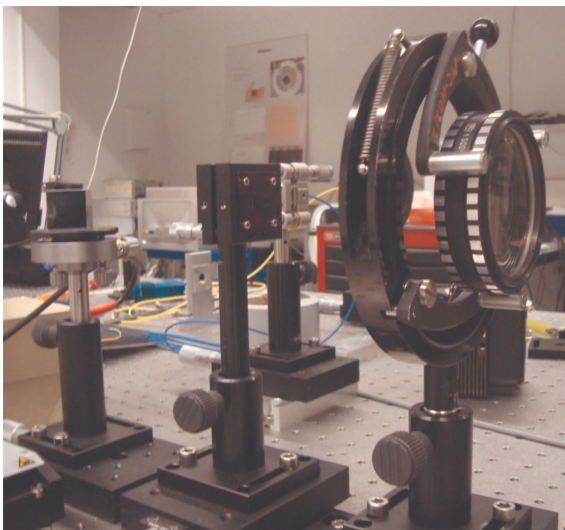


Figure 2.15: Reflective prism, aperture mask and first lens ($f=500$ mm) of the imaging optics.

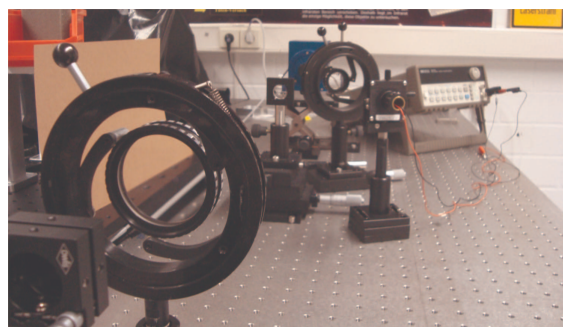


Figure 2.16: Overview of the imaging optics. The aperture mask and the first lens ($f=500$ mm) are in the front left section. In the rear right section, one can see the second lens ($f=-50$ mm) of the imaging optics, the diode and its single lens ($f=120$ mm) imaging optics, the signal generator and the detector.

surfaces. The prism is attached to a stage, which allows rotation in 3 axes and translation in 2 axes. After the reflective prism, there is a custom made (MPIA mechanical workshop) aperture mask (see Fig. 2.14, I in Fig. 2.2). This aperture resembles approximately the aperture geometry of the LBT, i.e. the ratio of single aperture diameter to aperture separation. This ratio defines the geometry of the PSF. Thus, the system can be calibrated under conditions similar to the optical imaging conditions in LINC - NIRVANA . The aperture mask is attached to opto-mechanics. It possesses a precision translational axis in the horizontal plane and can be tipped and tilted with respect to the plane perpendicular to the beam. The single apertures have a diameter of ≈ 4.9 mm and a separation of 8.8 mm (center-to-center). The imaging optics were designed by Peter Bizenberger (MPIA), using the ZEMAX optical design software. They comprise 2 lenses ($f_1=500$ mm, $f_2=-50$ mm, J, K in Fig. 2.2); compare Figs. 2.15 and 2.16. This leads to a focal ratio of $F/325$. The PSF has approximately a diameter of $r \approx 3$ mm (first Airy null) on the detector.

The blinking diode

The camera readout software does not provide the user with any temporal information (time stamp) and only little information whether the readout was successful and/or biased somehow. In the course of the lab experiment, the need for an independent means for assessing the temporal information became clear. This was solved by extending the lab setup (see Figs. 2.16 and 2.17). A single diode emitting at 1300 nm was aligned and imaged using a single lens onto the image plane, well separated from the image of the piston simulator (for an image of the focal plane see Fig. 2.19). The diode is driven by a frequency generator. The frequency generator delivers a triangle wave, the offset, amplitude and frequency can be set. The frequency is typically 10 Hz. The amplitude and offset are chosen such that both the minimum and maximum peaks are well within the dynamic range of the detector. In the data reduction process, a triangular wave is fitted to the mean intensity of the spot. This presents a very precise tool to assess the average time between two consecutive frames and a means to find intrinsic problems occurring in the readout.



Figure 2.17: Front of the “blinking diode”. The pupil can be positioned in xy .

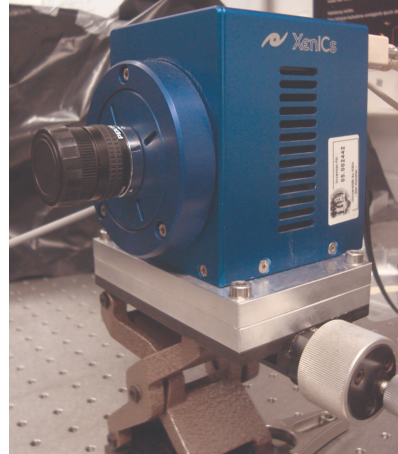


Figure 2.18: The infrared detector used for the atmospheric piston simulator lab setup. Note that the objective lens is removed during the measurements. The focal plane of the imaging system is defined by the detector chip.

Detector

For the data acquisition, a previously acquired infrared camera was used in the lab (Xeva-1.7-320 from Xenics, see Fig. 2.18, L in Fig. 2.2). The detector has a size of 320×256 pixels, each $30 \mu\text{m}$ square. It is sensitive from $0.9 \mu\text{m}$ to $1.7 \mu\text{m}$. There is a tool running under Windows to access the camera, yet it proved to be not efficient enough for the fast subframe readout. Thus, this tool is merely used to send commands to the camera, while a Camera Link system is used to do the actual readout. Fig. 2.19 depicts the full detector frame. Note the PSF of the atmospheric piston simulator in the right section of the frame; the fringes are clearly visible. In the left section, the irregular spot denotes the image of the blinking diode (see above, section 2.3.2).



Figure 2.19: Screen shot of the full detector area.

2.4 Control and readout of the atmospheric piston simulator

This section briefly describes the software to control the electro-optical phase modulators and fiber stretchers, which will introduce the piston sequences. The software to read out the camera and to convert the raw frames into useful observables is presented as well.

2.4.1 Software control of the EO-PMs and fiber stretchers

Both the EO-PMs and the fiber stretchers are controlled by using an analog/digital converter card (AD card, Meilhaus, ME-4670i PCI). This particular card has 4 independent 16 bit analog outputs. Each output is separately opto-isolated, and can be driven with a maximum sample rate of 500 kHz. In analog mode, the accessible voltage range is fixed to $[-10\text{ V}, 10\text{ V}]$. This results in a minimum voltage increment of $\approx 0.3\text{ mV}$.

The card is addressed by a small self-written C-program using the software development kit (SDK) of the Meilhaus card. The program initializes the AD card. Then it reads in external files which contain the piston sequences to be generated for each device. These sequences are saved in float arrays. The program is set up in this way to keep the processor load during the actual control sequence generation to a minimum. This reduces the temporal jitter. The pre-calculated sequences also contain the phase shift value, which is the center between maximum and minimum phase shift of the whole sequence. A signal with this particular central value is sent to the phase modulating devices and input by the user is expected prior to actually starting the control sequence. This was done to enable the user at this point to make sure that the system resides close to zero OPD (i.e. one can find fringes). After input by the user, a loop is started. The loop either stops after a defined time or upon user input. During each loop cycle, only the current phase sequence value is read from the array and sent to the AD card to generate the voltage signal. The loop is constructed such that a cycle time of 1 ms is achieved. Thus, the signal stream has a bandwidth of 1 kHz. Note, that the differential atmospheric piston varies at frequencies less than a few Hz. The oversampling will lead to a smoother signal shaping and will allow to simulate instrumental OPD variations, i.e. vibrations, with a few 10 Hz. Finally, the program de-initializes the AD card and closes all running processes.

2.4.2 Software to create the piston sequences

To allow easier modification and implementation, the sequence preparation code was separated from the main program. It is written in IDL. The user can either specify an analytic sequence (for example simple sinusoidal sequences for calibration purposes), generate control sequences from measured piston sequences or it can process arbitrary power spectra supplied by the user.

If a power spectrum is supplied as input by the user, the program first generates a piston sequence from the power spectrum. The power spectrum is read and transformed into an spectral amplitude spectrum. In order to generate a piston sequence by applying a complex Fourier transform, a spectral phase spectrum is required as well. The spectral phase spectrum is constructed by assigning random phase terms (uniform distribution, values range from 0 to 2π) to the frequency grid which is defined by the amplitude spectrum. This reduces the correlation of the components of the complex spectrum. The amplitude and phase spectrum are finally converted into the piston sequences by a complex Fourier transform.

Depending on user input, the piston sequence can be generate by using only one phase

modulating device or several synchronously. In the first case, the control sequence is generated by applying the gain of the respective phase modulating device. In the second case, the phase sequence to be generated is split among the specified phase modulating devices, taking into account their specific gains. If devices in both arms are required to be controlled, the control signal can either be applied in parallel or in antiparallel. Since a parallel variation of the optical path would not give rise to a differential phase variation, the control signal is generated in antiparallel as the default choice.

Finally, the generated control sequences minima and maxima are determined and compared to safety limits for each device. If the signal stays within the safety limits, the mean of each sequence is determined (see section 2.4.1). Both the control sequence and the mean of the sequence are then written to a file (a separate file for each device to be controlled).

2.4.3 Camera readout

As already explained above (see section 2.3.2), the camera is read out using a Camera Link system. The Camera Link PCI card in the readout computer is controlled and addressed by a self-written C-program. The C-program first initializes the Camera Link card and provides it with necessary information on the expected frames (frame dimensions, pixel depth). Then, it requests frames from the camera and saves them as raw binary files to disk. Processing the data during readout could lead to serious time lags between two consecutive readouts due to the elaborated data processing. The data needs to be written to disk in any case for analysis and comparison of the sequences. Thus, offline data processing is preferable for high speed readouts. After the number of frames specified by the user is read out, the program de-initializes the Camera Link card and closes all processes.

2.4.4 Post-processing the detector frames

The data processing software is written in IDL (Interactive Data Language, ITT VIS). On start up, it allows the user to specify necessary information on the frames to be processed (i.e. frame pixel width and height) and to set several flags which will influence the data processing process. The whole program is modular. After each module completes its task, the current data processing product is combined and saved to disk. For example, the one dimensional fringe patterns for each read out are collected and stored to a single file. These intermediate steps can be read in during later runs by setting the appropriate flags. Thus, the user can make slight modifications to parts of the program (for example changing plotting parameters) while the previous modules do not have to be run again.

The program first reads the data from a user specified data directory. Separate directories containing calibration data (to determine frame statistics and characteristics) or data with incoherent images (to determine fixed geometric parameters of the PSF) can be specified, as well. The program checks for binary files in the specified folders, and transforms them to ASCII tables for easier access. Then, each frame is read separately. Frame corrections (Bias, bad pixel map) are calculated and applied if the respective flags are set. The frame sections which contain the piston simulator PSF and the image of the blinking diode are separated by applying different regions of interest (ROI). The piston simulator PSF is averaged along the vertical direction and the average value over the diode ROI is calculated. Both pieces of information, the one dimensional piston simulator PSF profile and the mean diode intensity, are saved to separate files. Fig. 2.20 depicts the subframe as obtained by the Camera Link data acquisition. The red boxes indicate the ROIs. The mean diode intensity is determined

as the mean over the small box to the left, the fringe pattern is determined by averaging the box to the right in the vertical direction.



Figure 2.20: Subframe as obtained by the Camera Link data acquisition. The red boxes denote the applied regions of interest (ROI). The subframe has a total size of 224×8 . Compare with Fig. 2.19.

If specified by the user, the set of incoherent frames is analyzed next. The following equation is fit to each frame, and the most probable parameters are averaged afterward over the set of calibration frames.

$$I(\theta) = 2I_0 \left(\frac{2J_1(\theta)}{\theta} \right)^2, \quad (2.3)$$

$$\theta = 1.22\pi \frac{x - x_0}{r_a},$$

where J_1 is the Bessel function of first kind and order, x_0 denotes the peak position of the PSF within the ROI coordinate system, r_a is the radius of the first null of the Bessel function and I_0 the peak intensity of a single aperture PSF. The factor 2 accounts for the two single aperture PSFs overlapping incoherently. By determining these parameters and fixing them for the subsequent fitting of the interferometric fringes, the determination of the fringe phase becomes much more robust and reliable. Fig. 2.21 shows a fit of a single frame. Black crosses depict the mean intensity of a single pixel column in the ROI (i.e. collapsed in y direction), the error bars denote the respective standard deviation. The red line gives the fit according to equation 2.3.

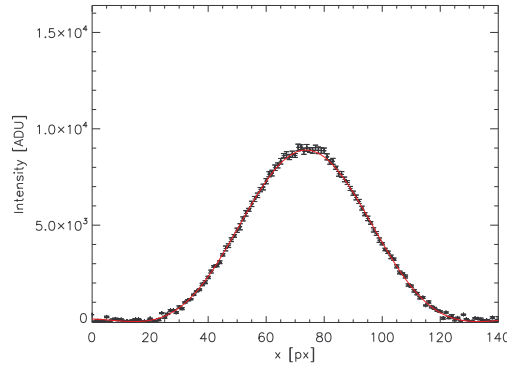


Figure 2.21: Fit of the PSF produced by incoherent superposition of the PSF of the two single sub-apertures (see equation 2.3). Black crosses denote data, the red line depicts the fit.

Next, the mean intensities of the blinking diode images are analyzed. Here, a simple triangle wave is fitted to the sequence of mean intensities as a whole. One can determine in this way any temporal jitter from deviations to the theoretic profile. It was found though that the camera runs very stably and reliably in continuous mode. In this way, a precise time stamp can be determined for each frame. This is done by comparing the fitted triangle wave period (in number of frames) to the applied signal period (in ms). Fig. 2.22 depicts a cut from a

diode sequence. The data is depicted with black crosses and the fit with the green dashed line. The red crosses in the upper part indicate the time elapsed during the respective frame acquisition cycle Δt which is measured by the camera readout program. Note that the jitter of Δt is negligible.

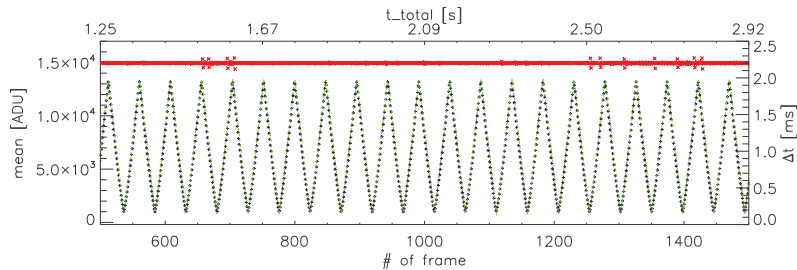


Figure 2.22: Sequence of the mean intensity of the blinking diode (black crosses), fit with a triangular wave (dashed green line) and timing between consecutive frames (Δt , red crosses).

In the next software module, the fringe phase information is finally determined by fitting the following function:

$$I(\theta) = 2I_0 \left(\frac{2J_1(\theta)}{\theta} \right)^2 \left(1 + V \cos \left(2\frac{b}{d}\theta + 2\pi\Phi \right) \right), \quad (2.4)$$

$$\theta = 1.22\pi \frac{x - x_0}{r_a},$$

$$\frac{b}{d} = \frac{\text{diameter of single aperture}}{\text{aperture separation (center to center)}},$$

where I_0 , J_1 , x_0 and r_a have the same meanings as above. $\frac{b}{d}$ determines the fringe frequency and Φ is the required phase information. The amplitude factor V takes account of possible fringe contrast degradation. For a perfectly coherent source, $V=1$ for any phase shift Φ . Since the light source has a limited coherence length, $V \approx 1$ for zero OPD and then decreases to 0 outside the coherence length of the light source (see Fig 2.6). Fig. 2.23 depicts an example of a fit of equation 2.4 to a measured fringe pattern.

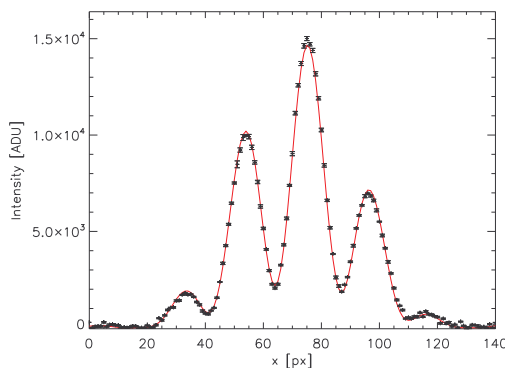


Figure 2.23: Example of fringe fitting. Black crosses indicate the data and the red line indicates the fit.

In the current version of the data reduction software, I_0 , x_0 and r_a are fixed by analyzing the

incoherent images. The fringe frequency $\frac{b}{d}$ is defined by the geometry of the aperture mask. Thus, it is fixed as well to a nominal value of 1.8. There is a software option to visualize the fit to each frame. In this way, the user can make slight adjustments to the fixed parameters in order to improve the fit on a global basis. Note that this option should be switched off when fitting the entire set of frames to increase the speed.

After the phase sequence is retrieved from the data, the software produces some plots to visualize the data. Fig. 2.24 depicts one of the phase sequences obtained in this way. A sine modulation of 1 Hz was applied using one EO-PM (peak amplitude=10.13 V). One can nicely see a low frequency modulation of the mean of the sine function. This modulation can partially be explained by a temperature variations (see section 2.5.3 below).

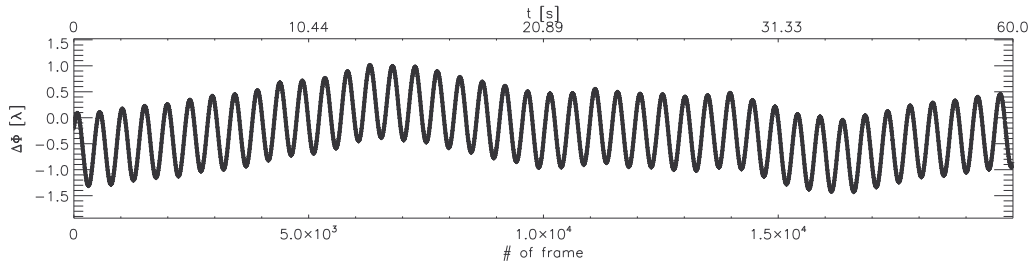


Figure 2.24: Fitted phase sequence. Note the low frequency modulation of the sinusoidal wave caused by the low frequency noise floor.

In addition, the phase sequence is Fourier transformed (using the IDL FFT routine). A fast Fourier transform (FFT) does only rely on the assumption, that the data points are equidistantly sampled on their domain. Thus, to generate the respective frequency grid associated with the Fourier transform one needs to assess the average time difference of two consecutive frame acquisitions. This is done by making use of the precise time stamp generated by the blinking diode. In general, one could use the time stamps in conjunction with more sophisticated Fourier transform routines. But since the temporal jitter of the frame acquisition is negligible, this is unnecessary

The complex Fourier transform is then transformed into an amplitude spectrum, which is a powerful tool for calibrating the system. Fig. 2.25 depicts such a Fourier amplitude spectrum. Note the peak at 1 Hz and the contribution of the noise floor at low frequencies.

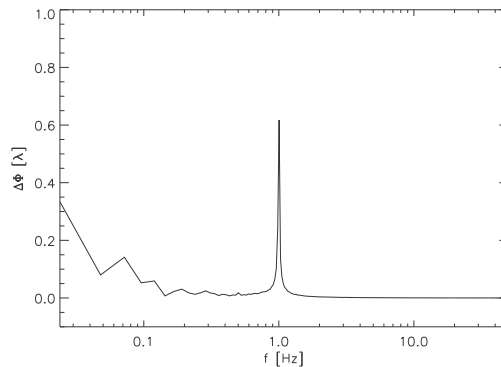


Figure 2.25: Fourier amplitude spectrum, as obtained from the 1 Hz sinusoidal phase sequence (Fig. 2.24).

2.5 Calibration and verification of the lab experiment

Since the atmospheric piston simulator shall serve as a tool to calibrate and verify the fringe tracking system of LINC-NIRVANA, its operation also needs to be carefully calibrated and verified beforehand. This involves careful calibration of each of the phase modulating devices on its own, calibration and verification of synchronous control of the various devices, and identification of intrinsic errors and limitations. In this section, the results of this process are presented and discussed.

2.5.1 Description of the calibration / verification experiments

Optical fibers are very sensitive to temperature variations and mechanical stress. If the temperature varies between the two fibers, this will lead to a slightly different thermal expansion of the two interferometric arms, which leads to an additional differential phase component. This component varies on timescales of a few tens of seconds to minutes if the environmental temperature is stable on average. Mechanical vibrations in the system, either affecting the optical fibers or the optics, will introduce an additional noise floor. Therefore, a calibration procedure is needed which allows an easy and reliable separation of the intentionally introduced differential phase sequences and the noise floor. The noise floor will be quantified in section 2.5.3 below.

To achieve the necessary separation of different effects, the calibration was done using sinusoidal signals with a defined amplitude and frequency. This allows for an easy identification of the control signal in a Fourier amplitude spectrum. The signal will appear as a single peak, in contrast to the low frequency noise floor. At the same time, this approach allows a quantification of the average power spectrum of the noise floor. Finally, the analysis of the Fourier spectrum will reveal immediately inconsistencies in the timing of the control signal (e.g. if there is an intrinsic problem with the signal clock frequency, this will introduce a frequency shift), while any temporally stable errors will be filtered.

Optical fibers are very sensitive to mechanically introduced stress or vibrations. In general, this effect will only marginally affect operations, since the whole setup is built on top a properly suspended optical bench. Nevertheless, the fiber stretchers will apply considerable stress on their spooled fibers. Therefore, one has to verify whether the operations of the fiber stretchers exerts any influence on the transmitted light, i.e. they might change the polarization vector of the light by stress-induced birefringence.

An actual calibration sequence thus comprises a set of sinusoidal signals of different voltage amplitudes. Since it is not clear from the beginning whether the gain of the phase modulating devices is a function of applied signal frequency, the calibration needs to be done at several frequencies. To ease and speed up the calibration process, more complex differential phase sequences were used. These sequences consist of several single sequences, each having a length of 60 s. The sinusoidal signals of the single sequences share the same amplitude, yet have a different frequency. The differing frequency components can again be nicely separated in the complex Fourier transform. The set of frequencies was chosen to span the range from very low frequencies up to the desired maximum rate of the fringe tracking system in LINC-NIRVANA. The frequencies analyzed were: 0.1 Hz, 0.5 Hz, 1.0 Hz, 5.0 Hz, 10. Hz and 20 Hz.

Thus, the goals of the calibration and verification are:

- Quantification of the noise floor

- Stability of polarization state of the output light
- Gain calibration of all devices
- Gain dependence on signal frequency
- Verification of operation of the devices in parallel / antiparallel
- Overall verification of the atmospheric piston simulator

2.5.2 A word on the achievable precision

The precision to which OPD variations can be measured with the lab setup mainly on two intrinsic effects. This precision affects the calibration and verification as well. First, the length of the applied sequences needs to be long enough to allow verification of the fringe tracking system under realistic conditions. The fringe tracking system has to be able to stabilize the fringes for several minutes. Note that the analysis of longer sequences increases the spectral resolution in Fourier space as well. The applied sequence length of 60s corresponds to a frequency resolution of ≈ 0.02 Hz. The main problem arising from the frequency resolution is the spectral leaking associated with discrete Fourier transforms. Spectral leaking occurs if the frequency of a signal is not precisely represented in the set of frequency bins. The power attributed to the signal is then distributed to the neighboring frequency bins, which makes the precise determination of the signal amplitude and its error difficult.

The second effect is intrinsic to the measurement and data reduction procedure. The applied fitting routine has only very limited *a priori* knowledge of the total phase shift applied. Thus, to determine the total phase shift at a certain point in the sequence, all frame - to - frame phase shifts are added up. The result will be correct as long as there are no phase jumps larger than $\pm\pi$ between consecutive images. If there are phase jumps with an amplitude larger than π , the fitting algorithm will be confused by the periodicity of the cosine part, since the cosine function is only bijective on the set $[-\pi, \pi]$, i.e. the cosine function can only be inverted on this set. Thus, the fitting algorithm and, therefore, the determination of the signal response will be correct if and only if the phase shift between two consecutive images is less than $\pm\pi$.

When a sinusoid is applied as the control signal, the signal rises from 0 to maximum amplitude within a quarter of the sinusoid's period. This gives rise to the following approximate phase shift between two consecutive images for a sinusoid control signal of given amplitude A , a frequency $f = T_{period}^{-1}$ and a readout time of $t_{readout}$:

$$\begin{aligned} \Delta\Phi &= \frac{A}{\frac{T_{period}/4}{t_{readout}}} \\ &= 4 \times A \times f \times t_{readout} \leq \pi \\ \Leftrightarrow A &\leq \frac{\pi}{4 \times f \times t_{readout}} \end{aligned} \quad (2.5)$$

Thus, a signal of given frequency should not exceed a maximum amplitude “slew” rate given by the above formula. For example, the amplitude of a 10 Hz sinusoid should not exceed ≈ 39 rad or $\approx 6.5 \lambda$ if the data is acquired with $t_{readout}=2$ ms. The dimension of A can be easily converted knowing the gain of the phase modulating device used. In practice, the maximum amplitude which can be unambiguously recovered will be lower. This is due to the fact that 1) the above derivation assumes a constant temporal gradient of the phase shift and 2) the actual requirements of the fitting routine are slightly more stringent than $\pm\pi$.

2.5.3 Power spectra of noise floor

The phase of light transmitted by a fiber is very sensitive to the ambient temperature and mechanical stress caused by vibrations. In the reconstructed phase sequences this can be observed as an additional spectral component at low ($\lesssim 0.5$ Hz) frequencies (see Fig. 2.24). These effects are in general not correlated with the piston sequences which are introduced by the phase modulating devices. Thus, the noise floor implies a lower limit on the achievable precision at a given frequency. In order to quantify these effects, the fringe movement was monitored for a few minutes without applying a signal to the phase modulating devices. The amplitude spectra of the measured piston sequences are depicted in Fig. 2.26.

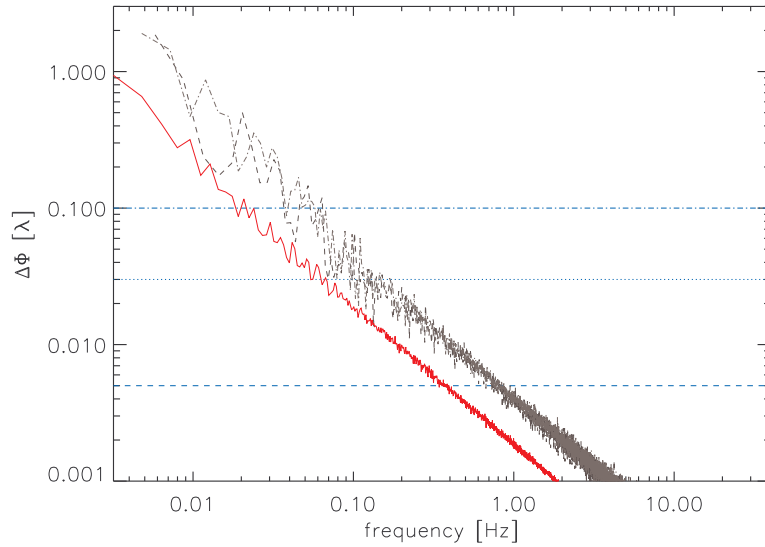


Figure 2.26: Amplitude spectra of the noise floor. Grey dashed and light grey dashed dotted lines represent measurements with the “regular” setup. The red line represents data including increased thermal insulation. The blue dashed line depicts the highest theoretically obtainable precision in phase modulation when using both fiber stretchers in parallel (defined by the voltage increment of the AD card and the gains of the fiber stretchers). The blue dotted line is the required precision of the phase modulation for the LINC-NIRVANA fringe tracking system verification, the blue dashed dotted line is the requirement for the residual differential phase during fringe tracking operations.

Note that the power spectra obtained with the “regular” setup (as described above, see section 2.3) are very similar. The amplitudes of the noise floor start to be higher than the maximum theoretically achievable precision of the atmospheric phase modulator at ≈ 0.8 Hz, and the required precision for the verification of LINC-NIRVANA is reached at ≈ 0.1 Hz. Thus, the required absolute precision could not be guaranteed already after 10 seconds of operation.

A major component of the noise floor is caused by a differential temperature variation between the two fiber arms. In order to assess the influence of this effect, the thermal insulation of the whole atmospheric piston simulator was increased in a simple test by padding the fiber setup. The procedure was repeated, and the result is depicted in Fig. 2.26 by the red curve. This simple increase of insulation resulted in a significant decrease of the amplitudes at all

frequencies in the frequency spectrum. The required absolute precision was reached at only ≈ 0.05 Hz, a factor of 2 better than in the uninsulated case. This enhancement can probably be increased with a better designed insulation of all fibers. Note though, that the noise floor and the temperature effect on phase drifts needs to be quantified in any case again with the final setup on the bench, since the average ambient temperature and its stability can differ significantly in the LINC-NIRVANA AIV laboratory.

2.5.4 Stress induced birefringence by the fiber stretcher

Stress induced birefringence is a well known problem with optical fibers. In the case of the atmospheric piston simulator, this problem is alleviated somewhat by the fact that during a measurement, the gravity vector is not going to change. Thus, the position and bending of the fibers will be well-defined and stable, and any residual static effects can be calibrated. The only exception is the fiber stretchers. These devices are even more problematic, since they are supposed to work in conjunction with the EO-PMs. Since the fiber stretchers act as very efficient linear polarization filters, any change of the polarization state of the light caused by the fiber stretchers will have significant implications. If the fiber stretchers are placed before the EO-PMs in the optical setup, than a temporally varying modulation of the polarization state will change the output intensity. If the fiber stretchers are placed behind the EO-PMs, then the polarization state of the output light can significantly change. In addition, it is expected that these effects would be different in magnitude in both arms. Thus, either the intensity ratio or the relative polarization state would vary with time, making a conclusive measurement impossible or nullifying the utility of the piston simulator.

In order to check for this effect and to find possible limits on the applicable control signal of the fiber stretchers, an experiment to determine the influence of the fiber stretchers on the polarization state was performed. A linearly-polarizing filter was placed in front of the detector and either one or the other fiber collimator output of the interferometer arms was blocked. This was done to disentangle interference effects from polarization effects. The linear filter was then oriented perpendicular to the polarization direction of the incident light, thus blocking most of it. The blocking due to the linear filter is not perfect (see Fig. 2.27). One reason could be an imperfect linear filtering by the EO-PMs. Another reason might be a degradation of the polarization state, which is defined by the outputs of the fibers, by the reflections and refractions in the bulk optics. Fig. 2.27 illustrates the two cases (crossed and uncrossed linear polarization filter). The extinction is $\approx 95\%$ on average for both interferometer arms.

Next, to test whether the fiber stretchers affect the polarization vector of the transmitted light, a sinusoidal signal was applied with a frequency of 10 Hz and an amplitude of 50 V, offset by 50 V. This exceeds any signal which will ever be applied when controlling the atmospheric piston simulator and corresponds to an OPD modulation of $\pm 240 \mu\text{m}$, far larger than any anticipated atmospheric or instrumental effect. If the fiber stretchers do change the polarization vector of the transmitted light, then the polarization vector of the output beam will no longer be perpendicular to the linear filter. This would result in an increase in observed intensity for the crossed polarizer arrangement.

In order to illustrate this, a sinusoidal sequence as described above was applied and monitored with an effective frame rate of ≈ 480 Hz. Since almost no change in the measured intensity was noticeable, the standard deviation for each pixel in the vertically averaged ROI was plotted against the pixel number for the case when no modulation was applied and when applying the modulation sequence to the fiber stretcher (Fig. 2.28). Note that the standard

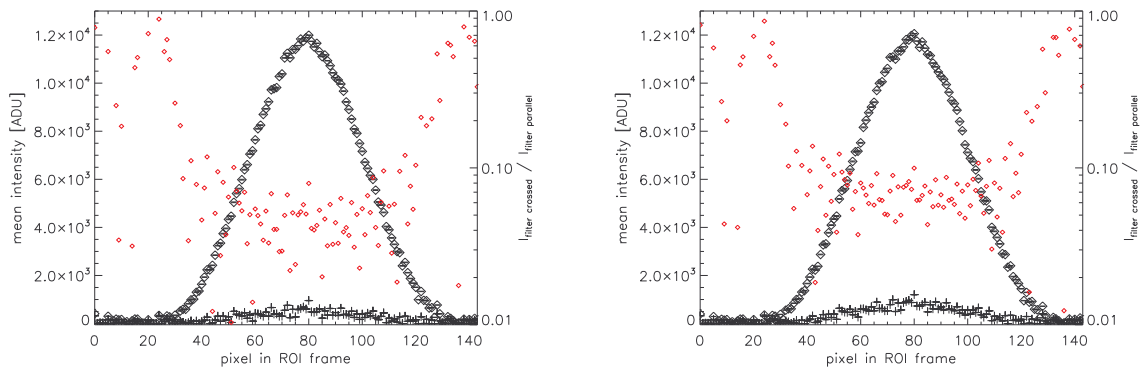


Figure 2.27: Comparison between parallel (black diamonds) and crossed (black crosses) linear polarization filter. Depicted are the mean intensities for each pixel across the ROI. The red diamonds depict the ratio crossed / uncrossed filter mean intensity for better illustration.

deviations are small in general (compared to the mean flux, compare Fig. 2.27). In addition, there is no significant difference, either on a scale comparable to the variation for each pixel for the time of the sequence or on the pixel-to-pixel variation scale.

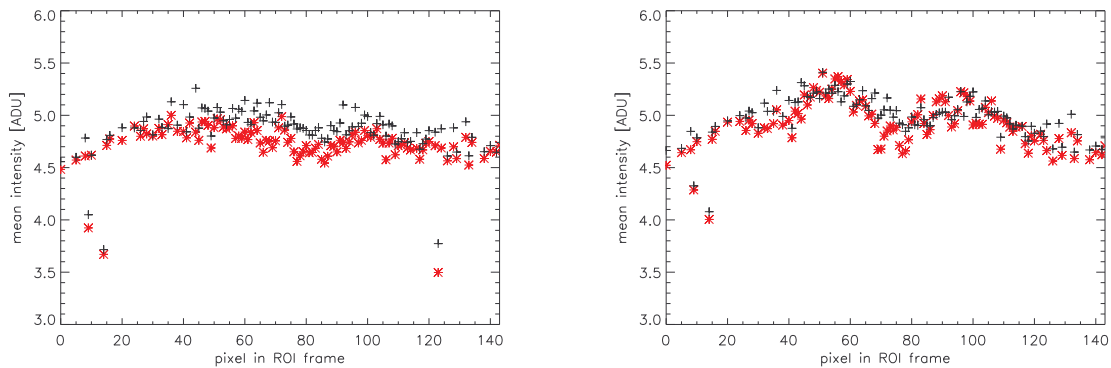


Figure 2.28: Pixel variation for the polarizing experiment. See text. The black crosses depict the standard deviations for each pixel when no fiber stretching was applied, the red asterisks depict the standard variation during the fiber stretching sequence.

2.5.5 Results

Calibration of the amplifier

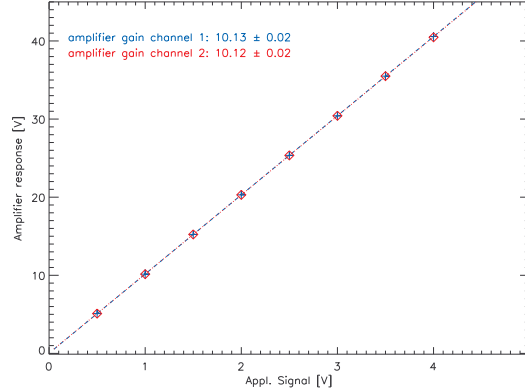


Figure 2.29: Calibration of the amplifier gain. The figure shows the output of the amplifier as a function of the input voltage. Blue crosses (data) and the blue dashed line (fit) depict the results for channel 1, and red diamonds (data) and the red dashed line (fit) depict the results for channel 2.

In order to determine the response of the amplifier which was mainly used in conjunction with the EO-PMs, the output voltages for given input voltages were measured with an oscilloscope. Fig. 2.29 shows the amplitude response of the amplifier. The gain is very linear and equal for both amplifier channels to within the standard variation as determined by the applied linear fit. It amounts to $10.13 \pm 0.02 \text{ Volt}_{\text{output}}/\text{Volt}_{\text{input}}$. The amplifier was as well checked for its frequency response. No peculiarities were found: the gain was stable over the whole input range of 0 V to 10 V and input signal frequencies up to 200 Hz. This was expected, since the primary use of the amplifier before its integration in the atmospheric piston simulator was to drive piezo stages at even higher signal voltages and bandwidths.

Calibration of the individual devices

Table 2.1: Gains determined for single device operations, EO-PMs and fiber stretcher. No gains were determined for the fiber stretcher for the 20 Hz control signal due to overly large fitting errors.

f [Hz]	EO-PM 1		EO-PM 2		stretcher 1		stretcher 2	
	gain [waves/V]	σ	gain [waves/V]	σ	gain [waves/V]	σ	gain [waves/V]	σ
0.1	0.078	0.006	0.066	0.006	4.85	0.35	4.81	0.31
0.5	0.078	0.006	0.068	0.005	4.88	0.37	4.69	0.34
1.0	0.072	0.006	0.061	0.005	4.78	0.36	4.61	0.34
5.0	0.067	0.006	0.059	0.005	3.62	0.40	2.77	0.31
10	0.060	0.005	0.057	0.005	4.08	0.61	4.07	0.50
20	0.067	0.006	0.053	0.005				

The gains of the individual devices were determined by applying control sequences as described in section 2.5.1. Then, the determined phase modulation was plotted as a function of the applied signal. Fig. 2.30 shows the calibration of the two EO-PMs, and their respective gains (in waves/Volt) are summarized in table 2.1. Each data point in Fig. 2.30 is determined by scanning the Fourier transform of the measured phase sequence for a peak. The position and the amplitude of the peak is determined. The applied voltage as depicted on the abscissa of Fig. 2.30 represents the peak amplitude of the applied signal. Fig. 2.31 depicts the calibration of the two fiber stretcher units, and the respective gains (in Phase shift/Volt) are summarized in table 2.1 as well.

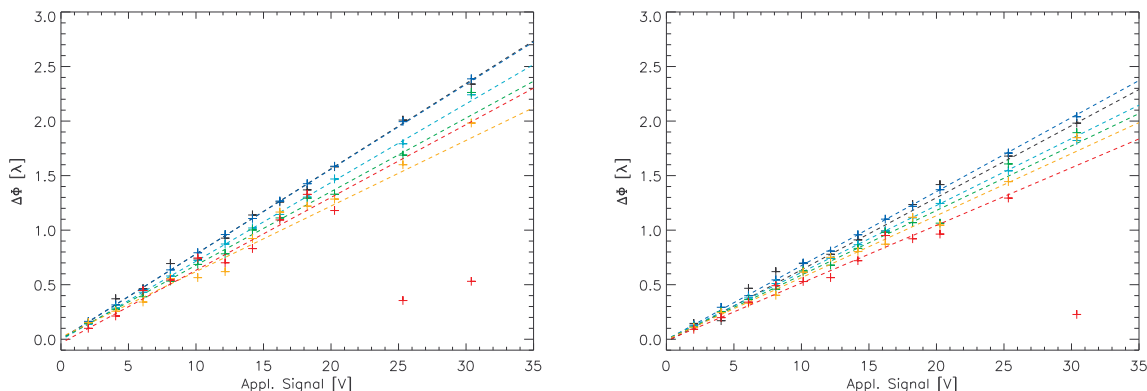


Figure 2.30: The calibration curves for the two EO-PMs. Crosses depict data points, dashed lines in the same color depict a linear fit. The colors indicate differing signal frequencies: black=0.1 Hz, blue=0.5 Hz, cyan=1 Hz, green=5 Hz, orange=10 Hz, red=20 Hz

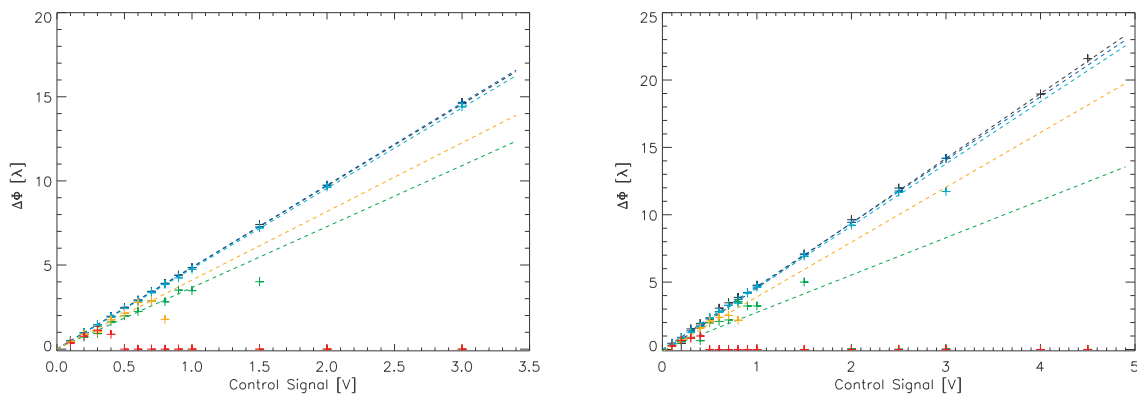


Figure 2.31: The calibration curves for the two fiber stretcher. Crosses depict data points, dashed lines in the same color depict a linear fit. The colors indicate differing signal frequencies: black=0.1 Hz, blue=0.5 Hz, cyan=1 Hz, green=5 Hz, orange=10 Hz, red=20 Hz

Note the variation in the gains obtained for different control sequence frequencies. For the three lowest control sequence frequencies (0.1 Hz, 0.5 Hz, 1 Hz), the variance of the gain for different frequencies is small in comparison to the uncertainty derived by the fit of the gain for a individual frequency. For higher control signal frequencies, the gain differs in comparison to the values obtained for lower frequencies. For control signal amplitudes higher than a

certain value (depending on the frequency), the apparent gain drops significantly. This can be explained by the slew rate effect described in section 2.5.2. From the presented calibration curves, a maximum “slew” rate, which is still determinable by the fitting algorithm, can be determined. It amounts to $\approx 0.21 \lambda$. This is only half of the approximated 0.5λ from section 2.5.2. This is expected, since equation 2.5 does not take into account the varying slope of a sine function, for example.

Calibration of the devices in parallel

Table 2.2: Gains determined for the OPD modulating devices operating either in parallel (EO-PMs) or antiparallel (fiber stretcher). No gains were determined for the fiber stretcher for the 10 Hz and 20 Hz control signal due to too - large fitting errors. The errors are increased due to the slew rate effect.

f [Hz]	EO-PM		fiber stretcher	
	gain $\left[\frac{\Delta\Phi[\lambda]}{V}\right]$	σ	gain $\left[\frac{\Delta\Phi[\lambda]}{V}\right]$	σ
0.1	0.16	0.01	9.64	0.69
0.5	0.15	0.01	9.58	0.69
1.0	0.15	0.01	9.45	0.68
5.0	0.11	0.01	6.84	0.90
10	0.13	0.01		
20	0.14	0.03		

Table 2.2 summarizes the results for the gain calibration for each of the two devices operating in parallel, and the respective graphs appear in Fig. 2.32. Here, a signal of equal amplitude was applied to each device in the symmetric setup, either the two fiber stretcher or the two EO-PMs. The two signals applied to each arm need to be phase-shifted by π with respect to each other (antiparallel operation). Applying an equal amount of phase modulation in each arm (parallel operation) will not result in a modulation of the differential phase, which is the observable (assuming equal gain for both devices). Interestingly, it was found that the EO-PMs have to be operated in parallel rather than antiparallel. Where the additional phase shift comes from is unclear in principle. Yet, when controlling them in antiparallel, the differential phase stayed constant (modulo the variations on the level of the noise floor described in section 2.5.3). Thus, this additional effect seems to be very confined and will not interfere with the operations in general.

2.5.6 Verification of overall operations

In order to verify the overall operation of the atmospheric piston simulator, several tests were performed. Note, that for all tests presented in this section the mean gain for each phase modulating device as defined in the conclusions (see section 2.6) was used.

First, a sinusoidal wave with an amplitude of 5λ was specified. The corresponding control signal was calculated by the control signal software (“antiparallel signal”) and used as input for the actual control software. The system response, i.e. the differential phase modulation as indicated by the moving fringes, was determined and compared to the anticipated sine curve. The same signal was applied again, this time including an additional phase shift of π

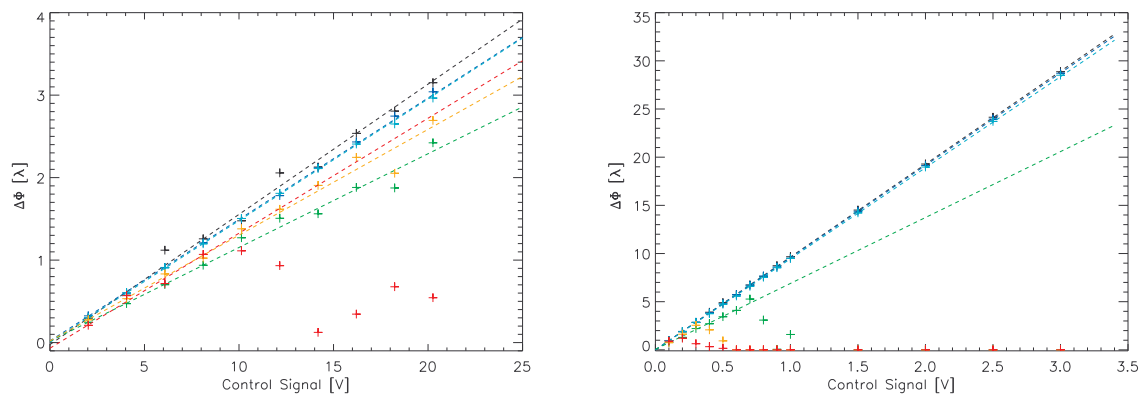


Figure 2.32: The calibration curves for the two EO-PMs operating in parallel (left figure) and the fiber stretchers in antiparallel (right figure). Crosses depict data points, dashed lines in the same color depict a linear fit. The colors indicate differing signal frequencies: black=0.1 Hz, blue=0.5 Hz, cyan=1 Hz, green=5 Hz, orange=10 Hz, red=20 Hz

(“parallel signal”). As expected, almost no modulation is seen. Fig. 2.33 compares sections of the two phase sequences as obtained by the data analysis software.

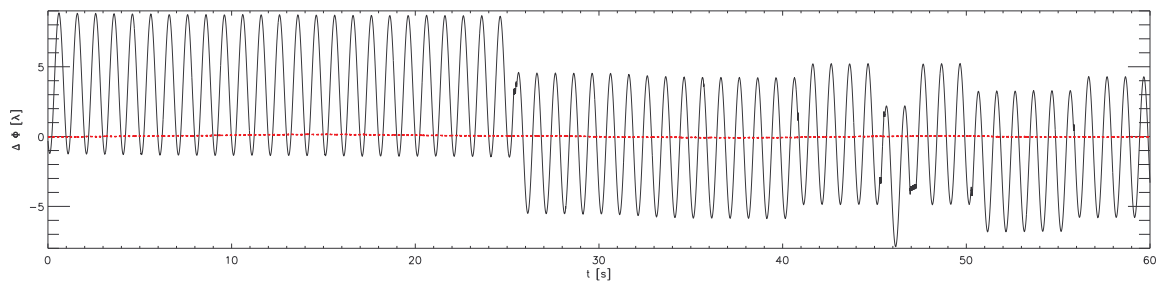


Figure 2.33: Comparison of two piston sequences. In both cases, a sinusoidal signal with an amplitude of 5λ was applied. The respective control signal was applied in antiparallel on the two fiber stretchers (black curve) or in parallel (red curve). The “jumps” at 25 s and 45 s are due to an imperfect fringe fitting by the data reduction software.

For a more quantitative comparison, the two phase sequences were Fourier transformed (see Fig. 2.34). There is still a peak at 1 Hz for the parallel modulation, yet the amplitude is less than 0.005λ , which is less than the achievable control precision. The ratio of the peak amplitudes for the antiparallel and parallel modulation amounts to 10^{-3} .

Next, a theoretical atmospheric differential power spectrum was used as input for the atmospheric piston simulator. To generate the theoretical spectrum, the LBT aperture geometry (aperture diameter $d=8.4$ m, aperture separation $B=14.4$ m), a wind speed of $v=10 \frac{m}{s}$ and a (somewhat arbitrary) power at ν_1 of 0.5 were assumed (see equations 1.6). Fig 2.35 compares the anticipated phase sequence (red curve) and the measured phase sequence. Note that the red dashed line was slightly shifted horizontally and vertically for an easier comparison. The offset in the time axis can be explained by the fact that there is no physical synchronization between the application of the control signal and the data acquisition. The offset in absolute phase is arbitrary, since the lab experiment data reduction software cannot determine the offset from zero OPD at the beginning of the measurement. The two curves perfectly match

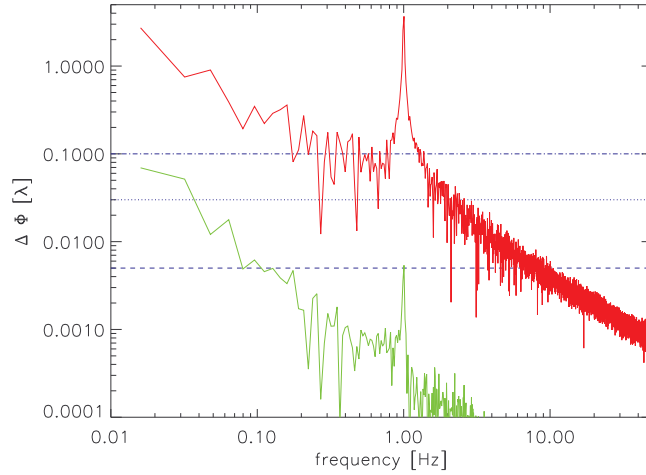


Figure 2.34: Comparison of the two Fourier amplitude spectra of the sequences presented in Fig. 2.33.

at the beginning. As time goes on, the measured phase sequence starts to deviate from the anticipated sequence. This is due to the additional phase drift introduced by the effects causing the noise floor. Still, the short time scale dynamics of the two sequences agree very well. For a more quantitative comparison of the dynamical behavior, both sequences were Fourier transformed. Note that the anticipated phase sequence was resampled to match the temporal resolution of the measurement (1 ms resolution of the control signal vs. 2.1 ms resolution of the measured sequence).

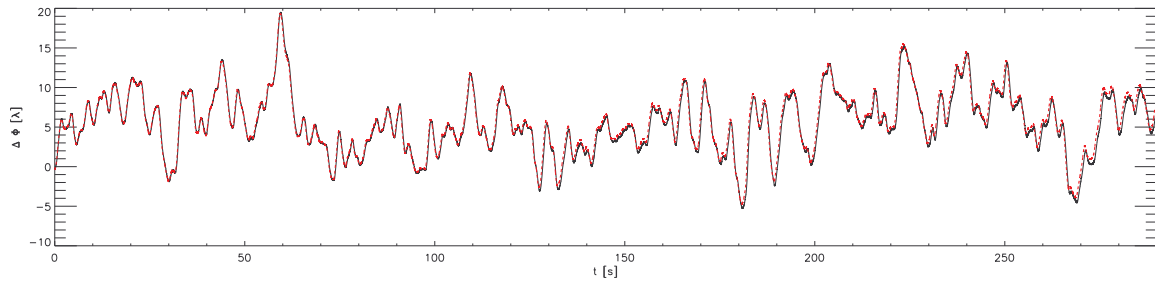


Figure 2.35: Comparison of the anticipated piston sequence (red dashed line) and the measured phase sequence (black line). Note that the red dashed line was shifted horizontally and vertically slightly for greater visibility. The two curves overlap very well.

The two power spectra presented in Fig. 2.36 agree very well. Note the “noisy” appearance of the power spectrum of the anticipated phase sequence. This can be explained as follows: In order to generate a piston sequence, an amplitude and a phase spectrum are required for the complex Fourier transform. Theory (see section 1.2) only makes predictions on the power spectrum of the differential atmospheric piston, which can be transformed in the amplitude spectrum. Thus, an assumption on the phase spectrum needs to be done in order to construct a true piston phase. It was assumed that the phase in each frequency bin is entirely uncorrelated. Thus, a random phase (uniform distribution) between 0 and 2π was associated with each frequency bin. If the phases of two consecutive frequency bins now differ by π ,

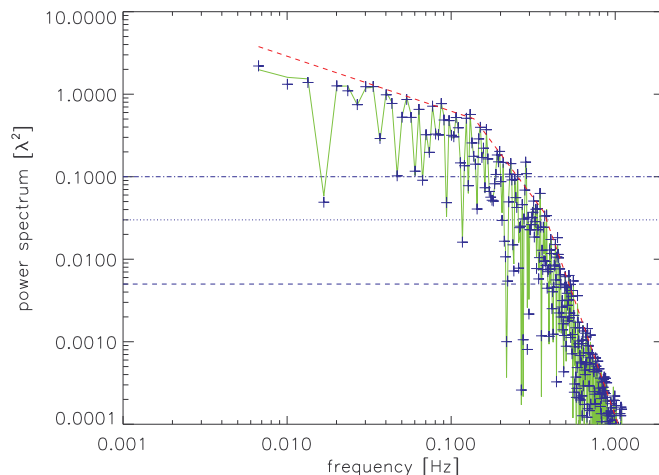


Figure 2.36: Comparison of the Fourier power spectra of the anticipated (blue crosses) and measured (green line) sequence (see Fig. 2.35). The dashed red curve shows the theoretical power spectrum used to generate the piston sequence.

the resulting sinusoids will cancel each other almost perfectly, giving rise to a “noisy” power spectrum.

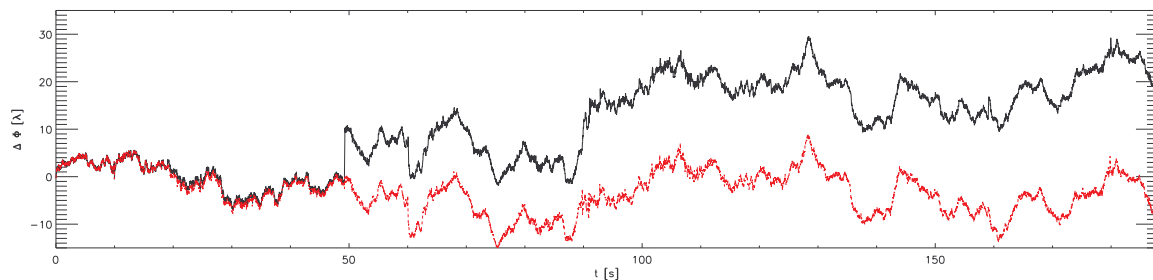


Figure 2.37: Comparison of the anticipated piston sequence (red dashed line) and the measured piston sequence (black line, MIDI data by W. Jaffe, private communication). Note that the red dashed line was slightly shifted horizontally and vertically for an easier comparison.

Finally, an OPD sequence obtained with MIDI (W. Jaffe, private communication, see section 1.2) was used as input for the atmospheric piston simulator. The piston sequence was scaled by $\frac{1}{\sqrt{10}}$ and obvious phase jumps due to loss of the fringe signal in the MIDI data were masked out (phase jumps of several hundred μm within a few 10 ms can be found in the data and are definitely artificial and not caused by the atmospheric differential piston). The scaling was done in order to stay within the coherence length of the light source, the factor of $\frac{1}{\sqrt{10}}$ relates to $\frac{1}{10}$ in the power spectrum. Again, the anticipated piston sequence (red) and the measured phase sequence (black) were compared (see Fig 2.37).

The red curve was shifted horizontally and vertically to match the black curve at the beginning of the 2 curves. This piston sequence has apparently higher frequency components (see also the respective power spectrum, Fig. 2.38). There are a few distinct mismatches between the anticipated sequence and the measured sequence, for example the jumps at 48 s and 90 s

and the peak at 157s. These are caused by large slews and the data reduction software (see section 2.5.2). Note though, that in the parts in between the dynamic behavior matches nicely.

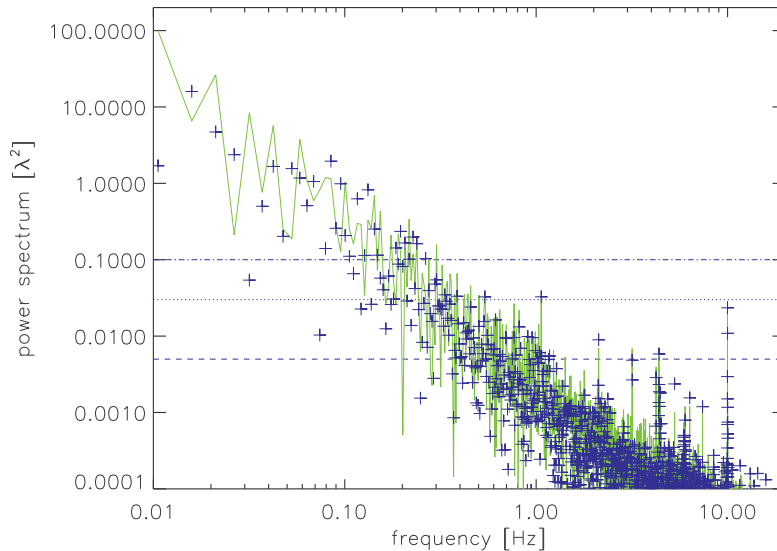


Figure 2.38: Comparison of the Fourier power spectra of the anticipated (blue crosses) and measured (green line) sequence (see Fig. 2.37). The measured piston sequence was obtained by W. Jaffe with the MIDI instrument installed at the VLTI (private communication).

The two power spectra presented in Fig. 2.38 agree at higher frequencies. At low frequencies one can find deviations, yet most of these are likely caused by the phase jumps in the measurements.

2.6 Conclusions of the lab experiment

In this chapter the design, calibration and verification of the atmospheric piston simulator were presented. The fiber based design proves to be very flexible, yet there are a few caveats which need to be addressed carefully. The main problem is the high sensitivity of optical fibers to temperature variations. This effect needs to be quantified again in the LINC-NIRVANA integration hall prior to the final test of the LINC-NIRVANA fringe tracking system. It was shown though, that already a very simple thermal insulation reduces the effect significantly. If necessary, a more advanced thermal insulation scheme will reduce the influence of thermal variations on the noise floor. In addition, the thermal effects are very similar to the differential atmospheric piston and can be corrected as well by the LINC-NIRVANA fringe tracking system

Although optical fibers are known to be sensitive to mechanical vibrations as well, no such effect was observed during the calibration and verification of the atmospheric piston simulator lab experiment. This can be explained by the lack of mechanical vibration sources and the use of a vibrationally stabilized optical bench. The same conditions will apply for the verification of the fringe tracking system of LINC-NIRVANA .

The calibration of the phase modulating devices shows a nice linear behavior with increasing input signal. There are deviations between calibration curves obtained for different calibration signal frequencies. This could be interpreted as a dependence of the gain on signal frequency. On the other hand, the variance of the gains as determined for various low control sequence frequencies (see tables 2.1 and 2.2) is well below the gain fitting accuracy. The dependence on the signal frequency seems to be less pronounced for the fiber stretchers. This is expected by the information provided by the company from which the fiber stretchers were purchased.

There is no obvious physical reason why the EO-PMs should be more susceptible to the frequency of the applied signal. Nevertheless, the EO-PMs are optimized to operate at a lot higher frequencies ($\gtrsim 1$ GHz). Therefore, the complex impedance might have a non negligible influence. This effect needs to be further investigated.

The mean gains are given here:

Table 2.3: Mean gains for the calibrated phase modulating devices

device	gain $\left[\frac{\Delta\Phi[\lambda]}{V}\right]$	σ
EO-PM1	0.076	0.006
EO-PM2	0.0065	0.006
fiber stretcher 1	4.84	0.36
fiber stretcher 2	4.7	0.34

Finally, the operation of the atmospheric piston simulator was verified by applying a sinusoidal wave (in parallel and in antiparallel signal), a theoretic power spectrum and a realistic piston sequence obtained with the MIDI instrument. In all cases, the measured sequence matched the anticipated phase sequence very well (within the attainable precision).

Chapter 3

Fringe tracking verification

This chapter describes plans for verifying the LINC-NIRVANA fringe tracking system on LINC-NIRVANA itself. Since the integration of LINC-NIRVANA got delayed for various reasons, the verification could not be conducted within the time anticipated for this thesis. Thus, an outlook will be given.

Possible ways to integrate the atmospheric piston simulator lab experiment are discussed. Preliminary experiments and modifications for the lab experiment are described. This chapter will also cover some proposals for the fringe tracking system verification. Finally, a possible future use of the equipment within the so-called “zero OPD fiber” concept are examined.

3.1 Improvements to the lab experiment

The atmospheric piston simulator lab experiment is designed for easy integration onto the LINC-NIRVANA optical bench. A major aspect in this regard is the optical fiber based design. This will allow a very high flexibility with respect to possible interfaces between the lab experiment and the LINC-NIRVANA optical bench (see section 3.3 below).

The major part of the atmospheric piston simulator will be assembled on a transportable small optical board. This comprises the light source, the Y-coupler, the polarization controllers and the phase modulating devices (EO-PMs and fiber stretchers). This optical board can then be placed in any convenient position within the LINC-NIRVANA integration hall. In order to connect the atmospheric piston simulator, the optical fibers protruding from the fiber stretchers will be prolonged using additional, matched patch cords.

Two major modifications are required for an optimal operation in conjunction with LINC-NIRVANA. First, a proper concept for thermal insulation of the fibers and the integrated optical components needs to be designed and installed. As discussed in section 2.5.3, temperature variations along the optical fibers limit the absolute achievable precision of the controlled differential piston on minute timescales. A straightforward concept would include thermal shielding of the optical board by a properly insulated casing and thermal insulation of the fibers using padded cable trays. This padding would also restrict mechanical vibrations affecting the fibers.

The second modification is more general. In the atmospheric piston simulator lab setup, a linear stage is used to remove larger ($\text{OPD} > 100 \mu\text{m}$) intrinsic static OPDs. There is no device with a similar dynamic range foreseen when integrating the atmospheric piston simulator on the LINC-NIRVANA optical bench. Therefore, additional steps need to be taken to alleviate large intrinsic OPDs.

As explained above, the fiber outputs of the atmospheric piston simulator need to be prolonged in any case to connect to the LINC-NIRVANA optical bench interfaces. Thus, it is planned to measure the absolute OPD between the two existing fibers with a precision of $\Delta\text{OPD}\approx 1\text{ mm}$. Then, a suitable set of customized polarization maintaining patch cords will be purchased. These have to be of sufficient length to connect the atmospheric piston simulator optical board with the LINC-NIRVANA optical bench interfaces, taking the thermal insulation concept into account, while making up for the intrinsic OPD in the original setup. The remaining $\Delta\text{OPD}\approx 1\text{ mm}$ can then be eliminated by a static signal on the fiber stretchers. They are capable of introducing a OPD of $\Delta\text{OPD}\approx 3\text{ mm}$ each (at a maximum input signal of 400 V).

3.2 Preliminary experiments on the LINC-NIRVANA bench

There are two main experiments which need to be carried out prior to the actual fringe tracking system verification. These tests are made necessary by the modifications to the atmospheric piston simulator.

Thus, the first experiment covers the verification of the thermal insulation concept. For this preliminary experiment, the current atmospheric piston simulator lab setup can be used. The lab setup can be installed on a bench in the LINC-NIRVANA integration hall. The atmospheric piston simulator fiber optics will be assembled on the foreseen optical board. After assembly of the thermal insulation, tests similar to those presented in section 2.5.3 have to be conducted in order to quantify the influence of the temperature effect on the long term achievable absolute precision.

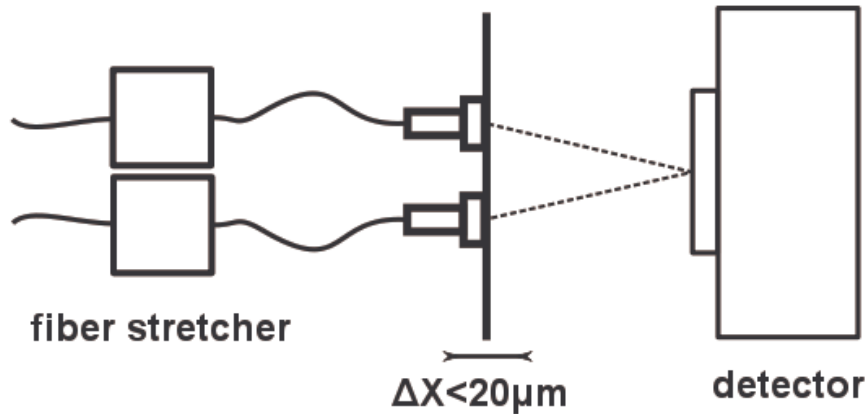


Figure 3.1: Concept of the “zero OPD” preliminary experiment. The 3D position of the fiber heads in the customized fiber port plate needs to be specified to less than $\pm 10 \mu\text{m}$. The fiber stretchers on the left will control the OPD to allow coherent overlapping of the two PSF on the detector on the right.

The second preliminary experiment will verify the modified OPD adjustment concept. The modified OPD adjustment concept foresees a combination of customized fiber path cords and the fiber stretchers to account for an intrinsic static OPD. An interface plate will be fabricated by the mechanical workshop in house. This customized interface plate will allow us to place the two patch cord ends, which determine the output of the atmospheric piston

simulator, in a common plane close to each other. This will effectively create an experiment comparable to Young's double slits (see Fig. 3.1).

Since the coherence length is rather limited (see section 2.3.2, typically 20-200 μm , see Fig. 2.5), interferometric fringes will be only observable if the fiber stretchers are capable of controlling the OPD near to zero OPD (and thus to make coherent combination of the two PSF possible). This experiment will allow to determine the DC signal, which has to be applied to the fiber stretchers, in order to reach and an OPD of $< 30 \mu\text{m}$.

3.3 Interfaces on the LINC-NIRVANA optical bench

There are three different possible interfaces between the atmospheric piston simulator and the LINC-NIRVANA optical bench: LINC-NIRVANA MAPS, the LINC-NIRVANA calibration unit or separate opto-mechanical posts in the SX and DX foci of LINC-NIRVANA. These three options are briefly described in this section, and advantages / disadvantages are discussed.

3.3.1 LINC-NIRVANA MAPS

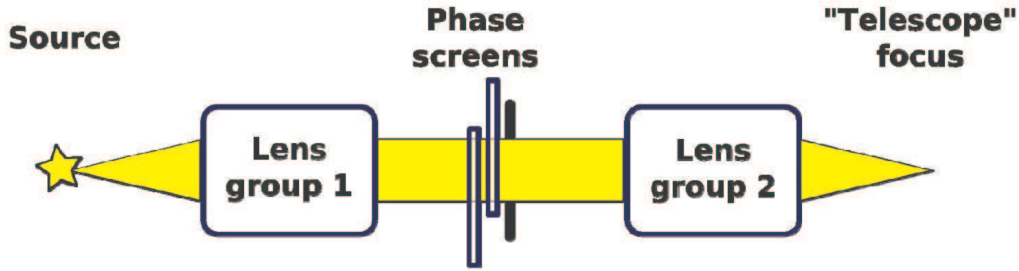


Figure 3.2: Concept of LINC-NIRVANA MAPS (Meschke et al. 2010).

LINC-NIRVANA MAPS (Multi-Atmosphere Phase screens and Stars, Meschke et al. (2010)) is a device constructed to test and verify the LINC-NIRVANA multi-conjugate adaptive optics (MCAO). The concept is depicted in Fig. 3.2. Its main functionality is achieved using two custom rotating phase screens.

Fig. 3.3 depicts the current design of LINC-NIRVANA MAPS. MAPS is potential interface for the atmospheric piston simulator, since light sources of the reference star unit will be fiber fed. Thus, one of the existing fibers in each MAPS unit can simply be exchanged with the output fibers of the atmospheric piston simulator.

This approach has two advantages. First, the integration will be trivial. Second, this allows us to run MAPS and the atmospheric piston simulator in parallel. Thus, the entire MCAO in conjunction with the fringe tracking system can be tested and their operation can be verified. The main disadvantage is that the current design does not foresee overlapping the single-eye PSF of each arm on the fringe tracking camera, since MAPS was intentionally designed for MCAO verification. This needs some investigation and possibly minor modifications to MAPS. Fig. 3.4 depicts MAPS and the calibration unit on the LINC-NIRVANA optical bench.

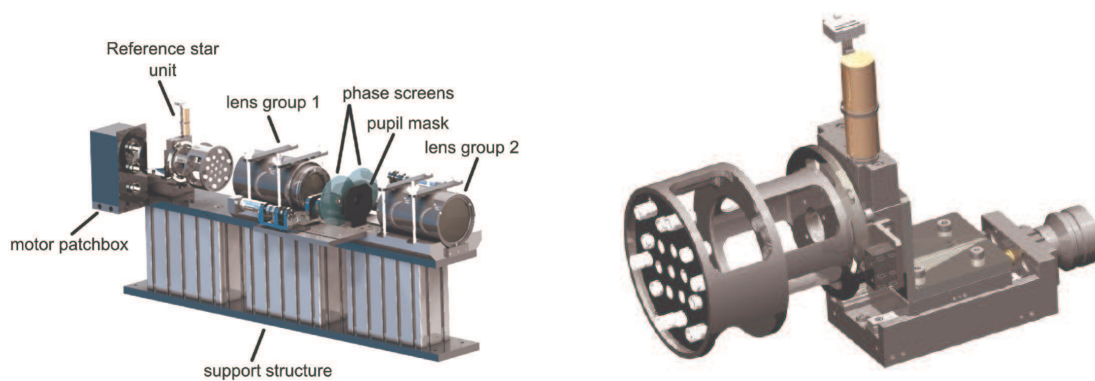


Figure 3.3: Design of MAPS. The left figure shows the entire device, while the right figure shows the rotating reference star unit (Meschke et al. 2010).

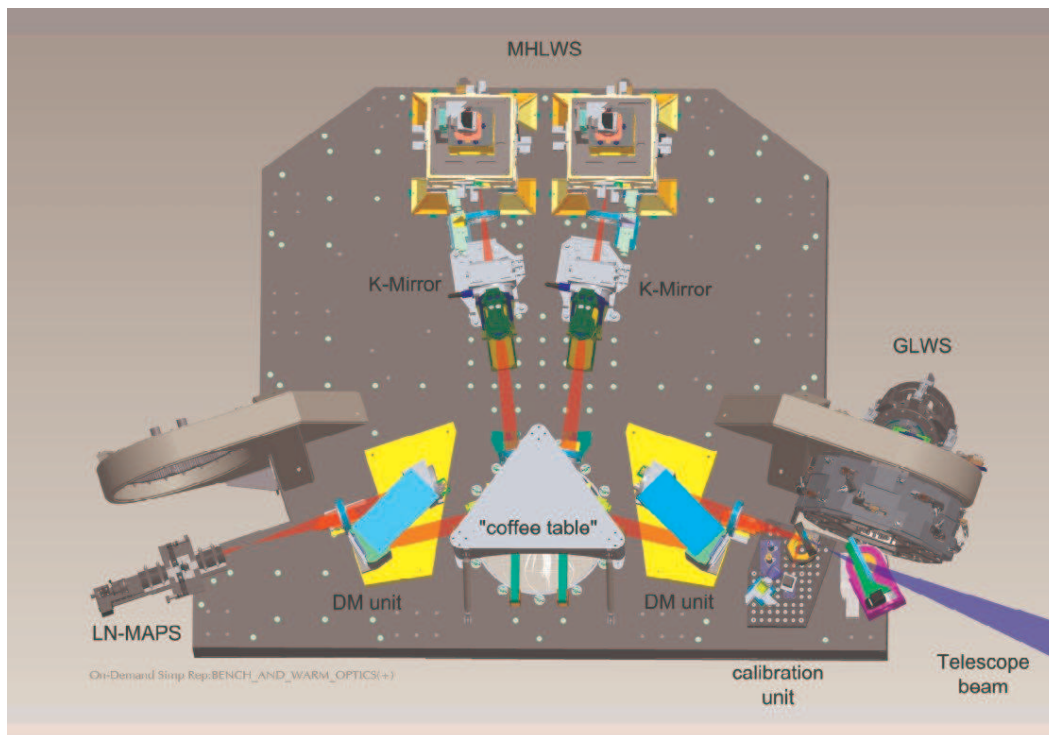


Figure 3.4: LINC-NIRVANA MAPS and the calibration unit on the LINC-NIRVANA optical bench (Meschke et al. 2010) (a temporary installation for lab testing).

3.3.2 LINC-NIRVANA calibration unit

The second option for a potential interface between the atmospheric piston simulator and the LINC-NIRVANA optical bench is the LINC-NIRVANA calibration unit (de Bonis et al. 2010). The calibration unit is a system which will be permanently integrated into LINC-NIRVANA. It consists of four separate sub-systems: the integrating sphere, the fibers plate, the absolute reference fiber and the phase diversity unit. For a detailed description of these sub-systems see de Bonis et al. (2010). Here, it suffices to mention that the fibers plate and the absolute reference fiber will have fiber ports which can accommodate FC/PC patch cords

(the fibers of the atmospheric piston simulator are all equipped with FC/PC connectors). Thus, placing the outputs of the atmospheric piston simulator in one of these fiber ports will be trivial. By design, each of these fiber ports resides in a nominal focus of LINC - NIRVANA . The separate sub - systems are individually addressed by a folding mirror, which resides on a rotational stage. See Fig. 3.5 for a design view of the calibration unit and Fig. 3.4 for its position on the LINC - NIRVANA optical bench. The advantage of this interface is that the PSF of the sub - systems will overlap in the detector focal plane by design. Yet, this option will not allow simultaneous operation of MAPS and the atmospheric piston simulator, since the folding mirror blocks the light from the focal plane where MAPS resides.

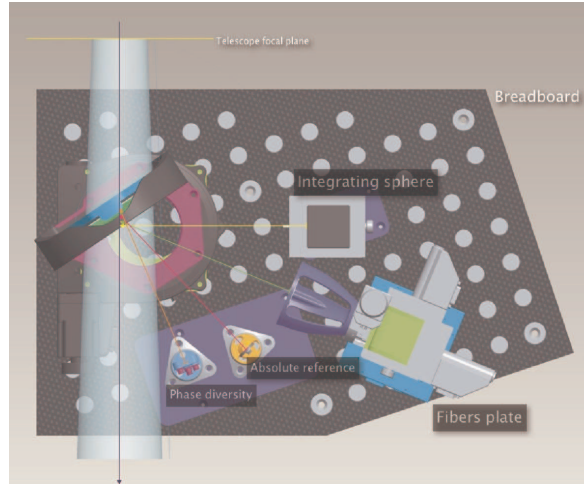


Figure 3.5: LINC - NIRVANA calibration unit (de Bonis et al. 2010).

3.3.3 A distinct opto - mechanical post

A third option would be to have a distinct opto - mechanical post in the straight or bent (calibration unit) focal points on the left and right side (SX & DX) of the instrument. This option would, with respect to the current design of the LINC - NIRVANA optical bench, be the least attractive, since it would require the most modification to the LINC - NIRVANA optical bench.

3.4 Verification scenarios

Since the input of the atmospheric piston simulator is entirely software based, it will allow us to address various calibration and verification tasks. The simplest calibration task will be to introduce a coherent superposition of its two output PSF. The next step would be to introduce a simple and well defined piston sequence, e.g. a sinusoidal or a triangular wave. This will allow verification of the response of the fringe tracking system.

The final verification test will comprise various tests. It is possible to introduce theoretical piston sequence of any desired power spectrum or to use measured piston sequences obtained with other instruments / observatories. In order to make the verification process even more realistic, it is foreseen to apply two separate and uncorrelated (with respect to each other) power spectra: a power spectrum of the atmospheric differential piston and one of the structural vibrations obtained within the OVMS campaign (see section 1.3). Since the AD

converter card used for controlling the phase modulating devices possesses 4 analog outputs, all four devices can be addressed in parallel. The ultimate verification experiment would be to combine this with simultaneous operations of MAPS.

3.5 Fringe tracking verification - the end?

The atmospheric piston simulator is not a permanent installation on the LINC-NIRVANA optical bench. Rather, it is foreseen to be used for the instrument verification in the LINC-NIRVANA integration hall. Therefore, it will be disassembled after the AIV phase is successfully completed. Yet, this will not necessarily prove to be the end of the phase modulating devices. A possible reincarnation is shown in Fig. 3.6. The absolute reference fiber or zero OPD fiber is a sub-system foreseen in the calibration unit of LINC-NIRVANA. It is designed to provide a zero OPD reference signal for calibrating the fringe tracking during operations at the LBT, i.e. before opening the dome in the evening. Yet, the design phase is not completed yet. The scheme shown in Fig. 3.6 shows a possible configuration. Light from a coherent light source is injected into a fiber. The light is split by an X-coupler and sent to the reference ports. In order to account for a varying OPD, there are fiber stretchers in each arm. A small portion of the light will be reflected from the polished ends of the output fibers. The corresponding signal can be acquired by detector which will feed a feedback loop to control the fiber stretchers and thereby keeping the two fiber references at true zero OPD. A concept is given in Fig.3.6.

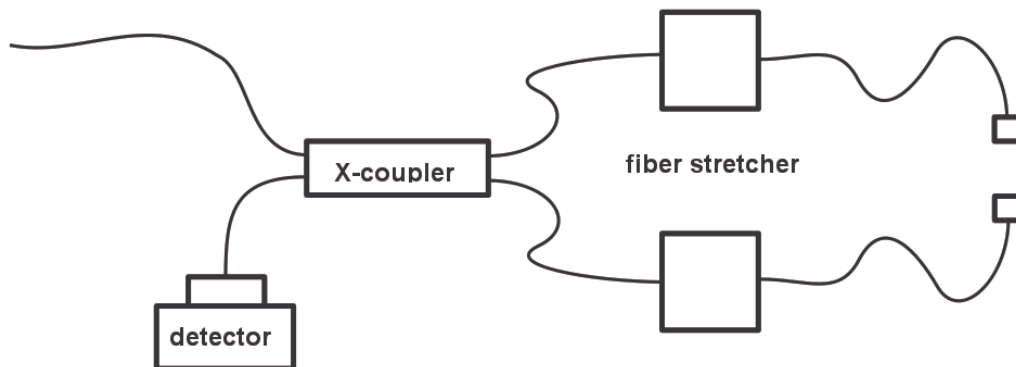


Figure 3.6: Concept for a zero OPD absolute reference. A small fraction of light will be reflected by the fiber outputs on the right. The reflected signal can be recorded by the detector. The acquired signal will be used as input in a feedback loop to control the fiber stretchers.

Chapter 4

Massive young stellar objects and interferometry

The previous chapters focus on the design and assembly and integration of the atmospheric piston simulator. It will serve as a tool for the fringe tracking system of LINC-NIRVANA . LINC-NIRVANA , as an interferometric imager, will allow high spatial resolution imaging of various objects and, thereby, allow a new look on the universe and our astronomical neighborhood.

In various fields of astrophysics, high spatial resolution observations are mandatory to connect theoretical predictions with actual measurements of the predicted quantities. One of these fields is the formation and early evolution of stars. In principle, the formation of low-mass stars is understood, yet many details of the associated processes remain ambiguous. Therefore, observations of the vicinity of young stellar objects can significantly improve our understanding of star formation and the formation of the close stellar environment, i.e. planet formation. The second part of this dissertation presents interferometric observations of massive young stellar objects with the MIDI instrument installed at the Very Large Telescope Interferometer (VLTI).

4.1 Formation of high mass stars

Massive stars play a very important role in shaping their surrounding interstellar medium and even the universe itself. They are the main production facilities for heavy elements in the universe due to the processes associated with their violent death in supernova explosions. Massive stars shape their interstellar neighborhood at all stages of their evolution: during their birth by strong outflows, later by winds and the UV radiation they emit, and finally by the shock fronts exerted by the supernova explosions. These processes are believed to trigger star formation shocks fronts, while the UV radiation can effectively hinder star formation via photo-evaporating the molecular gas reservoirs. Yet, despite their very important role in shaping galaxies, their formation and their first evolutionary steps are little understood (Zinnecker & Yorke 2007). A star is considered massive in that respect, if its mass exceeds $\approx 10 M_{\odot}$. Then, the stars mass will exceed the Chandrasekhar mass after its post-main-sequence phase, and thus the star ends its existence in a supernova...

The formation of lower mass is quite well understood. The natal molecular cloud collapses first to cold dense cores (or filaments) by gravo-turbulent cloud fragmentation (Klessen 2004). These cold cores collapse further due to gravitation, while they start to accrete more

and more material of their natal cloud. Due to conservation of angular momentum, disks are formed. Material then accretes both directly from the envelope onto the proto-star and onto the disk, in which the material is transported inwards by viscous friction. To lose the acquired angular momentum, disk winds are formed which launch jets perpendicular to the disk. The natal envelope disappears and when the gravitational pressure is large enough in the core, nuclear fusion ignites and the new low-mass star is born. Many of the most significant morphological structures were shown to exist in low mass young stellar objects, i.e. disks and outflows. This observational evidence supports the theoretical models.

The evolutionary phases of stars are usually classified according to the scheme introduced by Lada (1987). His class I describes an evolutionary phase where the natal envelope still exists, yet a circumstellar disk already formed. Thus, the central object is still accreting. These objects are usually called young stellar objects (YSOs). In that terminology, massive young stellar objects (MYSOs) are objects which in this evolutionary phase already exceed $8-10 M_{\odot}$. Unfortunately, MYSOs which show a “naked” disk (not obscured by an optically thick envelope) are rarely found. This is supported by the rather short disk destruction timescales. They are caused by the strongly increased UV photon emission of the central massive star once has reached the main sequence (e.g. Hollenbach et al. (1994, 2000)). Thus, in order to be able to draw a conclusive comparison between YSOs and MYSOs, the latter have to be observed when they still are surrounded by an optically thick envelope. This allows us to find circumstellar disks around them, which are not yet dissipated.

One of the central unsolved issues in the study of massive star formation is to which extent the accretion mechanism is comparable to the better-understood processes in low-mass star formation, e.g., accretion of material from a disk structure by the forming star at certain evolutionary stages (Zinnecker & Yorke 2007). Unfortunately, the optically thick envelope imposes severe observational constraints.

4.2 IR interferometry for assessing small spatial scales

This work assumes some knowledge of the reader on optical interferometry in astronomy, in particular technical terms commonly used within the scope of optical interferometry. There are some nice and comprehensible text books available on this subject for some years, e.g. Glindemann (2011). Since the MYSOs are usually deeply embedded, observations of the inner structures have to be done in the mid-infrared (MIR) or at even longer wavelengths. Second, the angular resolution of $\lesssim 100$ milliarcseconds (mas) in the MIR, necessary to reveal the inner structures, is not achievable even with 8 to 10 m-class diffraction limited telescopes. In addition, massive young stellar objects (MYSOs) are much rarer than their low mass counterparts and hence tend to be further away.

All of the above problems can be partially solved by near- and mid-infrared interferometry. If the natal envelope is already dissipated, near-infrared ($1-2.4 \mu\text{m}$) interferometry can resolve the warmest regions of the circumstellar dust disk and possible internal optically thick gaseous disks. Mid-infrared interferometry ($8-13 \mu\text{m}$) on the other hand can even peek through the thick dusty envelopes in which the MYSOs are embedded at earlier stages, resolving the inner morphology of the envelope and revealing the existence of disks within these envelopes.

On the other hand, analysis of the data obtained by interferometric techniques is complicated for several reasons. First, the proper data calibration is far from trivial. Even though

established data pipelines exist (e.g. MIA+EWS (Jaffe 2004) for the MIDI instrument (Leinert et al. 2003) installed at the VLTI), they usually cannot be applied in a straightforward fashion. This is mainly due to instrumental problems. For example, the measurements of the total flux (i.e. the spectrum) obtained with MIDI are sometimes questionable (see section 5.2). Furthermore, the analysis of the calibrated data brings several difficulties of its own. In principle, even though for example the interferometric instruments at the VLTI deliver spectrally-dispersed visibility data, each interferometric measurement associated with a projected baseline \vec{B} gives only information about the amplitude of the associated point in the normalized Fourier plane of the objects intensity distribution. The spectral information can be used to increase the Fourier plane ((u, v) -plane) coverage, since the spatial frequency is a function of wavelength. But this is only true under the assumption that one traces the same morphological structures at all wavelengths, an assumption which does not hold for example when strong spectral features are present. For instance, Weigelt et al. (2011) find that the emitting region of the Br_γ line is approximately a factor of 3 larger than the compact continuum emitting region in certain cases in MWC 297.

Several different approaches can be found to get conclusive insight from the observations. The most trivial one is fitting of simple geometric models. Simple geometrical morphologies like 1D or 2D Gaussians, uniform disks and rings, point sources, and halos yield either analytical or at least simple numerical solutions for the (u, v) -plane. Therefore, the parameters can be directly fit to the limited data and give an idea about the spatial distribution and asymmetries of the target’s intensity distribution. Since the models can be parametrized in angular coordinates, this method yields results which are unaffected by precise distance estimates of the target. A nice introduction is given by Berger & Segransan (2007).

A more advanced approach combines radiative transfer (RT) modeling methods with the interferometric observations. Yet, physically self-consistent RT models usually require many parameters, which are usually also correlated (see for example the *ttsre* code by Whitney et al. (2003b)). Additional data, taken for example at other wavelengths, or spectra can help to fix certain parameters. On the other hand, this method relies heavily on this additional information, its accuracy, as well as an accurate distance estimate (since the models are usually parametrized in distance units).

Since MIDI only uses two telescopes at a time, the information about the 2D phase spectrum of the intensity distribution is very limited. There is the “differential phase” observable in the MIDI data products (Jaffe 2004). Yet, due to the complicated treatment of the phase in the MIDI data acquisition process, the interpretation of the differential phase data is far from trivial. Qualitative statements about the connection between the differential phase and intensity distribution asymmetries have been made by Linz et al. (2008). In the near-infrared, Kraus et al. (2010a) recently achieved model-unbiased image reconstruction of VLTI/Amber data, but this instrument can combine the light of three telescopes coherently and is thus capable of measuring closure phase data, i.e. the sum of the phase over all 3 baselines.

4.3 Review of recent results

Infrared (near- and mid-infrared) interferometry is still a young field of observational astronomy. Interferometric observations of MYSOs have in fact been conducted for only ≈ 7 years. Therefore, the most recent results are briefly reviewed in this section to give an overview of the field. This will allow to put the results presented in chapters 5 and 6 into context with current research.

4.3.1 MWC 297

[Acke et al. \(2008\)](#) present VLTI/MIDI and Amber observations of MWC 297. They classify MWC 297 as a young massive B[e] star. Its distance is only 250 pc, which makes it one of the closest massive young stars. They fit various simple models to the near- and mid-infrared data separately. Their main conclusion is that a concentric combination of two geometric shapes gives better fitting results. The angular extent found in this way varies between 40 mas and 100 mas. Next, [Acke et al. \(2008\)](#) try to fit some more physical models, i.e. a dusty outflow or a passive disk, to the data. They conclude that none of these models is capable of fitting the SED data and the interferometric data at the same time. Finally, they show that an analytic model consisting of 3 concentric Gaussians is capable of reproducing the AMBER data, MIDI data and to some extent the SED. They thus can confine the distribution of circumstellar material. A central conclusion is that, since the interferometric data shows no signs of asymmetry, the inclination of the circumstellar disk should be less than 40° . This allows finally to resolve the $v \times \sin(i)$ ambiguity of the rotation of MWC 297. This lead [Acke et al. \(2008\)](#) to conclude that MWC 297 is indeed very close to its critical rotation speed.

[Weigelt et al. \(2011\)](#) observed MWC 297 recently with the AMBER high spectral resolution mode, which offers a spectral resolution of 12000 on the spectrally - dispersed visibility curves. They confirm the very low inclination angle of the circumstellar disk. The increased spectral resolution allows them to compare spatial scales of the source of the Br_γ emission and the continuum emission. They find that the region which is the source of the Br_γ emission is 3 times more extended than the continuum emission region. This indicates the presence of an extended disk wind.

4.3.2 IRAS 13481-6124

[Kraus et al. \(2010a,b\)](#) present for the first time model - unbiased image reconstruction from data obtained with VLTI/AMBER. They also use the radiative transfer models of [Whitney et al. \(2003b\)](#) (see Fig. 4.1). Nevertheless, substantial changes to the total dust mass and the location of the rim used in the radiative transfer models of [Whitney et al. \(2003b\)](#) were necessary to fit their data reasonably well, e.g. the near - infrared dispersed visibility curves.

4.3.3 NGC 2264 IRS1

[Grellmann et al. \(2011\)](#) present VLTI/MIDI measurements at 2 different baselines. One of the measurements was done using the SCI-PHOT mode (see the MIDI user manual¹ provided by ESO) in conjunction with the grism of MIDI. In the SCI-PHOT mode of MIDI,

¹<http://www.eso.org/sci/facilities/paranal/instruments/midi/doc/>

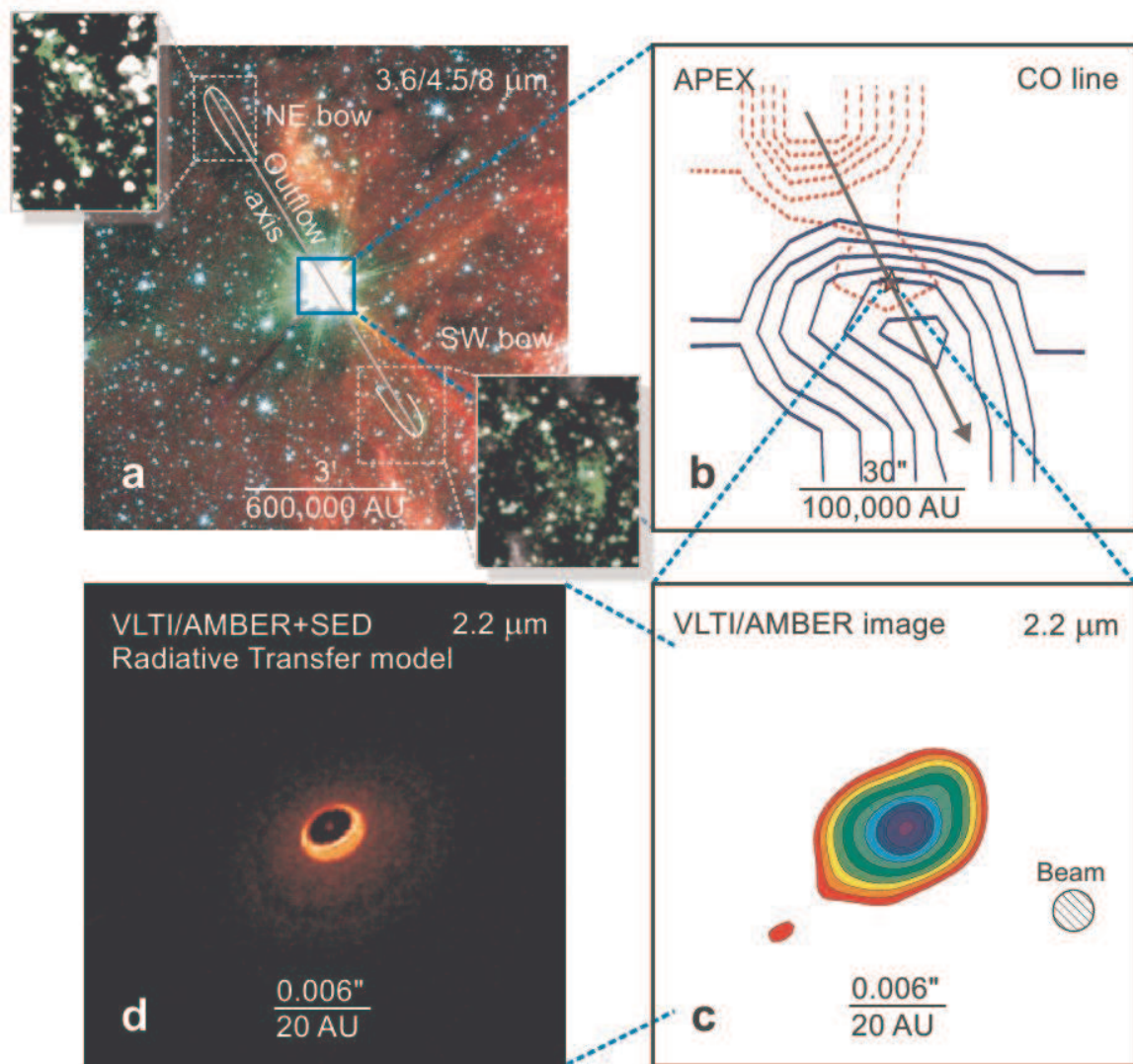


Figure 4.1: Zoom in on IRAS 13481-6124, covering spatial scales over more than five orders of magnitudes in: (a) In Spitzer/IRAC images, note the two bow-shock structures, indicating a collimated outflow. (b) The outflow is also detected in molecular line emission using APEX/SHFI on scales of a few 10000 AU (the contours show blue-shifted velocities of $10 \frac{km}{s}$ and redshifted velocities of $+5 \frac{km}{s}$, where the latter are indicated with dashed lines). (c) Model-independent aperture synthesis image of IRAS 13481-6124. Contours decrease from peak intensity by factors of $\sqrt{2}$ (d) The best fit radiative transfer model image. (Kraus et al. 2010a).

the correlated and the uncorrelated flux are measured at the same time, while the grism offers a much higher spectral resolution ($\frac{\lambda}{\Delta\lambda} \approx 230$) than the prism ($\frac{\lambda}{\Delta\lambda} \approx 30$). Since the (u, v) -plane coverage is very sparse, they only attempt to fit very simple (Gaussian and uniform disk) analytic models to each of the measurements separately. They also attempt to fit the SED and the interferometric measurements using two different radiative transfer codes, yet the quality of the fit is rather poor.

4.3.4 M8E-IR

Linz et al. (2009) present 7 measurements of M8E-IR with VLTI/MIDI. They show that there is some evidence in the data for an asymmetric intensity distribution of the target. However, the existence of a circumstellar disk in addition to an envelope is not certain due to the limited (u, v) -plane coverage. The combination of SED fitting using the *Online SED model fitter* (Robitaille et al. 2006) and the comparison of the radiative transfer code of Whitney et al. (2003b) leads them to the conclusion that the central object might be a cool but bloated star, a scenario suggested by Hosokawa & Omukai (2009)

4.3.5 W33A

de Wit et al. (2010) present measurements of W33A with VLTI/MIDI at 4 different baseline orientations. The extreme depth of the silicate absorption feature in W33A affects both the correlated and the total flux. The lower correlated flux drops below the detector noise level between $8.5 \mu\text{m}$ and $12 \mu\text{m}$ and can thus not be used for the analysis. They also attempt to use the radiative transfer code of Whitney et al. (2003b) for more physical modeling. Finally, they discuss how well the *Online SED model fitter* can predict specific morphological properties by comparing the results of the SED fitter to the interferometric measurements and information known from previous investigations of W33A.

Chapter 5

Kleinmann - Wright object Evidence for a circumstellar disk surrounding

This chapter discusses the results obtained in an investigation of the Kleinmann - Wright object (Kleinmann & Wright 1973 - also known as M17 SW IRS 1, hereafter KWO) within a large interferometric study of MYSOs with the Very Large Telescope Interferometer (VLTI) (Linz et al. 2008). Most of the targets were taken from a list of BN - type objects (Henning et al. 1984). The majority of results presented in this chapter have been published in Follert et al. (2010b).

5.1 Introduction to the Kleinmann - Wright object

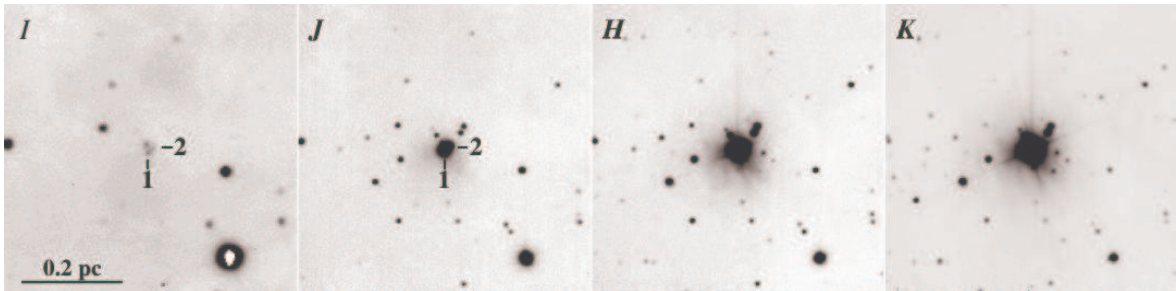


Figure 5.1: iJHKs images of the KW region (Chini et al. 2004). The KWO is the brighter component labelled 1 in the i and J band images.

Based on NIR spectroscopic data, Porter et al. (1998) classified the KWO as a transition object between a deeply embedded MYSO and a Herbig Be star. Chini et al. (2004) presented for the first time iJHK images, in which the KWO is clearly resolved into two separate sources. They determined a projected separation of $1''.2$, or 2650 AU, assuming a distance of 2.2 kpc. Chini et al. (2004) assumed that the second component (No. 2 in their paper) contributes a significant amount of flux only in the visual and near infrared wavelength regime. Here, the focus of the research is on the brighter component (No. 1, see Fig. 5.1). Furthermore, Chini et al. used multi-color photometric data, ranging from the Gunn i band to the MIR, and a TIMMI2 spectrum to fit a simple radiative transfer (RT) model, assuming a spherical dust

distribution. Due to excess in the infrared part of the spectral energy distribution (SED), they proposed that the KWO is a heavily embedded Herbig Be star, in agreement with the work of [Porter et al. \(1998\)](#).

This chapter presents new MIR interferometry for the KWO. The SED for this source was re-evaluated, based on 2D RT simulations. The statistics of the model parameters are discussed. Finally it is shown how the interferometric results can help constrain these parameters.

5.2 Observations and data reduction

The interferometric data were obtained with the MIDI instrument ([Leinert et al. 2003](#)) installed at the VLTI. The KWO was observed during five nights at five different projected baseline / projected angle configurations in the N - Band (8 - 13 μm). For the first three nights of observation (2005-06-24, 2005-06-26, 2006-05-18), the 8.2 m diameter Unit Telescopes (UTs) were used. For the other two nights, the 1.8 m Auxiliary Telescopes (ATs) were used for the observation. At the time of submission, the related paper ([Follert et al. 2010b](#)) represented the first published analysis of MYSO data using the ATs.

Table 5.1 lists the observations, dates, times, telescopes used, as well as the associated baseline lengths and orientations. The observations followed the procedure described in [Leinert et al. \(2004\)](#). MIDI was set to work in HighSens - mode. The beams from the two telescopes were first combined to determine the interferometric signal or correlated flux. While measuring the correlated flux, the optical path difference (OPD) is first changed on a coarser scale (some millimeters) to search for the interferometric fringes. Once they are found, the OPD is swept continuously around the zero OPD (the white light fringe) with an amplitude of approximately 80 μm at a frequency of a few hundred scans in three to four minutes. After the correlated flux is determined, the photometric signal (or uncorrelated flux, see Fig. 5.2) is measured.

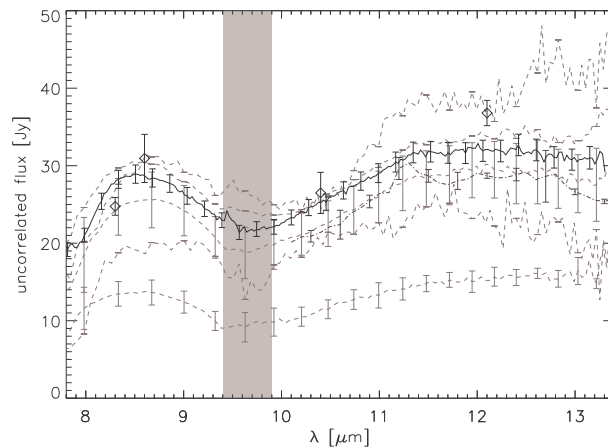


Figure 5.2: Photometry of the KWO. The dashed, gray lines depict the spectra as obtained by MIDI, the dash - dotted, dark gray line archival IRS data, the diamonds the N - band SED from [Chini et al. \(2004\)](#), and the bold, black line the spectrum used for further analysis. The vertical gray bar denotes the wavelength regime of the atmospheric ozone absorption feature, in which measurements are rendered unreliable.

In order to measure the total flux, the light from one telescope is blocked, allowing mea-

Table 5.1: List of observed objects. All objects other than the KWO are calibrator stars (see above). The objects marked with an asterisk are included in the subsequent analysis. See text for details. The third column lists the projected baseline in meters, the fourth column the projected angles (PA) east of north (EON). The last column lists the UT telescopes and the AT stations forming the baseline.

Object	Date and Time	B [m]	PA [°] E of N	UTs
HD107446*	2005-06-24T03:24:09	61.51	167.2	3-4
HD168415*	2005-06-24T04:22:42	62.34	108.6	3-4
HD169916	2005-06-24T07:04:18	56.89	127.4	3-4
HD169916	2005-06-24T07:59:14	52.06	138.1	3-4
KWO*	2005-06-24T08:23:34	43.87	140.7	3-4
HD169916*	2005-06-24T08:48:54	47.75	150.3	3-4
HD177716	2005-06-24T09:59:36	47.07	160.2	3-4
HD169916*	2005-06-26T00:49:52	55.84	-6.5	1-2
HD107446	2005-06-26T01:44:57	38.57	57.5	1-2
HD169916	2005-06-26T02:29:52	55.88	8.0	1-2
HD145544	2005-06-26T03:58:14	43.41	44.6	1-2
KWO*	2005-06-26T04:25:11	55.79	24.3	1-2
HD95272*	2006-05-18T00:36:17	46.63	43.4	2-3
HD169916	2006-05-18T04:07:17	43.99	10.4	2-3
HD101666	2006-05-18T05:41:02	26.03	58.0	2-3
HD120404	2006-05-18T06:42:24	28.96	100.1	2-3
HD120404	2006-05-18T07:36:18	25.98	114.7	2-3
HD168415	2006-05-18T09:27:57	44.99	47.8	2-3
KWO*	2006-05-18T09:59:02	43.52	48.4	2-3
HD169916*	2006-05-18T10:28:38	40.01	52.2	2-3
				ATs
HD150798	2006-08-09T23:30:24	31.6	65.6	D0-G0
KWO*	2006-08-10T01:27:29	31.7	69.6	D0-G0
HD211416	2006-08-10T01:52:18	31.5	22.6	D0-G0
HD168454*	2006-08-10T02:12:13	31.8	73.9	D0-G0
KWO*	2006-08-13T00:22:43	15.1	64.76	E0-G0
HD211416	2006-08-13T00:48:05	15.7	9.9	E0-G0
HD150798	2006-08-13T01:40:00	14.9	-81.7	E0-G0
HD150798	2006-08-13T02:46:00	14.2	-65.5	E0-G0
HD150798	2006-08-13T03:42:34	13.6	-50.7	E0-G0
HD206778*	2006-08-13T04:35:19	15.4	74.8	E0-G0

surement of the flux from the other and vice versa. During the recording of the photometric signal, chopping with a throw of $10''$ and a frequency of roughly 2 Hz is applied to remove the thermal background signal. Appropriate calibrator stars were observed in the same way immediately before and after the KWO (see table 5.1 for details), in order to account for instrumental effects which distort the visibility curve.

The MIDI prism was used as the dispersing element, providing a spectral resolution of $R \approx 30$. The data obtained with MIDI were first reduced using the MIA+EWS package (V1.5.1, see

<http://www.mpia-hd.mpg.de/MIDI/> or Jaffe (2004)), developed at the MPIA Heidelberg and the Leiden Observatory.

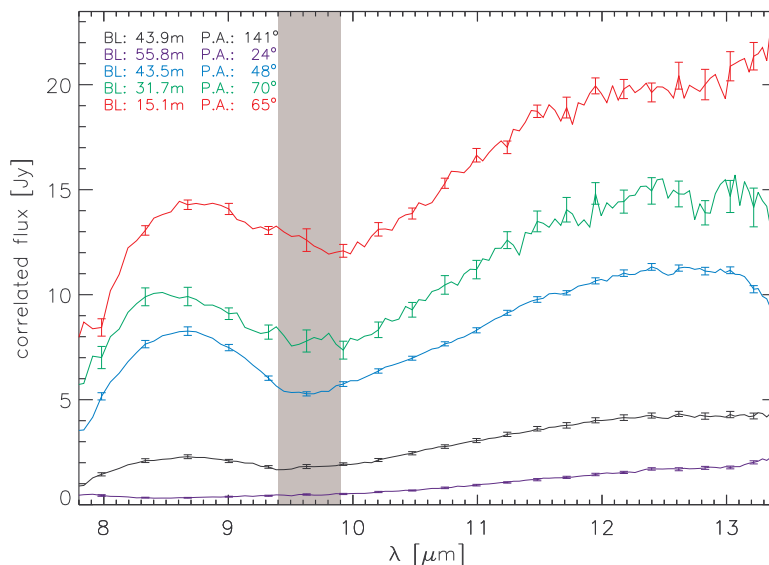


Figure 5.3: The measured correlated fluxes.

The photometry results, when calibrated with different calibrators belonging to one night of observation, were not consistent (see Fig. 5.2). This is a clear sign that the nights of observation were far from photometric. Hence, a different data reduction scheme was employed. First, the correlated fluxes of the KWO for each night of observation were determined and afterward calibrated by the corresponding set of correlated fluxes of the calibrator stars (see Fig. 5.3). The correlated flux is less affected by atmospheric emission, due to the differential recording technique. For determining the correlated flux, two subsequent 180° phase-shifted measurements are subtracted from each other. Due to the high fringe scan speed, the background is subtracted far more efficiently than by the chopping procedure. Accordingly, the variations in the correlated fluxes were negligible within the errors. The only exception are artifacts caused by the atmospheric absorption features (e.g. the ozone feature at $9.4\text{--}9.9\ \mu\text{m}$). If the science target and the calibrator are observed at different air masses, the calibrator will be more (or less) affected by the atmospheric absorption, which may result in emission- (absorption-) like artifacts in the calibrated correlated fluxes. Hence, only calibrators observed at air masses comparable to those of the KWO were taken into account for the subsequent analysis (marked with an asterisk in table 5.1). Nevertheless, the correlated fluxes in the wavelength range covering the ozone feature might still be slightly affected; hence, these data are neglected for the subsequent analysis. In order to deduce the calibrated visibilities, the calibrated correlated fluxes need to be divided by the calibrated total flux (i.e. $8\text{--}13\ \mu\text{m}$ the spectrum).

In order to avoid the spectrum obtained by MIDI under non-photometric conditions, TIMMI2 data (see Fig. 5.2, solid bold black line) were used instead. The ESO archive contains mid-infrared grism spectroscopy of the KWO between 8.0 and $13.0\ \mu\text{m}$ obtained with TIMMI2 (Reimann et al. 2000) with a nominal spectral resolution of 230. The observations were performed within the ESO programme 71.C-0185(A) on July 25, 2003. Using a slit width of $1''.2$, the measurements were done with chopping and nodding throws of $10''$. The star HD169916

served as a spectrophotometric standard. For the re-reduction of these data, the TIMMI2 pipeline of [Siebenmorgen et al. \(2004\)](#) was used. The same spectrum was used for the subsequent SED fitting. For that purpose, the data were re-sampled to match the wavelength grid used by the Online SED model fitter ([Robitaille et al. \(2007\)](#), see also section 5.3.1).

Furthermore, archival *Spitzer* IRS data and the SED of [Chini et al. \(2004\)](#) complemented the spectral information. The post-basic calibrated IRS data (Request Key 11546624, PI M. Wolfire) was reduced with the standard software version 15.3.0 and subsequently re-binned. The KWO is quite luminous in the infrared. Thus, the *Spitzer* IRAC imaging frames covering the spectral range from $3.6\ \mu\text{m}$ to $8.0\ \mu\text{m}$ are overexposed. There are no non-saturated *Spitzer* MIPS data at $24\ \mu\text{m}$ of the KWO and, unfortunately, no (sub-) millimeter continuum data are available either.

The SED used in the subsequent analysis is summarized in table 5.2. For the error analysis, variations in the correlated flux (during one measurement cycle) as specified by the data reduction tool were taken into account, as well as the error specified for the TIMMI2 spectrum. If more than one calibrator provided usable data, the respective visibility curves were finally averaged.

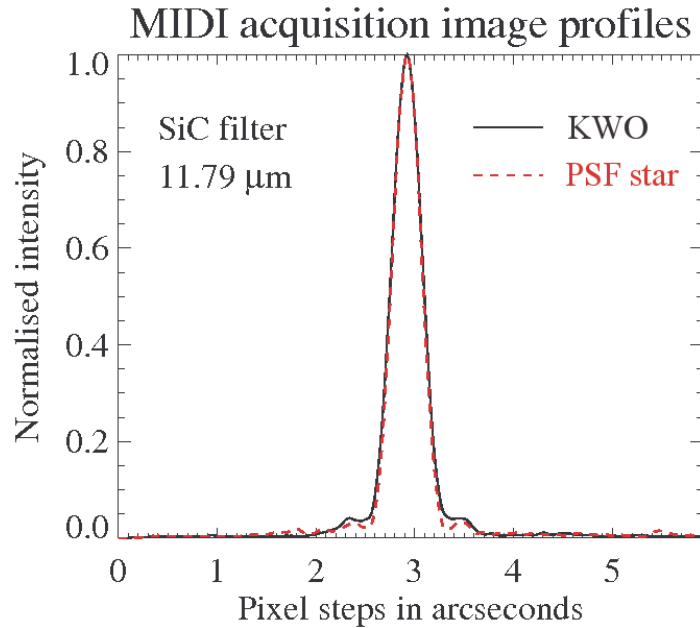


Figure 5.4: Comparison between radial cuts of image profiles of the KWO and the calibrator star HD169916, derived from MIDI UT acquisition images.

In addition to the interferometric data, acquisition images from the UT measurements at $11.8\ \mu\text{m}$ were taken as well. After background subtraction, the profile of the science target is compared to that of a calibrator star. They overlap very well, which is remarkable since the observation of the calibrator clearly has better adaptive optics correction (on-source guiding). Hence, the KWO is not resolved in the MIR with single 8 m-class telescopes (see Fig. 5.4).

Table 5.2: Flux densities of the KWO.

wavelength [μm]	F_ν [mJy]	σ_{F_ν} [mJy]	aperture arcsec	data source
0.8	0.025	0.005	2	Chini et al. (2004)
1.25	7	1	2	Chini et al. (2004)
1.65	91	9	2	Chini et al. (2004)
2.2	550	60	2	Chini et al. (2004)
3.9	4400	1000	2.5	Chini et al. (2004)
4.4	9700	4500	18	MSX B (archive)
4.6	5800	1500	3	Chini et al. (2004)
8.06	22920	930	1.2	TIMMI2
8.50	28890	1180	1.2	TIMMI2
8.97	26670	1090	1.2	TIMMI2
9.44	24110	1030	1.2	TIMMI2
9.95	22310	940	1.2	TIMMI2
10.49	25920	1080	1.2	TIMMI2
11.05	29510	1240	1.2	TIMMI2
11.65	31450	1320	1.2	TIMMI2
12.27	31730	1380	1.2	TIMMI2
12.93	31090	1370	1.2	TIMMI2
14.7	33070	1650	18	Chini et al. (2004)
17.8	55488	13900	5	Chini et al. (2004)
21.3	68760	3440	18	Chini et al. (2004)
23.04	105000	6100	12	IRS
26.96	129000	5900	12	IRS
31.56	156000	7100	12	IRS

5.3 Analysis of the spectral and interferometric data

The analysis of spectrally dispersed visibility curves is non-trivial. Analytical numerical models can only be found if one assumes very simple models and/or geometrical shapes. For this reason, the SED was fitted to pre-calculated models. The set of parameters which describe the respective model is then used as input for a Monte Carlo radiative transfer model. The resulting synthetic images are finally Fourier-transformed in order to produce synthetic visibility curves which can be compared to the measurements (Linz et al. 2009).

5.3.1 SED fitting

The SED data (see table 5.2) served as input for the Online SED model fitter¹ (Robitaille et al. 2007). The fitter is based on a grid of 200,000 pre-calculated, 2D Monte Carlo radiative transfer (MC RT) models computed with the code of Whitney et al. (2003a). Each of these models is characterized by a set of 28 parameters, which are not all independent of each other (for details see Robitaille et al. (2006) and Robitaille (2008)). The models include the properties of the central object (mass, radius, temperature), the envelope (accretion rate, outer radius, inner cavity density and opening angle), the disk (mass, inner and outer radius, accretion rate, scale height factor, flaring angle) and the ambient density. These parameters

¹<http://caravan.astro.wisc.edu/protostars/index.php>

have been varied to cover a large range of possible configurations of young stellar objects, yet the parameter volume is not covered uniformly. The result is a first grid-like set of 20,000 models. For each of these models, the SED was calculated for 10 different inclination angles (defined between the axis of symmetry of the model and the line of sight), distributed equally over the cosines of the inclination angle. Hence, the final grid consists of 200,000 models. The grain model used consists of a mixture of astronomical silicates and graphite in solar abundance, where the optical constants are taken from [Laor & Draine \(1993\)](#). In addition, the optical properties are averaged over the size distribution (taken from [Kim et al. 1994](#)) and composition. For further details see [Robitaille et al. \(2006\)](#).

In addition to the SED, the user of the Online SED model fitter is required to specify some assumptions on the distance and interstellar extinction toward the object as input for the Online SED model fitter. These assumptions are treated as boundary values in the fitting procedure. The fitter then performs a global χ^2 minimization procedure to evaluate which parameter combination fits the observed SED best. The results are presented ordered by increasing deviation between the modeled and specified SEDs. For each of these models, a parameter file is available which contains the set of parameters describing this particular model. These files then serve as input to the Monte Carlo radiative transfer code of [Whitney et al. \(2003a\)](#).

Figure 5.5: Best SED fits, obtained with the Online SED model fitter. The black solid line corresponds to the best fitting model and the gray lines to the nine next best fits. The dashed line shows the stellar photosphere model with the best-fit interstellar extinction taken into account. The dots and triangles represent the data the fit was applied to; dots denote regular data points and triangles upper limits, respectively.

For this work, the distance and the interstellar extinction were chosen in accordance with [Chini et al. \(2004\)](#), who proposed a distance $d = 2.2$ kpc and a total visible extinction of $A_v \approx 24$ mag, including extinction due to both the intervening interstellar matter and the local circumstellar structures. The recent re-determination by [Hoffmeister et al. \(2008\)](#), who found $d = 2.1 \pm 0.2$ kpc for the M17 SW star cluster, was also taken into account. Hence, $d = 1.9$ - 2.3 kpc is adopted as boundaries for the fitting procedure, while the interstellar extinction was assumed to be larger than 5 mag. Note that the distance, the interstellar as well as the total extinction are treated as free parameters (within the boundaries). Figure 5.5 presents the ten best SED fits.

The *Spitzer* IRS data were considered as upper limits. There will be a significant contribution to the luminosity by the interstellar material surrounding the KWO, due to the much larger aperture of IRS ($\approx 11''$) at these wavelengths. Apparently, the fitted curve overestimates the flux at 3.9 and 4.6 μm . In order to assess the result, the SED fitter was run again, including each data point shortward of 8 μm twice. The resulting set of solutions indeed involves some spectra which agree on the relatively low flux at 3.9 and 4.6 μm . Yet, all these solutions cannot account for the pronounced silicate feature (see Fig. 5.2). In addition, a MSX B2 data point from the archive is included. Due to the uncertain calibration of the MSX B2 data, the associated error is large; hence, it does not have a strong effect on the SED fit. Nevertheless the MSX B2 flux and the best fit match quite well. Hence, the result is kept as presented in Fig. 5.5.

The compiled SED used for this work is based on data covering the peak and Wien side of the SED. No published data exist for the Rayleigh-Jeans part, which could distinguish KWO from the surrounding high level of extended (sub-) millimeter flux present in the M17 SW region. Therefore, the SED of KWO is not constrained at far infrared and submm wavelengths, and several model configurations fit the observed optical / infrared SED almost equally well. For this reason, a statistical approach to constrain the meaningful parameter space was adopted (see Sec. 5.4). Histograms were created of the different model parameters (accounting for the 1000 best fitting models), with each count weighted by $1/\chi^2$. High densities in the respective parameter space hence give an indication of the probability that a certain parameter will have a value in the associated range.

5.3.2 Radiative transfer modeling and synthetic visibilities

For the 10 best-fitting configurations, MC RT simulations were performed using the TTSRE code of [Whitney et al. \(2003a\)](#). The simulation was run each time using a total of 100 million test photons. The MC RT was modified code for that purpose by defining eleven narrow filters centered at equally spaced wavelengths covering the N-band. Hence, for each model, eleven synthetic images were obtained. Figure 5.6 shows an example of the frames created by this procedure. Three synthetic images at different wavelengths create an RGB composite ($\lambda_{red} = 12.5 \mu\text{m}$, $\lambda_{green} = 10.5 \mu\text{m}$ and $\lambda_{blue} = 8.5 \mu\text{m}$). In addition, logarithmic intensity scaling is applied in order to reveal the diffuse outer regions of the structure. The picture was adaptively smoothed to reduce the graininess inherent to Monte Carlo simulations.

Each of these synthetic images was first embedded in a larger, empty frame, since the MCRT code only allows for a certain spatial resolution in combination with a respective maximal spatial outer scale. Then, each image was Fourier-transformed in order to obtain the related (u, v)-spatial frequency spectrum. Due to the increased spatial outer scale, the resolution

in Fourier - space was refined, which in turn helped to avoid numerical discretization effects.



Figure 5.6: Synthetic RGB composite image for model 3003929 (see Table 5.5) at an inclination angle of 75° . The $12.5\ \mu\text{m}$ bin is depicted in red, the $10.5\ \mu\text{m}$ bin in green and the $8.5\ \mu\text{m}$ bin in blue. The total visible area is 1200×1200 AU.

Next, the Cartesian coordinates of the (u, v) -plane were transformed to polar coordinates. The synthetic visibility curves were constructed by adopting the values from the synthetic (u, v) -spectra from each of the respective wavelength bin images at the spatial frequencies corresponding to the projected baselines used in the observations. There is one remaining degree of freedom: while the inclination angle i is fixed due to the SED fitting and the respective MCRT modeling, the symmetry axis of the synthetic images runs north-south, which is not necessarily true for the science target. Hence, an additional angular parameter is required to account for the observed position angle. This parameter was derived by minimizing the deviation between the synthetic visibility curves and the measured visibility curves by rotating the $u-v$ plane. Hence, for each model spectrally dispersed, synthetic visibility curves were obtained at the projected baselines used for the observation. These will be compared to the measured visibilities in 5.4.4.

This approach is similar to de Wit et al. (2010), who studied the MYSO W33A. They use the RT models of Whitney et al. (2003a) to generate synthetic visibility curves as well. Note that de Wit et al. (2010) were able to constrain various model parameters in advance, due to better availability of data for W33A, especially in the submm wavelength range.

5.3.3 Interferometric observations

The measured calibrated dispersed visibilities appear in Fig. 5.7. The depicted errors represent 3σ . The visibility amplitudes are smaller than unity for all observations. Hence, the KWO is clearly resolved on all baselines. Moreover, the silicate absorption feature which is visible in the total intensity spectra is not seen in any of the visibility curves. This is due to the fact that the relative depth of the feature is similar in both the correlated and the total flux spectrum. Since the same effect is observed in every visibility curve, although they are measured on clearly distinct baseline lengths, this indicates that the absorbing dust is situated in foreground structures not directly associated with the KWO. The existence of such a dust screen in front of the KWO was already proposed by [Chini et al. \(2004\)](#) and [Porter et al. \(1998\)](#), who suggest that the KWO might actually be located behind the SW obscuration of M17.

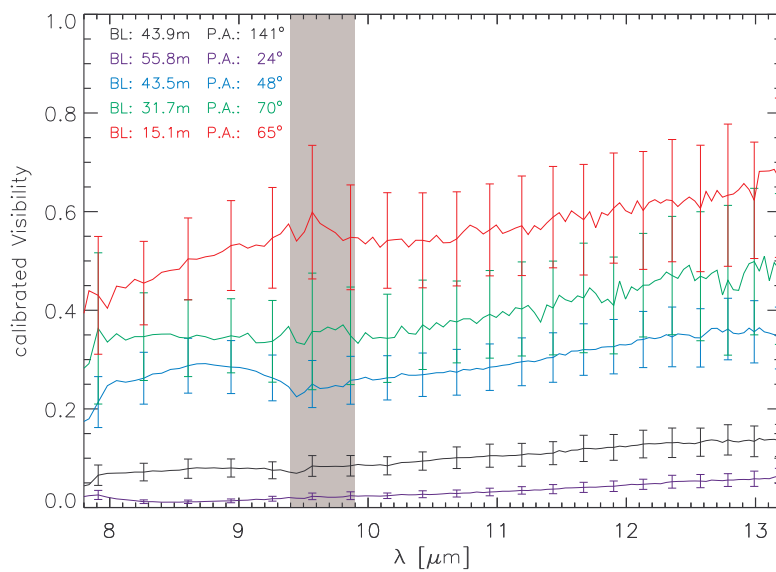


Figure 5.7: Calibrated visibility curves. See text for details.

5.4 Discussion

5.4.1 Statistical reduction of the parameter volume for the SED fits

SED data fitting of MYSOs is in general ambiguous. In order to investigate how the observational errors translate into variations of the RT model parameters, an approach comparable to [Pinte et al. \(2008\)](#) was adopted. Note that the histograms (see section 5.3.1) represent the distribution of the respective parameters taken from the set of the 1000 best-fitting models as obtained from the Online SED model fitter. No *a priori* assumptions were involved.

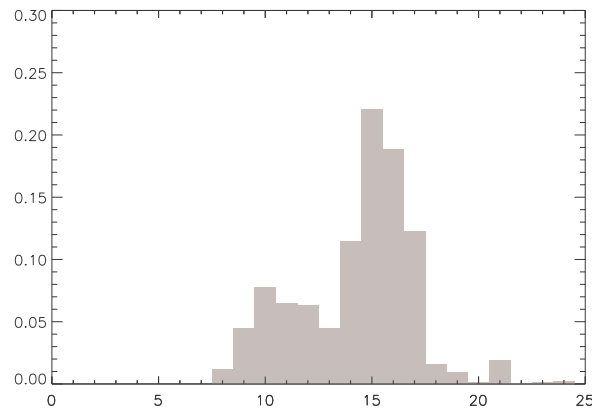


Figure 5.8: Distribution of the stellar mass. The ordinate gives the fractional occurrence of the values.

The stellar properties

Figures 5.8 and 5.9 show the distribution of the fitted stellar mass and temperature, respectively. The fitted stellar temperature is strongly peaked around 32000 K. The stellar mass distribution is peaked around $15 M_{\odot}$, with a side lobe towards $10 M_{\odot}$. Hence, the most probable embedded star for the KWO would be an early B star.

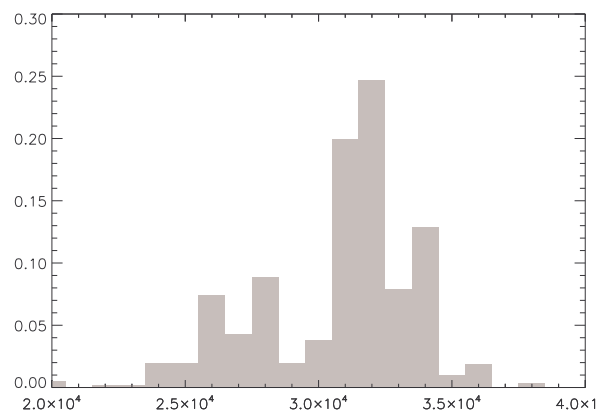


Figure 5.9: Distribution of the stellar temperature. The ordinate gives the fractional occurrence of the values.

Disk and envelope

Figure 5.10 plots the envelope accretion rate. It is interesting to note that most of the models fitting the SED have no envelope at all: these models consist of the central star and a disk only. In the [Robitaille et al. \(2007\)](#) models, this is denoted by setting the envelope accretion rate formally to zero. This is in contrast to [Chini et al. \(2004\)](#) who fit the SED with

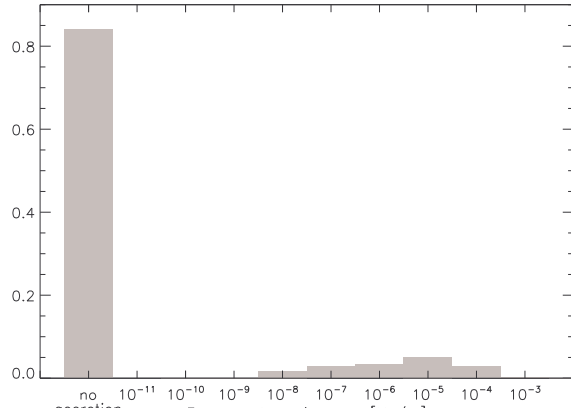


Figure 5.10: Distribution of the envelope accretion rate. The ordinate gives the fractional occurrence of the values.

a spherical dust distribution with a radial density profile varying as $r^{-0.5}$, which might be interpreted as an envelope-like structure. Due to the inability of this approach to properly reproduce the silicate feature, one of their suggestions was a disk-like structure, which would produce silicate features both in emission and absorption, depending on the disk orientation. [Chini et al. \(2004\)](#) identify the reflection nebula surrounding the KWO with this spherical dust distribution. The arguments made above and the interferometric measurements (see sections 5.4.3 and 5.4.4) favor a configuration without a small-scale optically thick dust shell directly enveloping the KWO. Thus, the scattering material in the reflection nebula is probably not bound to the KWO itself. Instead, this suggests that the reflecting material is either a remnant of the natal molecular cloud or it is situated in front of the KWO along the line of sight (as already proposed by [Porter et al. \(1998\)](#)).

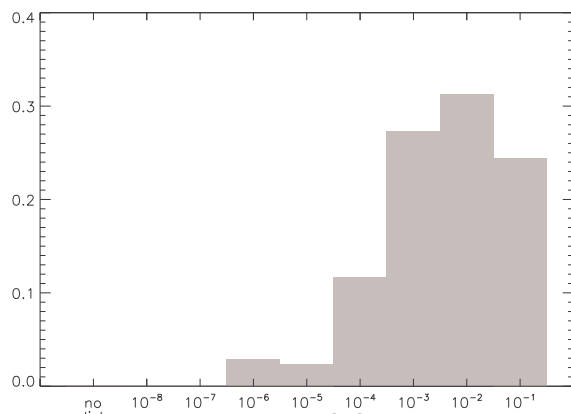


Figure 5.11: Distribution of the disk mass. The ordinate gives the fractional occurrence of the values.

Figure 5.11 shows the histogram of disk masses. The configurations with a disk of intermediate mass (10^{-3} to $10^{-1} M_{\odot}$) are most probable. Note though, that (sub-)mm data with sufficient angular resolution are not available. Only such observations would give the total mass of circumstellar material by measuring the optically thin thermal dust emission. Without such data, any assumptions on the mass of the circumstellar material will be model dependent.

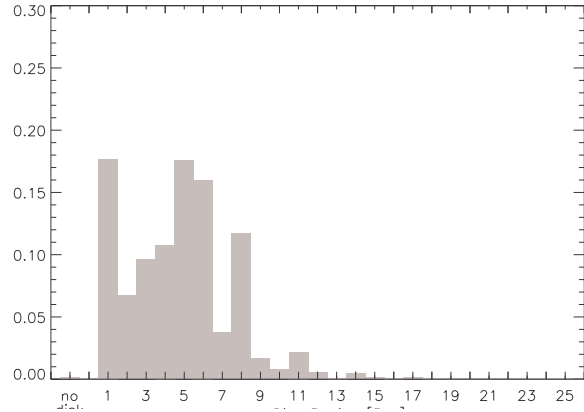


Figure 5.12: Distribution of the Disk inner radius (in units of the dust sublimation radius) model parameter. Values of -1 correspond to envelope-only models. The ordinate gives the fractional occurrence of the values.

Figure 5.12 shows the corresponding inner radii of the proposed disk structure, in units of the thermal dust sublimation radius. It is interesting to note that the most probable inner radii are larger than the dust destruction radius. This result is roughly consistent with the relation between the total luminosity and the source size as established by [Millan-Gabet et al. \(2007\)](#). However, the radius of the best-fitting model (Sect. 5.4.4 table 5.3) exceeds the dust sublimation radius by a factor of two, suggesting ongoing inner disk dispersal by UV photo-evaporation and/or stellar winds.

5.4.2 Object models from the SED Fitting

As a result of the SED fitting, four slightly different model configurations were obtained with various inclination angles which resemble the measured SED best (see table 5.2). Table 5.3 summarizes the most important structural parameters. A more detailed overview can be found in table 5.5.

All of these model configurations consider a disk only; hence, no additional circumstellar material is needed to account for the near and mid-infrared fluxes. The central object is in every case quite massive. According to [Martins et al. \(2005\)](#), the objects can be classified as early B stars. The disks themselves are massive as well, yet the distance of the inner rim to the central object differs considerably. Since the inner radius is directly related to the spatial distribution of the dust and, therefore, to the spatial intensity distribution, this should allow us to distinguish the different models when comparing the synthetic and measured visibility curves. Note, that an outer scale for the disk is explicitly not specified, since the data are not capable of confining the size of the disk in a model-independent way.

Table 5.3: Parameters and derived quantities of the models. Note that these are disk-only models.

parameter	Grid Model Number			
	3003929	3005903	3008813	3012934
stellar mass [M_{\odot}]	15	16	16	14
stellar temperature [K]	31300	32300	32200	30500
disk mass [M_{\odot}]	9×10^{-2}	4×10^{-2}	2×10^{-2}	6×10^{-2}
disk inner radius [AU] ($[R_{\text{sub}}]$)	26 (2.2)	84 (6.4)	99 (7.7)	55 (5.1)
disk accretion rate [M_{\odot}/yr]	7.8×10^{-8}	3.0×10^{-6}	2.2×10^{-7}	4.9×10^{-7}
Luminosity [L_{\odot}]	20.7×10^3	25.9×10^3	25.0×10^3	17.7×10^3

5.4.3 General discussion of the visibilities

Before actually comparing the synthetic to the measured visibility curves, a few more general conclusions shall be discussed which can be drawn from the overall shape of the measured curves themselves. The most intriguing fact is that although the baseline lengths for the 2005-06-24 and 2006-05-18 measurements are almost equal (43.9 m and 43.5 m, respectively) the respective visibility amplitudes are clearly distinct, even when considering the depicted 3σ errors (see Fig. 5.7). The respective projected angles (141° and 48°) differ by approximately 90° . This is a clear indication for a non-rotationally symmetric intensity distribution, i.e., the mid-infrared emission is dominated by a flattened structure, e.g., a disk. This interpretation of the visibility curves is consistent with the disk-only scenario proposed by the statistical analysis of the SED fitting.

To give an estimate of the size of the source, a Gaussian intensity profile² was fitted to the visibility amplitudes at 8, 10.5 and 13 μm (see Fig. 5.13, fit at $\lambda=10.5 \mu\text{m}$). The corresponding full width at half maximum were determined as 33, 38 and 40 mas (corresponding to 69, 80 and 84 AU, if a distance of 2.1 kpc is assumed), respectively. Note, though, that since obviously a Gaussian profile is a bad fit to the data, these numbers should be rather regarded as rough estimates.

For instance, if one assumes an extended source of 8-13 μm radiation, such as a halo or hot dust in an ultra-compact HII region, one would expect to measure rather small visibility amplitudes. These sources typically have sizes larger than 5×10^{15} cm (half-intensity radius, (Churchwell et al. 1990), corresponding to ≈ 160 mas at 2.1 kpc), which would imply much lower visibilities at these baselines due to over-resolving the target (the respective FWHM in Fig. 5.13 would be narrower by approximately a factor of four to five).

This is in accordance with the results found in the previous section, namely that the most probable solution for the SED fitting is an evolved, disk-only system without a dust envelope. The argumentation holds as well for every source of N-band emission being much larger than the scales found above. It applies, for example, also to a system consisting only of a central star plus flared circumstellar disk, seen edge-on. There, the direct view onto the hot inner rim of the disk is blocked, giving rise to more diluted emission on larger scales. Given the assumption that the projected intensity distribution of the KWO is not rotationally

² $\exp\left(-\frac{\pi^2}{4\ln(2)}\frac{FWHM}{u}\right)$ ($FWHM$ [rad], $u = \frac{\lambda}{B}$)

symmetric, which excludes a face-on disk, one would expect some intermediate inclination angle. Indeed, the ten best-fitting models are inclined by 57 to 81° , for which the resulting configuration still allows a direct line of sight to parts of the central disk edges (see Fig. 5.6).

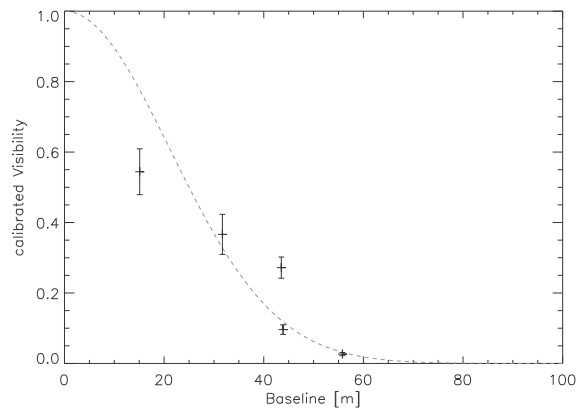


Figure 5.13: Fit of a 1D Gaussian intensity distribution to the visibility amplitudes at $10.5 \mu\text{m}$.

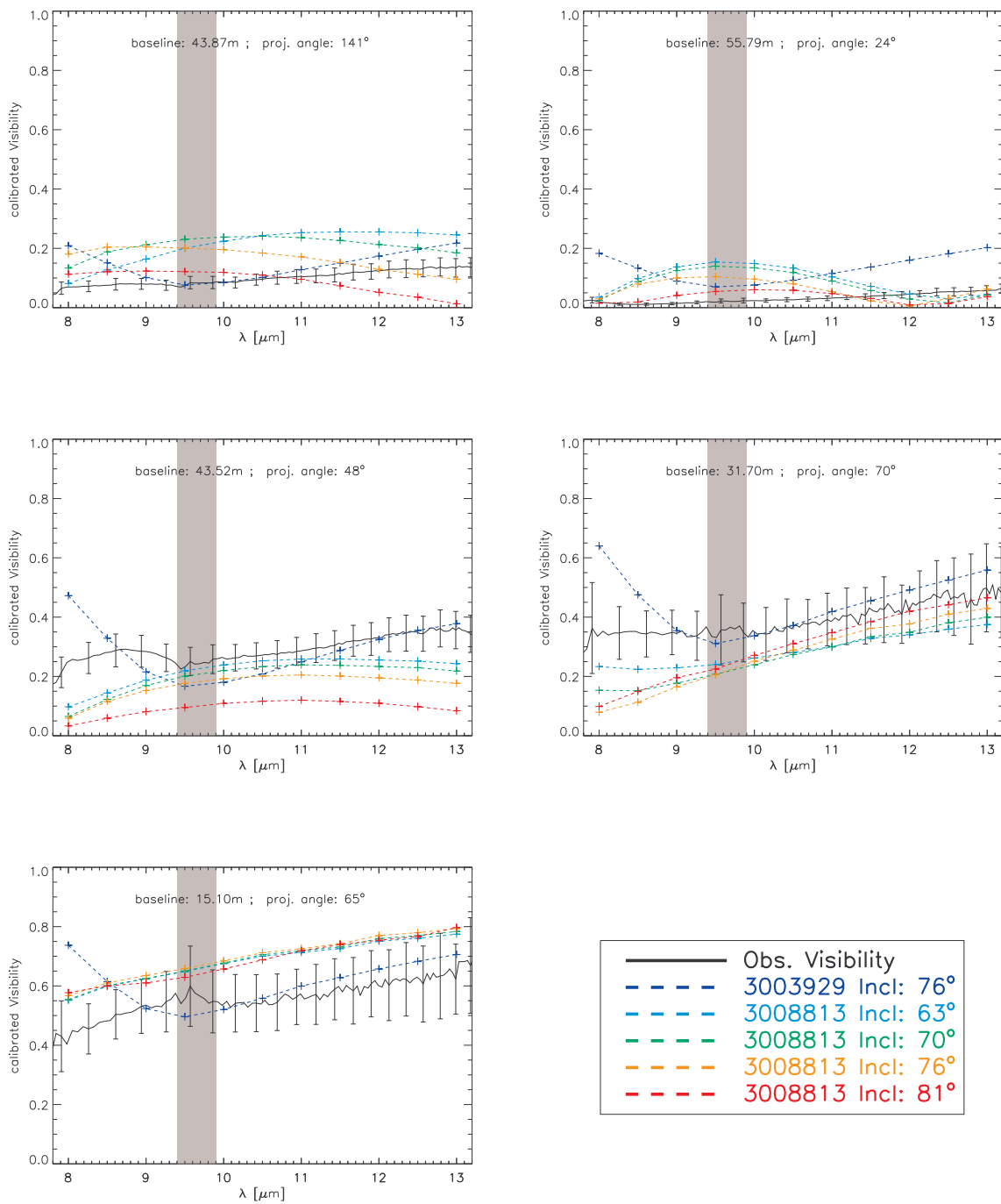


Figure 5.14: Comparison of the observed and synthetic visibilities; each figure represents one baseline configuration. The error bars are 3σ .

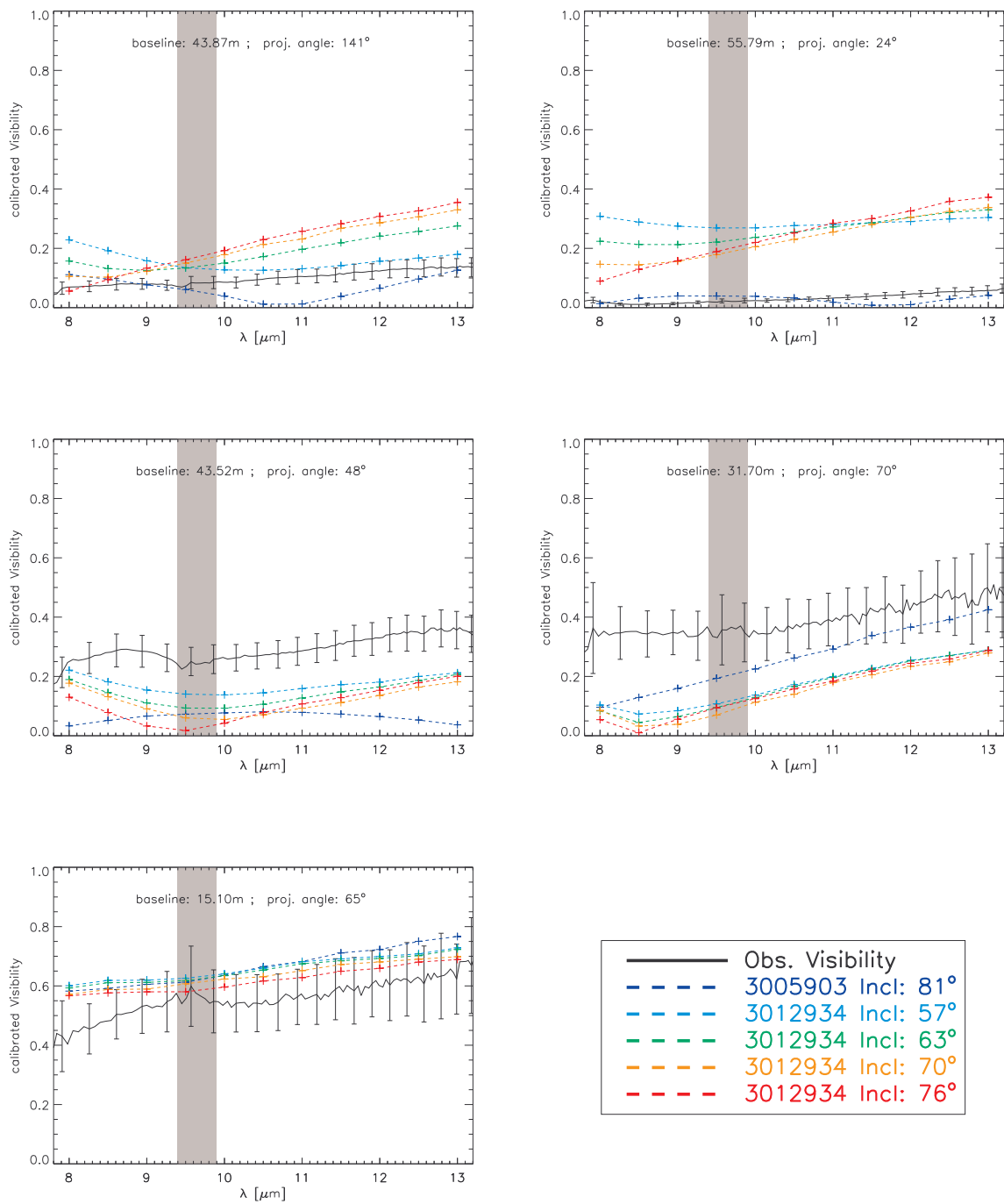


Figure 5.15: Comparison of the observed and synthetic visibilities; each figure represents one baseline configuration. The error bars are 3σ .

5.4.4 Comparison between modeled and measured visibility curves

Here, the modeled synthetic visibility curves and the measured ones are compared (see Figs. 5.14 and 5.15). Apparently, there is quite a discrepancy between the synthetic and the measured spectrally dispersed visibility curves. Nevertheless, there are clear differences in the qualitative shape of the modeled visibility curves, which enable us to exclude some of the models which otherwise fit the SED of the KWO almost equally well. Hence, this approach offers the ability to reduce the ambiguities arising from SED-only fitting.

The difference between measurement and model can have several origins. First, the flux measurements used with the Online SED model fitter were incomplete. Lacking submm/mm data, it is impossible to constrain the flux from the cold dust in the outer parts of the disk. This relates directly to the ambiguity in the results of the Online SED model fitter (see Fig. 5.5: The fitted SEDs differ considerably in this wavelength region). In addition, the modeling still suffers from many imperfections. For example, the model used here does not account for a puffed-up inner rim (Natta et al. 2001; Dullemond et al. 2001), yet most of the flux in the N-band stems from regions of the disk which would be affected in dimension and shape if this were implemented. A change of the geometric shape of this region will affect the shape of the synthetic visibility curves. The dust model used by the RT simulation code is also not well adapted to this disk-only situation, since it assumes a dust composition that resembles the typical composition of the halo, not including bigger dust particles which are likely present in an evolved disk. Additionally, a bigger variety of dust particles will lead to a smoothing of the dust destruction zone. Smaller dust grains in this region reach their evaporation temperature at larger distances from the central object than bigger ones. Hence, the inner radius of the disk as a function of height correlates with the size of the dust grain constituents, leading to a more curved, rather than flat, hot inner rim (Tannirkulam et al. 2007; Isella & Natta 2005).

Proper error handling is difficult to achieve when comparing the synthetic curves with the measurements. A conventional approach would be a global χ^2 measure, including deviations on all 5 baselines. Many models fit all the measurements except the 55.8 m baseline, where they fail to reproduce the rather low visibility amplitude. A conventional χ^2 measure, on the other hand, would overweight these measurements due to their small absolute errors. Yet, the relative error of all measurements is almost constant. Hence, instead of the absolute error, the square of the relative error is used as a weight in the error analysis. As a result, each curve is almost equally significant. In order to justify this *ansatz*, the same analysis was applied excluding the 55.8 m baseline. The two ways of handling the error deliver the same results, while they deviate partially when including all measurements in the standard deviation estimation. In this case, the absolute error weighted result was biased towards the 55.8 m baseline. Hence, the square of the relative error is used as the weight for comparing the measurements to the model. The results of this analysis are summarized in table 5.4. For a better comparison, the inclination angle and the χ^2 obtained from the SED fit are specified for each model in the first two columns. In column 4, the position angles (see section 5.3.2) best-fitting the data and in column 5 the respective estimates of the deviation between the synthetic models and the data are given.

The best agreement between model and data is obtained with model 3003929, the deviation estimate being almost a factor of two smaller than the next best one. It is interesting to note, that model 3003929 is not the best SED fit, although the respective values of the standard deviation of the SED fit for model 3003929 and the best fit are comparable. Model 3005903

and the four different variations of model 3012934 agree least with the data. Hence, they are excluded from the further discussion. Note that the four realizations of model 3008813 differ mainly in the inclination angle. The comparison between these four models and the data shows a trend toward smaller inclination angles. Yet, due to the small differences between the four realizations, the ones with inclination angles of 63° , 70° and 76° can be considered to agree equally well with the data. A comprehensive overview of the parameters determining model 3003929 (as well as the other models) can be found in Table 5.5.

Table 5.4: Standard deviations of the SED fits and estimates of the deviation between modeled and measured visibility curves.

Grid model number	Inclin. angle [°]	SED Fit χ^2	Pos. angle [°]	Visibility χ^2
3003929	76	141	16	73
3005903	81	189	167	248
3008813	63	190	176	125
	70	153	173	145
	76	123	171	155
	81	151	171	210
3012934	57	194	84	260
	63	199	89	284
	70	189	92	317
	76	188	92	338

Although model 3003929 agrees best with the data, there are obvious deviations between the synthetic and the measured visibility curves. To begin with, the synthetic visibility amplitude for the 55.8 m baseline is higher than the measured one. A possible reason for this was given above: this deviation might be systematic. There is good agreement for the other baselines, despite some qualitative discrepancies. Model 3003929 shows increased visibility amplitudes for the 8 to $9\ \mu\text{m}$ regime. The source of this behavior is probably directly related to how the RT code handles the inner rim. This rather narrow, hot region, from which emission in this wavelength regime emanates, is not as resolved in comparison to the other models due to the small inner disk radius of 3003929. This leads to higher visibility amplitudes. If one assumes that, in reality, a puffed-up inner rim exists, the spatial region of the disk emitting in the spectral range between 8 and $9\ \mu\text{m}$ might be considerably more extended, leading to the lower visibility amplitudes seen in the measurements.

Note that the total extinction given in table 5.5 is the sum of the interstellar and intrinsic extinction. The intrinsic extinction for disk-like structures is given for the direct line of sight; hence, it depends considerably on the inclination and flaring of the disk. If the total and interstellar extinction are equal on the other hand, this indicates a direct line of sight to the central stellar source.

Robitaille et al. (2006) state that the disk structure is given by:

$$\rho(\varpi, z) = \rho_0 \left[1 - \sqrt{\frac{R_*}{\varpi}} \right] \left(\frac{R_*}{\varpi} \right)^\alpha \exp \left(-\frac{1}{2} \left[\frac{z}{h} \right]^2 \right)$$

where $h \propto \varpi^\beta$ and $\alpha = \beta + 1$.

5.5 Conclusions

In this chapter, VLTI observations of the Kleinmann - Wright object with baselines ranging between 15 m and 56 m were presented. The target has been resolved for all baselines, with average visibility amplitudes between 0.01 and 0.69. In order to analyze the interferometric data, SED fitting was performed using the web tool of [Robitaille et al. \(2007\)](#). The resulting information, together with a Monte Carlo radiative transfer simulation code developed by [Whitney et al. \(2003a\)](#), was then used to create synthetic visibility curves. These were compared to the measured visibilities, which allows us to substantially narrow down the range of suitable solutions obtained by mere SED fitting.

While massive YSOs are usually thought to be associated with a significant circumstellar envelope which often dominates their infrared appearance, KWO does not show indications for a strong envelope component, and hence is probably more advanced in its evolution towards the main sequence. This is in accordance with [Porter et al. \(1998\)](#), who proposed that the classification as an embedded MYSO might be misleading, since it could be behind M17 SW but not actually embedded in it. The silicate absorption feature is missing in all visibility curves. This indicates that the silicate absorption feature, which is clearly visible in the total flux spectrum, is mainly due to foreground structures not associated with the KWO. In this geometry the correlated and uncorrelated fluxes are equally affected; hence, the visibilities do not show any pronounced silicate features. In addition, the statistical interpretation of the SED fitting also indicates the absence of a dusty envelope. The visibility curves in general can only be interpreted using an intensity distribution deviating from spherical symmetry, which hints at a circumstellar - disk scenario. Finally, evidence was given for a flared disk, inclined at 76° and with a mass of $\approx 0.1 M_\odot$ and an inner rim radius of 26 AU. This disk reproduces the combination of SED fitting and interferometric data best. To obtain better constraints for the dimensions of the disk and the amount of circumstellar material in general, high - resolution submm / mm data will be needed.

Chapter 6

AFGL 2136

High spatial resolution observations and grain growth in the vicinity

6.1 Introduction to AFGL 2136

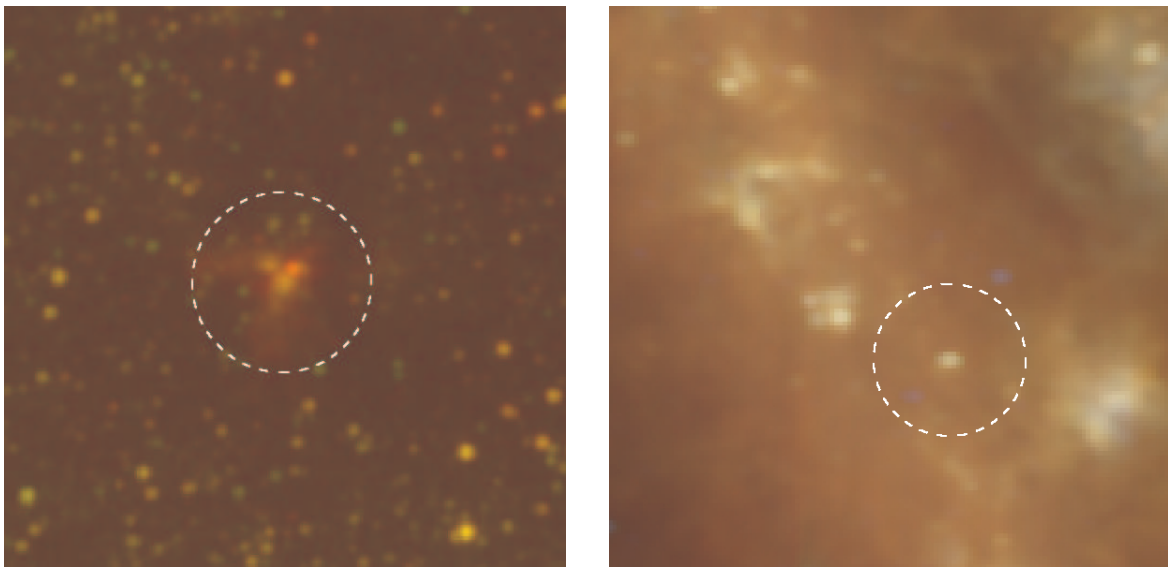


Figure 6.1: RGB composite images of AFGL 2136. The left figure is composed from logarithmically scaled 2MASS data (blue J - band, green H - band, red K - band), the right figure from logarithmically scaled IRAS data (blue $25\ \mu\text{m}$, green $60\ \mu\text{m}$, red $100\ \mu\text{m}$). The central object in the white dashed circle is at the position of the Juggler nebula of which AFGL 2136 is a component.

Due to its inherent infrared brightness, AFGL 2136 has a rich history of observations in the archives. [Minchin et al. \(1991\)](#) discussed the existence of a circumstellar disk with a position angle of 45° based on near-infrared imaging polarimetry. [Kastner et al. \(1991, 1992\)](#) determined a kinematic distance of about 2 kpc to 2.4 kpc, depending on the galactic rotation model adopted. Accordingly, they derive a total luminosity of $5 \times 10^4 L_\odot$. In a follow-up investigation, [Kastner et al. \(1994\)](#) used radio observations to identify a massive bipolar

molecular outflow at a position angle of 135° , thereby supporting the disk scenario. They determine the outflow to be inclined with respect to the line of sight by $\gtrsim 60^\circ$, leading them to the conclusion that the disc should be very thick or highly flared. Analyzing VLTI ISAAC and ISO SWS spectra, [Dartois et al. \(2002\)](#) concluded that AFGL 2136 is a quite evolved source and speculated upon grain growth. These results have recently been confirmed by JHK-band high-resolution imaging polarimetry ([Murakawa et al. 2008](#)) and MIR aperture masking interferometry ([Monnier et al. 2009](#)). Yet, while [Murakawa et al. \(2008\)](#) adopt an inclination angle towards the line of sight of $\approx 70^\circ$, [Monnier et al. \(2009\)](#) find that the axis ratio of a fitted two dimensional gaussian is close to one, which is indicative of a lower inclination angle. Finally, [de Wit et al. \(2011\)](#) try to simultaneously fit the SED and MIR interferometric data.

6.2 Observations and data reduction

6.2.1 Interferometric observations

MIDI correlated fluxes

The interferometric data were obtained with the MIDI instrument installed at the VLTI ([Leinert et al. 2003](#)) in the N-Band (8-13 μm). All the data presented were obtained using the UT telescopes. The interferometric data from [de Wit et al. \(2011\)](#), obtained from the ESO data archive, was added. Table 6.1 lists the observations, dates, times and telescopes used, as well as the associated baseline lengths and orientations. The observations were conducted following the procedure described in [Leinert et al. \(2004\)](#). MIDI was set to work in HighSens-mode. A prism, with a spectral resolution of $R \approx 30$, was used as the dispersing element.

The data reduction procedure employed in the standard package MIA+EWS (V1.6, see <http://www.mpia-hd.mpg.de/MIDI/> or [Jaffe \(2004\)](#)) is not suitable in the case presented here due to photometric variations during the night. This is in accordance with the findings from chapter 5. Thus, the same customized data reduction procedure used for the KWO was applied here.

The correlated fluxes of the science target were calibrated using the data of all suitable calibrator stars of the respective night of observation. Then, these calibrated correlated fluxes were averaged. Fig. 6.2 shows the averaged, calibrated correlated fluxes (depicted errors are 3σ). As described above, data from [de Wit et al. \(2011\)](#) was included, which is depicted in Fig. 6.2 with a red line. To be consistent with the rest of the data, the corresponding raw source and calibrator data were obtained from the ESO data archive and re-processed as above. They agree very well with the rest of the data, as one would expect considering the similarity of the baseline configuration.

MIDI visibility curves

In order to determine the spectrally dispersed visibility curves, one has to divide the averaged calibrated correlated fluxes by the averaged calibrated uncorrelated flux (e.g. the spectrum, see section 6.2.2). The calibrated dispersed visibilities appear in Fig. 6.3. The depicted errors represent 3σ . All of the visibility amplitudes are well below 0.1. Visibilities close to zero are commonly interpreted as the target being over-resolved at these spatial frequencies.

Table 6.1: List of observed objects. All objects other than the AFGL 2136 are calibrator stars. The objects marked with an asterisk are included in the subsequent analysis. See text for details. The third column, labeled BL, lists the projected baseline in meters, the fourth column the projected angles (PA) EON. The last column gives the VLTI telescopes forming the baseline.

Object	Date and Time	BL [m]	PA [°] E of N	UTs
HD 107446	2005-06-24T03:09:09	61.51	167.2	3-4
AFGL 2136*	2005-06-24T03:49:35	61.32	-73.0	3-4
HD 168415*	2005-06-24T04:22:42	62.34	108.6	3-4
HD 169916	2005-06-24T07:04:18	56.89	127.4	3-4
HD 169916	2005-06-24T07:59:14	52.06	138.1	3-4
HD 169916	2005-06-24T08:48:54	47.75	150.3	3-4
HD 177716	2005-06-24T09:59:36	47.07	160.2	3-4
HD 107446	2005-06-25T23:12:59	47.17	35.1	1-2
HD 169916*	2005-06-26T00:49:52	55.84	-6.5	1-2
HD 107446*	2005-06-26T01:44:57	38.57	57.5	1-2
HD 169916*	2005-06-26T02:29:52	55.88	8.0	1-2
AFGL 2136*	2005-06-26T03:02:08	53.51	14.0	1-2
HD 145544*	2005-06-26T03:58:14	43.41	44.6	1-2
HD 95272	2006-05-18T00:36:17	46.63	43.4	2-3
HD 169916*	2006-05-18T04:07:17	43.99	10.4	2-3
HD 101666	2006-05-18T05:41:02	26.03	58.0	2-3
HD 120404*	2006-05-18T06:42:24	28.96	100.1	2-3
HD 120404	2006-05-18T07:36:18	25.98	114.7	2-3
AFGL 2136*	2006-05-18T08:44:31	46.42	45.9	2-3
HD 168415	2006-05-18T09:27:57	44.99	47.8	2-3
HD 169916*	2006-05-18T10:28:38	40.01	52.2	2-3
de Wit et al. (2011)				
HD 151249*	2008-06-23T07:07:31	29.28	85.0	3-4
AFGL 2136*	2008-06-23T08:04:35	42.58	47.4	3-4
HD 175775*	2008-06-23T08:22:27	41.92	50.1	3-4

This is confirmed by the data from [Monnier et al. \(2009\)](#), which show a significant drop of the visibility amplitudes at lower spatial frequencies. Although Monnier's data were taken only at a single wavelength ($10.7 \mu\text{m}$), one can expect a similar behavior of the visibility amplitudes as a function of spatial frequency at similar wavelengths in general. Yet, since the measured visibility amplitudes do significantly differ from 0, this still restricts the possible range of models (see Fig. 6.26).

[de Wit et al. \(2011\)](#) report a steep rise of the visibility amplitude towards the blue edge of the dispersed visibility curve, which they interpret as proof for a compact source. Only a modest rise is observed after applying the customized data reduction procedure to their raw data. The red line in Fig. 6.3 represents the re-calibrated data from [de Wit et al. \(2011\)](#). This difference can be explained by the custom data calibration procedure, which treats the photometric calibration slightly different than EWS. This results in a clearly higher total flux at $8 \mu\text{m}$ compared to [de Wit et al. \(2011\)](#). For example, they use a flux at $8 \mu\text{m}$ of only

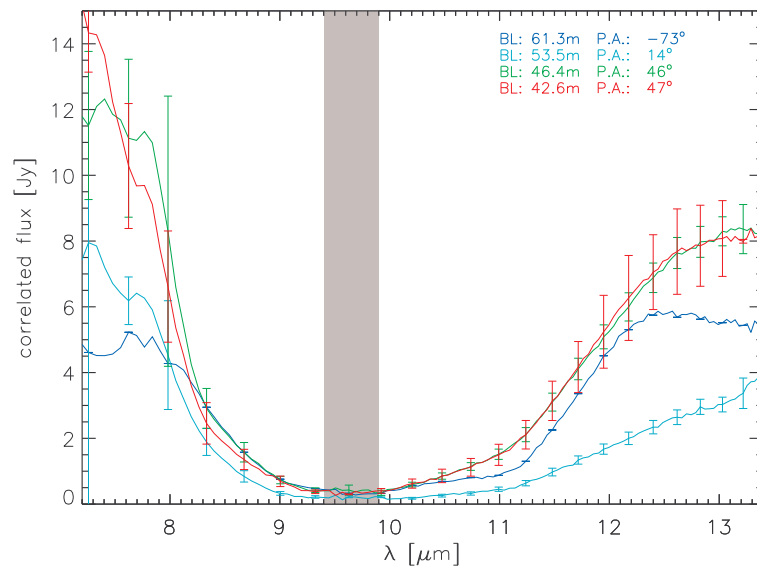


Figure 6.2: The measured correlated fluxes. The depicted error bars represent 3σ . The vertical gray bar denotes the ozone absorption feature, where terrestrial observations are unreliable. The red line shows the data from [de Wit et al. \(2011\)](#).

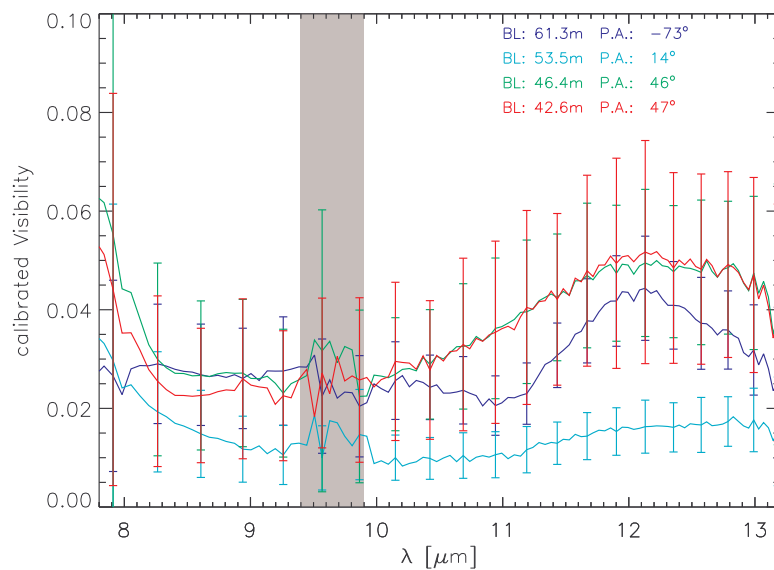


Figure 6.3: Calibrated visibility curves.

122 Jy. This discrepancy is consistent over all MIDI measurements (see Fig. 6.6). Hence, the visibilities for the de Wit data set are lower, given a rather similar level of correlated flux in both data reductions.

MIDI differential phases

In addition to the correlated fluxes, the differential phase data was extracted for each night of observation. Although in principle the calibration of differential phases should be straightforward, there are several effects which might influence the differential phase significantly, yet are difficult to assess (Millour et al. 2008), e.g. the water vapour content in the VLTI delay lines. The behavior of the differential phase data of the calibrators, which were used for calibrating the visibility amplitudes, was compared for each night of observation. Only small deviations were found from the expected zero mean in all cases ($\lesssim 10^\circ$). Therefore, the uncalibrated differential phases were used. Figure 6.4 shows the uncalibrated differential phases for each night of observation.

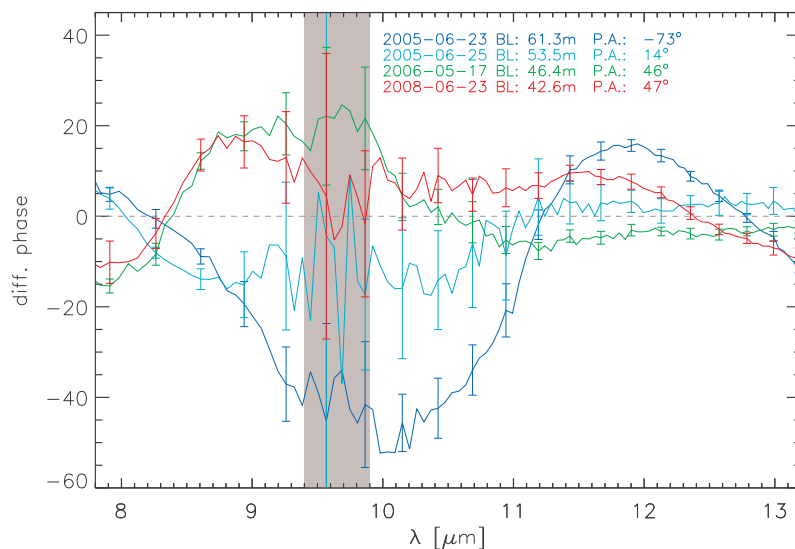


Figure 6.4: Uncalibrated differential phases for AFGL 2136. The depicted errors represent 3σ

Data from the Keck segment tilting experiment

To further increase the (u, v) -plane coverage, data recorded during the Keck segment tilting experiment was obtained from J. Monnier (Monnier et al. 2009). These data were taken in a filter centered at $10.7 \mu\text{m}$ ($9.92 \mu\text{m} - 11.47 \mu\text{m}$) in a field of view of $3''$. In order not to confuse the later analysis of these data, the (u, v) -plane is averaged in the radial direction using 0.25 m baseline length bins. Fig. 6.5 depicts the re-binned data.

Fig. 6.5 shows the re-binned data. Note that the plot depicts the Visibility amplitude as a function of spatial frequency, while the position angle associated with each data point has been taken into account for the model fitting. Thus, the marginal spread of the data for a certain spatial frequency is an indication for an object which only slightly deviates from circular symmetry.

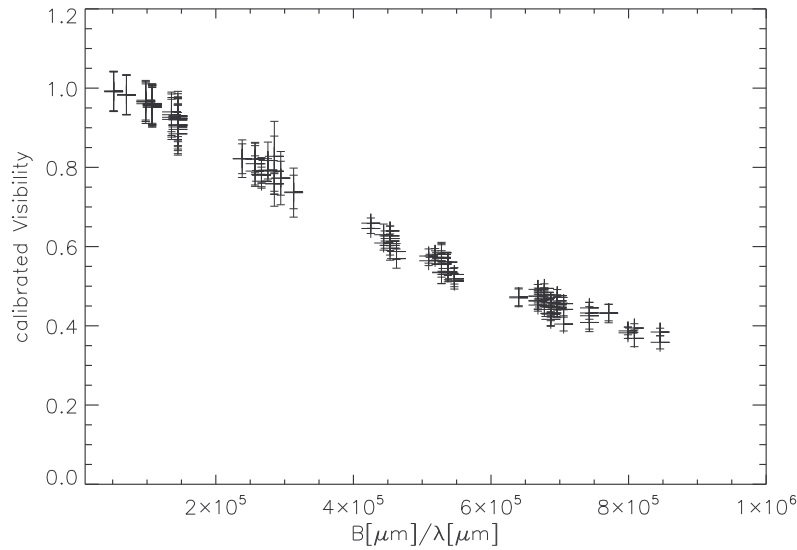


Figure 6.5: Re-binned (visibility vs. spatial frequency) data from the Keck segment tilting experiment (Monnier et al. 2009).

6.2.2 Spectra and SED compilation

MIDI spectra

The uncorrelated (i.e., total) fluxes were extracted from the MIDI data. These data were again averaged over the set of suitable calibrators per night of observation. There is a wealth of spectroscopic and N-band SED observations of AFGL 2136 available in the archives. All this information is included for deducing the average uncorrelated flux of AFGL 2136 (i.e. the spectrum).

The mean spectra obtained with MIDI for each night of observation agree well with the other observations (see Fig. 6.6). Therefore, it was decided to use the mean of the four MIDI spectra for further analysis. The respective mean spectrum is depicted as a dashed red line in Fig. 6.6.

SED compilation

The multi-wavelength spectral energy distribution (SED) comprises a wealth of information for the analysis of MYSOs. In order to analyze the interferometric data, Monte Carlo radiative transfer (MCRT) simulations are used based on SED fitting. For objects as complex as MYSOs, well-sampled data from the near infrared to radio wavelengths are required to properly constrain the SED. The SED used for the subsequent analysis is summarized in table 6.2. This SED consists mostly of archival data, unless stated otherwise. Data from the Two Micron All Sky Survey (Skrutskie et al. 2006) was included, as well as fully-processed ISO SWS and LWS data (Sloan et al. 2003 and Lloyd et al. 2003, respectively) and sub-mm/mm data collected in Mueller et al. (2002). Figure 6.7 depicts the compiled SED.

For comparison, there is MSX (Egan et al. 2003), AKARI IRC (Ishihara et al. 2010), IRAS (Helou & Walker 1988), SCUBA (Di Francesco et al. 2008) and 87 GHz data from van der Tak et al. (2000) in the plot. The 87 GHz data is not included in the subsequent SED fitting procedure, since the Online SED model fitter does not provide flux at this wavelength. All

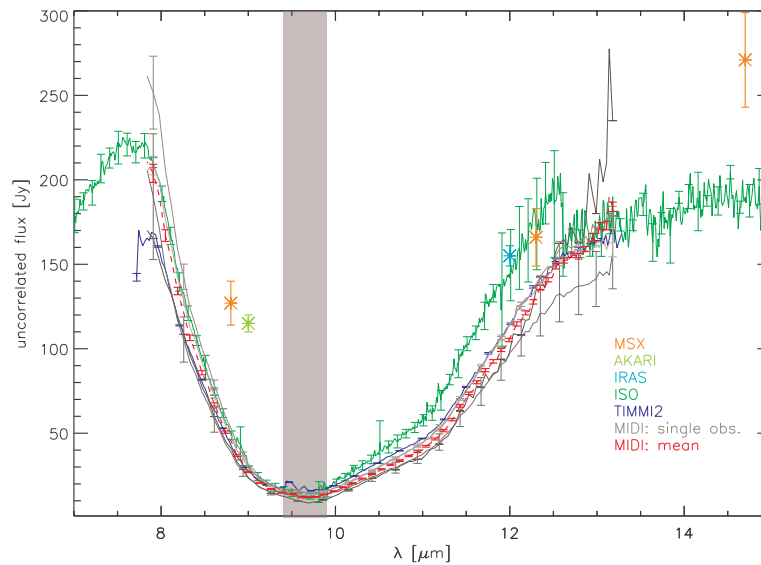


Figure 6.6: N-band spectra of AFGL 2136. For comparison, spectra from ISO SWS and TIMMI2 are presented as well as data from MSX, AKARI IRC and IRAS. The photometric means of the 4 nights of observations with MIDI are overplotted in gray continuous lines, while the mean of all nights is shown as a dashed red line.

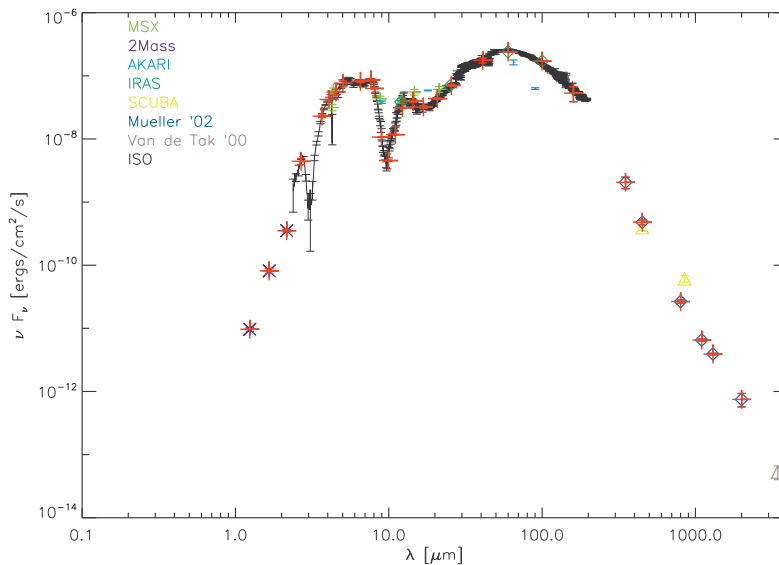


Figure 6.7: Compiled SED for AFGL 2136. The red crosses denote the SED data points used in the analysis. For a full description, see text.

the data are in good agreement with each other. The SED was compiled for further analysis in such a way as to (a) have a good and (on a logarithmic wavelength scale) equally spaced coverage of the whole wavelength range from the near-infrared to the millimeter and (b) to avoid or not to overemphasize absorption features. This is especially important for features which the SED fitter cannot reproduce, e.g. the water ice absorption feature at $3.08 \mu\text{m}$

(Kastner & Weintraub 1996). It applies as well to the silicate absorption features at $10\ \mu\text{m}$ and $18\ \mu\text{m}$ ¹. Section 6.4 presents an attempt to fit the silicate absorption features. The results differ significantly from the dust composition used in the *Online SED model fitter*, which supports the assumption to not over-emphasize these spectral ranges.

Table 6.2: Flux densities of AFGL 2136

wavelength [μm]	F_ν [Jy]	σ_{F_ν} [Jy]	aperture arcsec	data source
1.24	0.004	0.002	2	2Mass
1.66	0.04	0.01	2	2Mass
2.16	0.5	0.1	2	2Mass
2.68	4	0.48	20	ISO SWS
3.67	28	1.5	20	ISO SWS
4.07	57	5	20	ISO SWS
4.53	84	9	20	ISO SWS
5.03	130	11	20	ISO SWS
6.54	178	8	20	ISO SWS
7.65	220	7	20	ISO SWS
8.06	179	6	1.2	MIDI
8.95	33	1	1.2	MIDI
9.95	15.5	0.5	1.2	MIDI
11.05	44	1	1.2	MIDI
12.27	130	2	1.2	MIDI
14.36	190	8	25	ISO SWS
16.81	179	9	25	ISO SWS
20.74	301	8	25	ISO SWS
25.58	600	16	25	ISO SWS
41.03	2400	210	35	ISO SWS
60	4810	50	35	ISO LWS
100	5700	200	35	ISO LWS
160	2800	300	35	Mueller et al. (2002)
350	240	50	30	Mueller et al. (2002)
450	72	6	19	Mueller et al. (2002)
800	7.1	0.4	17	Mueller et al. (2002)
1100	2.4	0.1	19	Mueller et al. (2002)
1300	1.7	0.5	19	Mueller et al. (2002)
2000	0.5	0.12	19	Mueller et al. (2002)

¹The *Online SED model fitter* uses a fixed ISM dust composition (Robitaille et al. 2006). Extensive coagulation or ice features are not taken into account. A change in the dust composition would change the appearance of these features (private communication with T. Robitaille), see also section 6.4

6.3 SED fitting and statistical interpretation

6.3.1 SED fitting

The analysis of spectrally dispersed visibility curves is far from trivial. One can find analytical solutions for simple geometrical models of the intensity distribution (see subsection 6.5.1). They serve as a tool to assess the general properties of the targets intensity distribution. Nevertheless, these models usually oversimplify the complex shapes expected in MYSOs.

For this reason, a method similar to that presented in chapter 5 is applied by first fitting the compiled SED (see table 6.2) to pre-calculated models using the *Online SED model fitter*² (Robitaille et al. 2007).

The sets of parameters which describe the respective models are then used as input for a Monte Carlo radiative transfer model. The resulting model images are finally Fourier-transformed in order to produce synthetic visibility curves which can be compared to the measurements (Linz et al. 2009, see section 6.5.2).

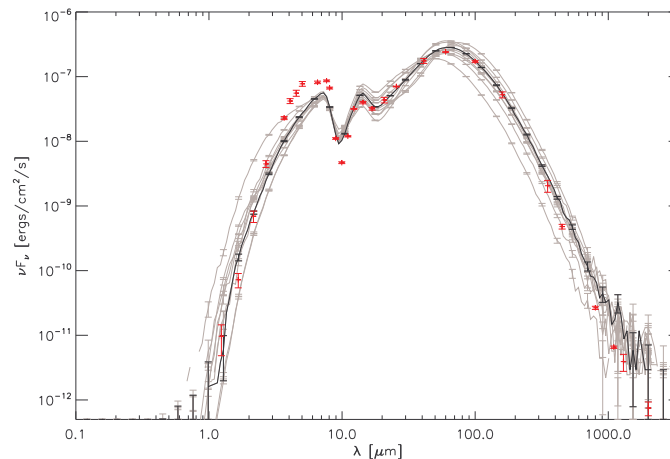


Figure 6.8: Best fit SEDs, obtained with the *Online SED model fitter*. The black solid line corresponds to the best fitting model, while the gray lines represent the 9 next best fits (based on the achieved χ^2). The red crosses represent the data indicate for the SED fitting.

In order to meaningfully constrain the range of probable solutions of the SED fitting, it is essential to fix the distance and the expected interstellar extinction towards the science target. A value of 1.5 mag is adopted as a lower limit for the visual interstellar extinction as expected for an object at a distance larger than 2 kpc. An arbitrary upper limit of 20 was set for the interstellar extinction. This is validated by the subsequent analysis.

Note the plotted histograms for each of the free parameters. There is no significant over-density in the histogram at the larger interstellar extinctions. Kastner et al. (1992) determined the kinematic distance of AFGL 2136 as either 2 kpc or 2.4 kpc, depending on the model of galactic rotation used. This result was substantiated by Wu et al. (2006), who find $d=2.3$ kpc. Accordingly, a distance range of $d=2.0$ kpc - 2.6 is adopted. Note that, concerning

²<http://caravan.astro.wisc.edu/protostars/index.php>

the fitting procedure, the distance and the interstellar extinction are treated as free parameters (within the limits). The 10 best fitting models and their respective model parameters are appear in table 6.3.

The models fit the data well in general. There are 2 main discrepancies. The models do not reproduce the deep silicate absorption feature at $10\ \mu\text{m}$. In subsection 6.4 a fit to the depth and shape of the silicate feature is presented using a power law distribution of dust grains of various sizes. This differs significantly from the dust composition used in the *Online SED model fitter*. Second, the models cannot reproduce the strong near-infrared excess at $3\text{-}8\ \mu\text{m}$. This can partially be explained as well by a grain model differing from that used in the *Online SED model fitter*, e.g. in chemical and size composition and optical properties. A simple explanation could also be an additional warm compact structure. The current version of the *Online SED model fitter* still has several shortcomings, i.e. it lacks a proper implementation of a puffed-up inner rim. Note as well that the sampling of the *Online SED model fitter* parameter space is sparse in the case of these very massive young stellar objects.

de Wit et al. (2011) use the *Online SED model fitter* as well for fitting their compiled SED of AFGL 2136. Unfortunately, they do not present any visualization of the fit. They claim that the models #3005338 and #3012893 do fit their SED best. This cannot be confirmed when comparing these models to the SED compiled for this work. A fit to both models at several different inclination angles was attempted, assuming boundary conditions for the distance and interstellar extinction as explained above. Since the resulting fits were less accurate than the results from the *Online SED model fitter* in conjunction with the newly compiled SED presented in this work (see table 6.2), these two particular models were not used in the subsequent analysis.

6.3.2 Object models from the SED Fitting

The 10 best fitting models (for details see table 6.3) obtained from the *Online SED model fitter* represent a good sample of the distribution of fitting models as discussed in section 6.3.3 below. Note that the χ^2 of the 10th best fitting model is more than a factor of two bigger than the χ^2 of the best fitting model. This shows that the SED fitting problem is well defined in the case of AFGL 2136.

The central stellar object is in all cases quite massive ($17\text{-}31\ M_{\odot}$), the best fitting model with model number 3005939 having an intermediate mass of $22\ M_{\odot}$. Many models have a star with large radius and a low surface temperature. This is in accordance with Hosokawa & Omukai (2009) and Hosokawa et al. (2010), who suggest a cool, bloated central object during certain stages of the evolution of MYSOs. Such a scenario was also the most likely solution for explaining the measured properties of M8E-IR in Linz et al. (2009). de Wit et al. (2011) suggest this scenario in particular for AFGL 2136, although they argue that the fit of the blue wing of the N-band spectrum then is correspondingly poorer. This cannot be confirmed. In fact the three best-fitting models point to a large central object. Three of the presented best-fitting models have smaller radii and higher temperatures. Kastner et al. (1992) suggest a temperature of the central star of $7000\text{-}15000\ \text{K}$. However, this was just based on the integrated IR luminosity in combination with a $2.2\ \mu\text{m}$ flux and the assumption of blackbody emission. The total luminosity for the models is in the range of $4\text{-}7 \times 10^4\ L_{\odot}$, which agrees well with previous work (Kastner et al. 1992, 1994)

All models require a prominent circumstellar dusty envelope. The inner radius is for all best fitting models situated very close to the dust sublimation radius, defined by the the dust

sublimation temperature of ≈ 1600 K. This corresponds to a few tens of AU, according to the RT models, or around 10 mas, assuming a distance of 2.3 kpc. Thus, the inner disk rim is unresolved even by the longest baseline measurements presented here. The envelope extends to several thousand AU. [Monnier et al. \(2009\)](#) introduce a halo component to fit their zero spatial frequency visibility which could be identified with this envelope.

There are two classes of models fitting the SED (see section 6.3.3 below): three that include a disk, and those that do not. Among the ten best-fitting models, four possess a disk. In these cases, the inner disk radius is, as for the envelope, close to the dust sublimation radius. The outer radius of these disks on the other hand, is rather small, only a few tens AU (10 - 23 mas at 2.3 kpc), which is less than the spatial frequencies resolved by the longest baseline (36 mas at $10.7 \mu\text{m}$). Section 6.5.3 discusses such a narrow disk or ring-like feature further.

Note that the total extinction given in table 6.3 is the sum of the interstellar and intrinsic extinction. The intrinsic extinction is given for the direct line of sight. [Robitaille et al. \(2006\)](#) state that the disk structure is given by ($h \propto \varpi^\beta$ and $\alpha = \beta + 1$):

$$\rho(\varpi, z) = \rho_0 \left[1 - \sqrt{\frac{R_*}{\varpi}} \right] \left(\frac{R_*}{\varpi} \right)^\alpha \exp \left(-\frac{1}{2} \left[\frac{z}{h} \right]^2 \right)$$

Table 6.3: Summary of model parameters.

	3005939	3003850	3011688	3006592	3015716	3007251	3010326	3005234	3019121	3003763
incl angle[°]	18	18	18	18	18	18	18	18	18	18
SED fitting χ^2	2939	3946	4348	4491	4553	4564	4673	5611	5765	5933
distance [pc]	2089	2455	1995	2089	1995	2570	2089	2570	2089	2570
A_V (total)	319	548	231	194	402	670	625	472	148	137
A_V (interstellar)	1.5	2.4	13	20	1.5	2.65	1.94	1.5	20	20
$R_{stellar}$ [R_\odot]	235	166	333	19	86	170	79	21	315	38
$M_{stellar}$ [M_\odot]	22	25	31	17	21	25	25	22	28	22
$T_{stellar}$ [K]	5400	7000	4200	18800	8600	7200	9900	20800	4300	14300
L_{total} [L_\odot]	41800	59400	31900	40500	36000	71200	53800	75800	31400	55600
envelope accr. rate [M_\odot /yr]	2.6×10^{-3}	4.8×10^{-3}	2.7×10^{-3}	1.9×10^{-3}	2.4×10^{-3}	6.9×10^{-3}	2.6×10^{-3}	2.7×10^{-3}	1.2×10^{-3}	1.9×10^{-3}
$R_{inner}^{envelope}$ [R_{sub}]	1.29	1.0	1.0	1.0	1.0	1.0	1.0	1.33	1.0	1.0
$R_{outer}^{envelope}$ [AU]	10000	10000	8900	10000	10000	10000	10000	10000	5000	10000
disk mass [M_\odot]	6×10^{-2}	1×10^{-2}	-	-	16×10^{-2}	-	-	33×10^{-2}	-	-
R_{inner}^{disk} [R_{sub}]	1.29	1	-	-	1	-	-	1.33	-	-
R_{inner}^{disk} [AU]	18	17	-	-	14	-	-	29	-	-
R_{outer}^{disk} [AU]	31	23	-	-	34	-	-	58	-	-
disk accr. rate [M_\odot /yr]	4×10^{-6}	2×10^{-6}	-	-	9×10^{-6}	-	-	30×10^{-6}	-	-

6.3.3 Statistical reduction of the parameter volume

SED fitting of YSOs and MYSOs is in general a degenerate problem (Men'shchikov & Henning 1997). To tackle this degeneracy and to explore the meaningful parameter space, a statistical approach is adopted by following Pinte et al. (2008). For this purpose, histograms were created for the different model parameters (accounting for the 1000 best-fitting models), with each count weighted by $1/\chi^2$. Note that no a priori assumptions were involved.

Over-densities in these histograms will then identify probable classes of models fitting the data. The respective widths of the over-densities are a means for assessing the range in which a certain parameter varies. In addition, if an over-density is found to occur at the edge of the total allowed parameter space, this indicates that the boundaries of the respective parameter are not properly chosen.

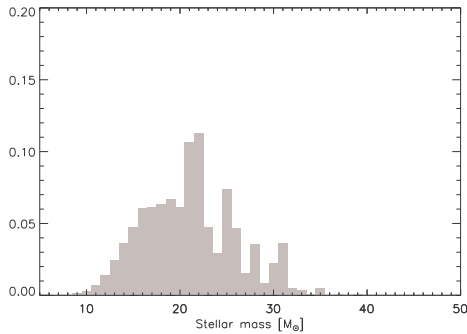


Figure 6.9: Distribution of the stellar mass. The ordinate gives the fractional occurrence of the values.

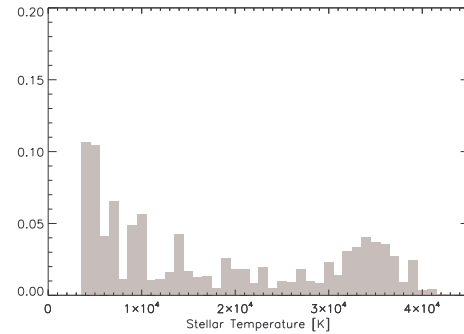


Figure 6.10: Distribution of the stellar temperature. The ordinate gives the fractional occurrence of the values.

The stellar properties

Figures 6.9 and 6.10 show the distribution of the fitted stellar masses and temperatures, respectively. The distribution of the mass peaks around $21/22 M_{\odot}$, although the peak is rather broad. The stellar temperature peaks at around 5000 K with a second concentration around 35000 K. This is agreement with previous findings. Based on comparing the $2.2 \mu\text{m}$ flux to blackbody radiation, Kastner et al. (1992) suggest a central object with a temperature in the range of 7000 K to 15000 K. This might be interpreted as the class of cool, bloated central objects in accordance with Hosokawa & Omukai (2009) and Hosokawa et al. (2010). Harvey et al. (2000) found 33000 K from theoretical predictions for zero-age main-sequence stars.

Disk and envelope

Figure 6.11 plots the histogram of fitted envelope accretion rates. The distribution peaks heavily at $10^{-3} \frac{M_{\odot}}{\text{yr}}$. Note that there is no solution which is solely composed of a central star and a surrounding circumstellar disk, since there is no model with no envelope accretion rate. Within the framework of the *SED online model fitter*, models with no envelope are parametrized by an envelope accretion rate of zero.

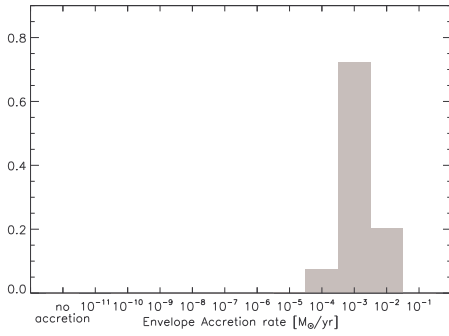


Figure 6.11: Distribution of the envelope accretion rate. The ordinate gives the fractional occurrence of the values.

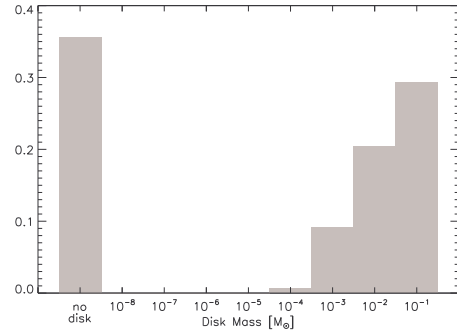


Figure 6.12: Distribution of the disk mass. The ordinate gives the fractional occurrence of the values.

Figure 6.12 shows the histogram of disk masses. There are two classes of solutions, those with no disk and those requiring heavy disks. For the second class (see Fig. 6.13), the inner rim is situated at the dust sublimation radius. By construction of the models (Robitaille et al. 2006), the inner rim of the envelope coincides with the disk’s inner rim. The dust sublimation radius corresponds on average to a distance from the central stellar object of 16 ± 3 AU or ≈ 8 mas at a distance of 2 kpc. This is well below the resolution of even the longest baseline data presented in this chapter. Note, though, that the dust sublimation radius in fact marks the hot inner rim of either the disk and/or the envelope. Thus, one would expect that the structures one can see in the N-band are slightly more extended, which nicely agrees with the findings from fitting the two centered Gaussian to the interferometric measurements (see section 6.5.1 below). Finally Fig. 6.14 shows that most of the solutions have an inclination of less than 40° , with a strong peak at an inclination less than 20° . This is in good agreement with the results of Monnier et al. (2009) and the results for the axis ratios of the simple geometric models, which can be interpreted as an inclined disk seen in projection (see section 6.5.3 below). An axis ratio close to one therefore can be interpreted as an seen object, seen face-on. More precisely, the average value of axis ratio of 1.06 corresponds to an inclination angle of about 20° . Note, though, that the model parameter grid of the *Online SED model fitter* is rather coarse.

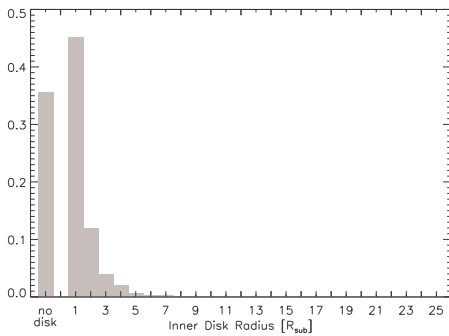


Figure 6.13: Distribution of the disk inner radius in units of the sublimation radius. The ordinate gives the fractional occurrence of the values.

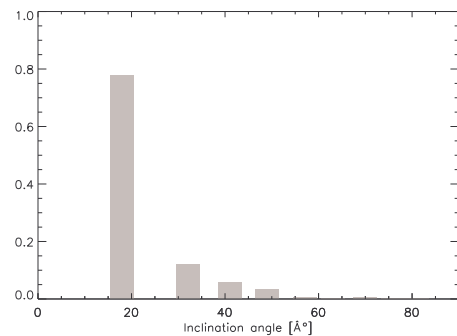


Figure 6.14: Distribution of the inclination angle. The ordinate gives the fractional occurrence of the values.

6.4 Dust growth in AFGL 2136

6.4.1 Fitting the silicate absorption features

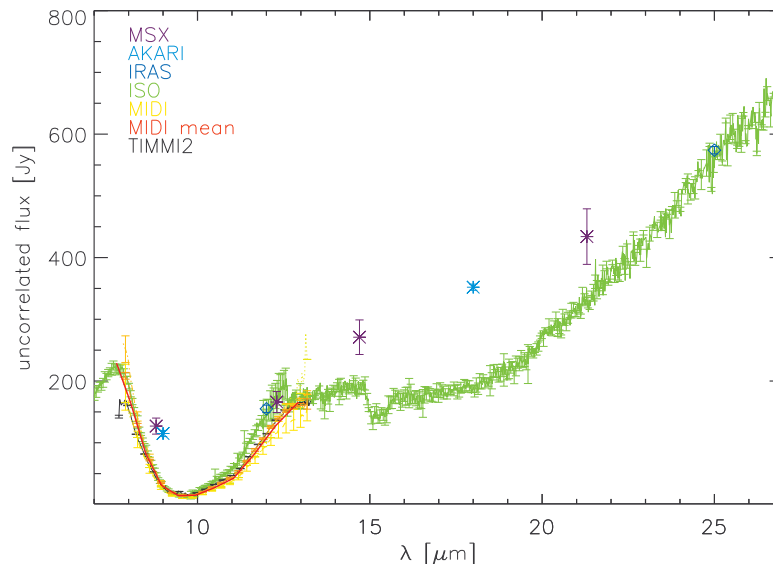


Figure 6.15: The spectrum of AFGL 2136 between $7 \mu\text{m}$ and $27 \mu\text{m}$.

In this section, a fit to the 10 and 18 micron silicate absorption feature is presented. To fit the data, a composition of dust grains of various radii was assumed.

The optical depth of the feature is calculated from the spectra presented in Fig. 6.15 assuming a flat continuum spectrum. Then, a power law size distribution of dust grains is generated, parametrized by a minimum grain size (a_{min}), a maximum grain size (a_{max}) and an exponent p . The tabulated optical properties for astronomical silicates of [Draine & Lee \(1984\)](#) are used to calculate opacities at nine tabulated wavelength in the N-band. Finally, the opacity curve is multiplied by the column density, which is considered to be constant with respect to wavelength (within the N-band), and which is an additional free parameter.

To assess the most probable grain composition, a grid search was conducted within a parameter volume ($a_{min} \in [1 \times 10^{-3} \mu\text{m}, 0.8 \mu\text{m}]$, $a_{max} \in [5 \times 10^{-2} \mu\text{m}, 8 \mu\text{m}]$, $p \in [-2, -7]$). The probability for each parameter combination is evaluated as $e^{-\chi^2}$. The maximum probability is normalized to one for better visualization. Finally, the set of parameters is determined for which the probability is maximal.

Since the model is highly non-linear, the approach of [Andrae \(2010\)](#) is applied in order to assess the parameter uncertainties. To identify the probable ranges of the parameters, the probabilities of models having a certain or a higher value are integrated, such that the integrated probability amounts to a fraction of the total integrated probability of 68.3%, 95.5% and 99.7% (1, 2 or 3σ , respectively).

To justify the somewhat arbitrary choice of a linear, flat continuum to calculate the optical depth of the silicate absorption feature, the results were compared to two additional, slightly different scenarios. The first scenario assumes the existence of a population of pristine dust

in the vicinity of the central object. This pristine dust population has approximately the composition of the interstellar medium, and can therefore be parametrized by a minimum grain radius of $0.005 \mu\text{m}$, a maximum grain radius of $0.25 \mu\text{m}$ and an exponent of the respective power law distribution of -3.5 (van Boekel et al. 2003). This dust population emits in the N-band. Thus the absorption due to the foreground dust has to be higher to reproduce the measured N-band spectra, and the optical depth increases accordingly. van Boekel et al. (2003) found that for such a dust population, there is a peak to continuum value (in N-band flux) of ≈ 1000 . The second scenario assumes an already processed dust population ($r_{min} = 2.5 \mu\text{m}$, $r_{max} = 3.5 \mu\text{m}$ and $p = -3.5$) in the vicinity of the central object. This dust population would also produce an emission feature, although with a greatly reduced peak to continuum value (in N-band flux) of ≈ 20 (van Boekel et al. 2003). The grid search was repeated for these two different scenarios. Then, the results were compared to the flat continuum scenario. Finally, a fit to the $18 \mu\text{m}$ silicate absorption feature is attempted in the same way as described above.

6.4.2 Grain growth in the circumstellar environment of AFGL 2136

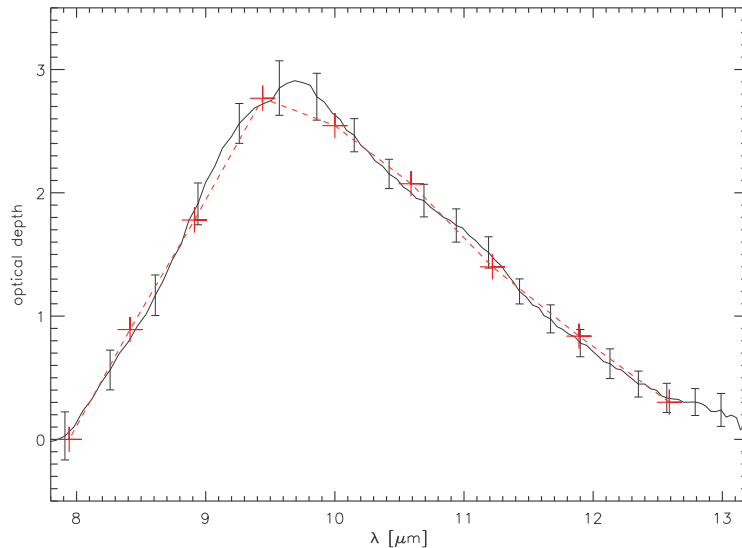


Figure 6.16: Fit of the $10 \mu\text{m}$ silicate absorption feature of AFGL 2136.

Figure 6.16 shows the best fit to the $10 \mu\text{m}$ silicate absorption feature of AFGL 2136. The best fit parameters are: $a_{min}=0.004 \mu\text{m}$, $a_{max}=2.6 \mu\text{m}$, $p = -3.3$ with an associated dust column density of 0.0015 g/cm^2 . Figures 6.17, 6.18 and 6.19 depict the respective probability planes for each pair of parameters, assuming a column density of 0.0015 g/cm^2 . As explained in section 6.4, the contour levels are calculated according to Andrae (2010). The red plane depicts all models for which the respective integrated probability over this subset is 68.3% of the entire integrated probability, which can be interpreted as a 1σ plane. The green plane depicts 95.5% of the entire integrated probability and the blue plane 99.7% (2σ and 3σ , respectively). The white cross shows the most probable set of parameters.

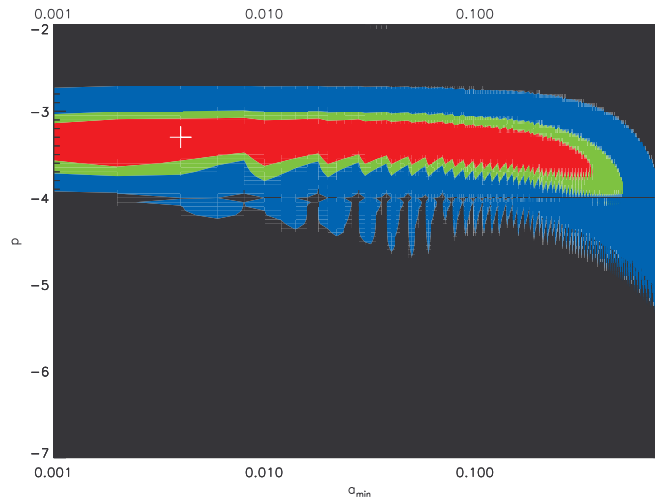


Figure 6.17: a_{min}/p probability plane.

The minimum radius of grains, a_{min} , is not well constrained. It does agree though with

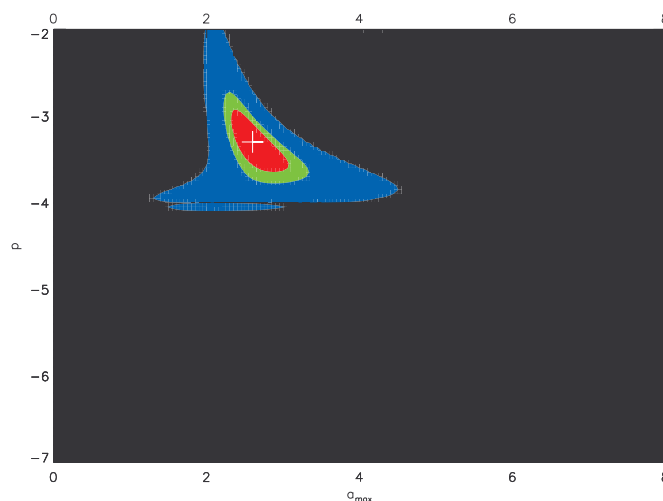


Figure 6.18: a_{max}/p probability plane.

small grain sizes found in the interstellar medium. On the other hand, grains larger than $2 \mu\text{m}$ (a_{max}) are needed to fit the data. This is in contrast to the interstellar medium, where commonly a maximum grain size $\lesssim 0.3 \mu\text{m}$ is assumed. In addition, the exponent of the fitted power law distribution of grains is in agreement with the common assumptions for the interstellar medium ($p = -3.5 \pm 0.3$). This leads us to the conclusion that grain growth has taken place around AFGL 2136.

The above results are based on the assumption of a flat continuum flux for calculating the optical depth. As explained in section 6.4, the grid search was applied again to the two other scenarios: a pristine and a processed dust population emitting in the N-band. Although details of the probability maps do change (the best fitting parameter set and the shape of the 1σ , 2σ and 3σ planes), the overall result is robust: The minimum grain size is not well constrained, but it agrees with findings for the interstellar medium. The exponent of the

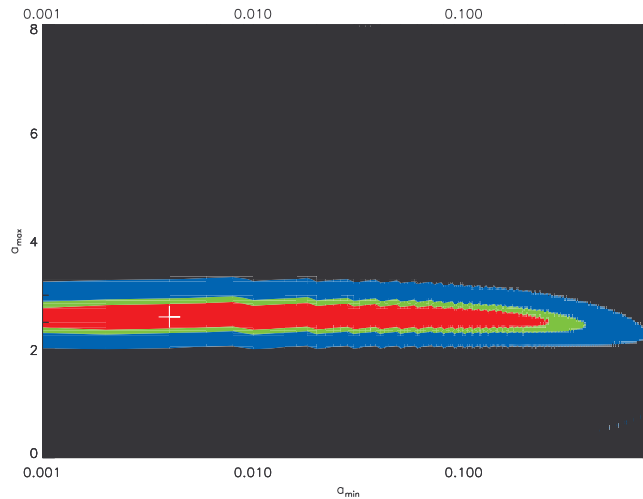


Figure 6.19: a_{min}/a_{max} probability plane.

power law distribution is again -3.5 , which agrees nicely with findings for the interstellar medium. But grains with sizes larger than $2 \mu\text{m}$ are essential for fitting the data in both of these alternate scenarios, which strengthens the claim of grain growth in the vicinity of AFGL 2136.

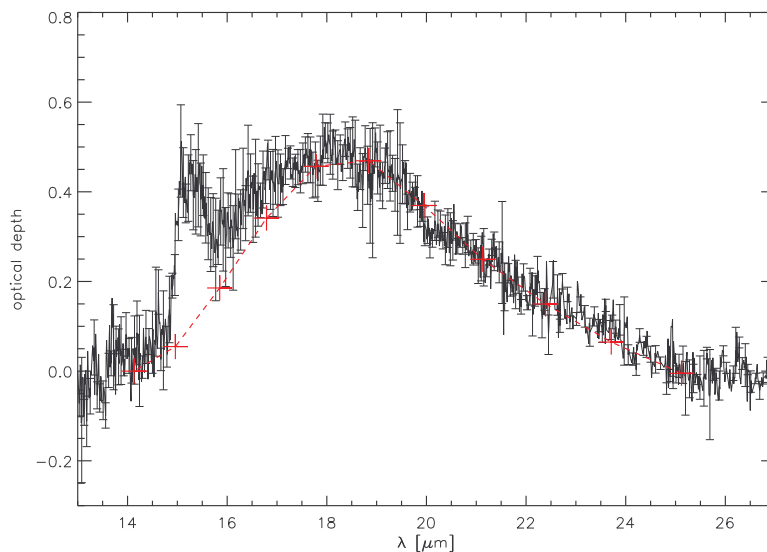
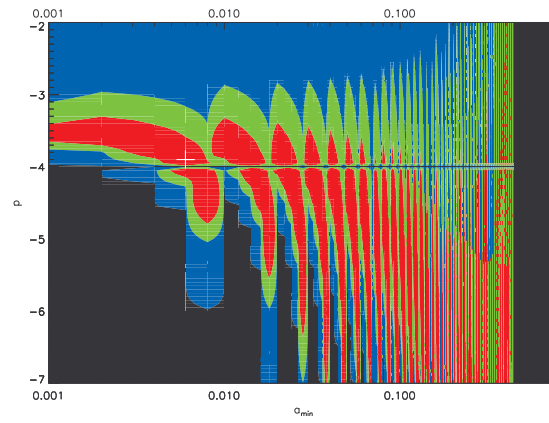
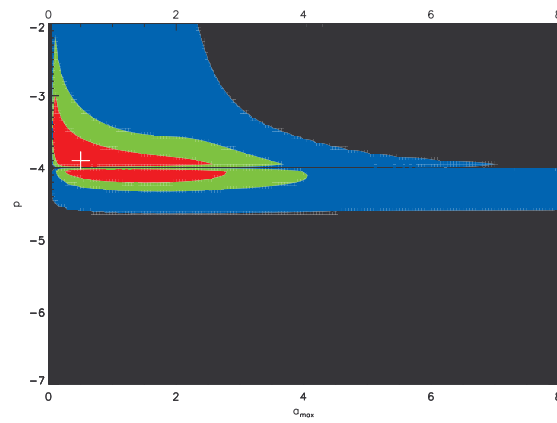
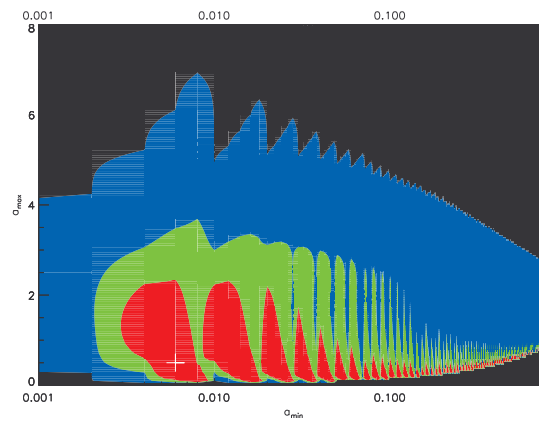


Figure 6.20: Fit of the $18 \mu\text{m}$ silicate absorption feature.

Figure 6.20 depicts the best fit of the $18 \mu\text{m}$ silicate absorption feature. The $18 \mu\text{m}$ silicate absorption feature is not as pronounced as the N-band absorption feature and the relative errors are larger, as well. In addition, one can identify a CO_2 ice bending mode absorption feature at $15 \mu\text{m}$ (Knez et al. 2005). These factors make an accurate fit of the $18 \mu\text{m}$ feature more difficult.

The best-fitting parameters are: $a_{min}=0.006 \mu\text{m}$, $a_{max}=0.5 \mu\text{m}$, $p=-3.9$ with an associated

dust column density of 0.0011 g/cm^2 . The column density is in good agreement with the results found by fitting the N-band absorption feature, although the other parameters are different. Note that none of the $18 \mu\text{m}$ fit parameters are as well constrained by referring to the respective probability planes (Fig. 6.21, 6.22 and 6.23). Note that the oscillations seen in Figs. 6.21 & 6.23 are probably caused by the numerical integration of the tabulated optical properties. In fact, a solution with a maximum grain size larger than 2 micron is still within the 1σ plane. Therefore, although the fitting of the $18 \mu\text{m}$ silicate absorption feature is not as conclusive as the fitting of the N-band feature, the indication of grain growth is consistent with both.

Figure 6.21: a_{min}/p probability plane.Figure 6.22: a_{max}/p probability plane.Figure 6.23: a_{min}/a_{max} probability plane.

6.5 Interpretation of the interferometric observations

6.5.1 Fitting simple geometric shapes

In order to assess the general properties of the intensity distribution of AFGL 2136, various analytic geometric models are fitted to the data from the Keck segment tilting experiment and the MIDI data at $10.7 \mu\text{m}$.

In a first attempt, a simple two dimensional Gaussian is fitted to the MIDI data only. This allows us to exploit the high spatial resolution information associated with the long baseline interferometric data. The spatial scales found from these fitted models will not give us representative spatial scales, since the fit does not include the short baseline data. Nevertheless, any asymmetries (and corresponding position angles) associated with these high spatial frequencies can be determined, independent of the Keck data, since for single morphological structures these are independent of the absolute measure on the spatial scale.

Then, a fit assuming a combination of a two dimensional Gaussian with a resolved (halo) component was attempted to recreate the results of [Monnier et al. \(2009\)](#). In addition, there is a fit of (1) a 2D-Gaussian + halo + a point source situated at the photo center, (2) a 2D-Gaussian + halo + a 2D-Gaussian (co-centered, but having a significantly lower FWHM) and finally (3) a 2D-Gaussian + halo + a co-centered ring-like structure. All of these structures are parametrized in real space with a spatial resolution of 5 mas. The size of the real space frames for the models is chosen large enough to achieve an adequate spatial frequency resolution in Fourier space. The real space frames are then Fourier transformed and the Fourier amplitudes corresponding to the data determined. The respective model parameters come from a χ^2 -minimization using a Levenberg-Markwardt algorithm in IDL (mpfit, [Markwardt 2009](#)).

6.5.2 Radiative transfer modeling and synthetic visibilities

The analysis of the observed spectrally dispersed visibilities is based on the models introduced by [Whitney et al. \(2003b\)](#). First, the SED (Fig 6.8) of AFGL 2136 is fitted in order to find a suitable set of parameters describing AFGL 2136 using the *Online SED model fitter*. MC RT simulations were conducted for the 5 best-fitting model configurations using the TTSRE code of [Whitney et al. \(2003a\)](#). The simulation was run each time using a total of 50 million test photons. Photons were tracked in a box of the 2800 AU by 2800 AU. This roughly corresponds to the expected field of view of MIDI ($1.4''$) at an assumed distance of about 2 kpc. The MCRT code was modified by defining 11 narrow filters centered at equally spaced wavelengths covering the N-band, see Fig. 6.24 for an impression of the best-fitting model.

The structure seen extends to about 1400 AU. The picture has been smoothed using a six pixel wide Gaussian kernel to reduce the graininess inherent to Monte Carlo Simulations. The hard edge in the upper right part is a result of the applied box. The structure would thus partially fill the field of view of MIDI.

Synthetic visibilities were calculated from the resulting model intensity distributions following the procedure described in chapter 5. These were then compared to the measured visibilities (see section 6.5.5) in order to further constrain the probable parameter volume found by the SED fitting. The position angle is determined by rotating the respective images and minimizing the deviation from the measured visibilities.

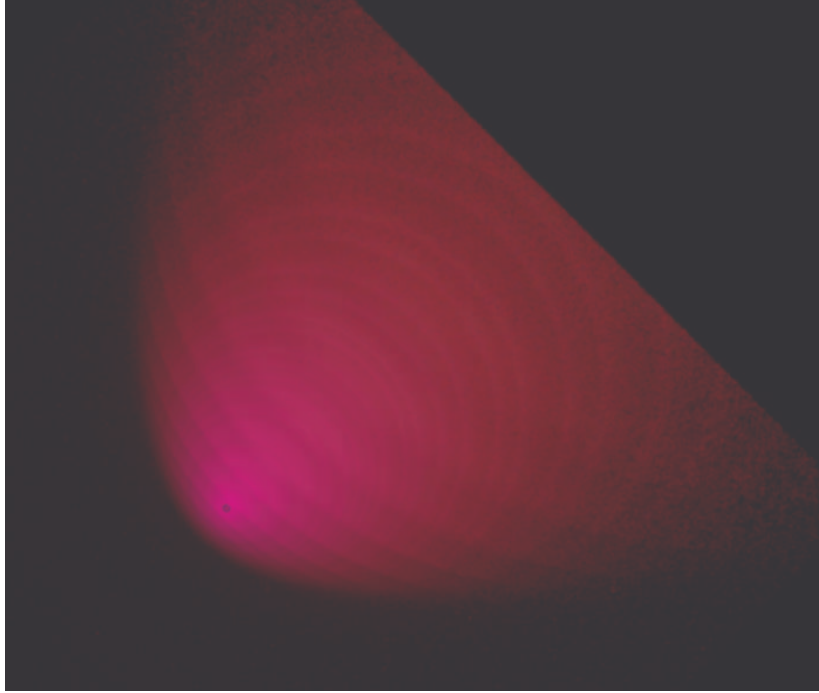


Figure 6.24: Synthetic RGB composite image for model 3005939 at a position angle of -45° EON. The $13\ \mu\text{m}$ bin is depicted in red, the $10\ \mu\text{m}$ bin in green and the $8\ \mu\text{m}$ bin in blue. See text for details.

6.5.3 Results from simple model fitting

The results for all the fits appear in table 6.4. The FWHM of the major axis increases slightly from 38 mas at $8\ \mu\text{m}$ to 55 mas at $13\ \mu\text{m}$. Note though, that this is not a significant spatial scale of the intensity distribution in the scope of a global solution, since this result neglects the Keck data. The axis ratio is 1.4 for wavelengths larger than $10\ \mu\text{m}$ and slightly larger (≈ 1.9) at shorter wavelengths. This is a clear sign of asymmetry at these large spatial frequencies. If interpreted as a sign of a cylindrically symmetric structure which is inclined with respect to the line of sight, one can determine an inclination angle of 45° (58° for $\lambda \leq 10\ \mu\text{m}$, respectively). This differs from the results found by Monnier et al. (2009), who found an axis ratio of only 1.06. Finally, a position angle of the major axis (east-of-north) of $42 \pm 6^\circ$ was found. This is in excellent agreement with previous findings (Kastner & Weintraub 1996; Murakawa et al. 2008; Monnier et al. 2009), if this asymmetry in the intensity distribution is interpreted as an inclined disk structure. Fig. 6.25 shows the reconstructed, normalized intensity distribution found for this fit. The white lines represent the baselines used for the MIDI measurements.

Monnier et al. (2009) fit a two dimensional Gaussian and a halo component to their $10.5\ \mu\text{m}$ Keck data. They explain the existence of the halo component by the fact that the field of view of an interferometer of a co-axial interferometer is in general rather limited. For comparison, their model was recreated. The results compare well. A slightly larger FWHM was found, but this can be explained by the fact that (u, v) -plane averaging was not applied as explained in Monnier et al. (2009). Yet, it is obvious (Fig. 6.26, solid line) that this model significantly underestimates the long baseline visibilities.

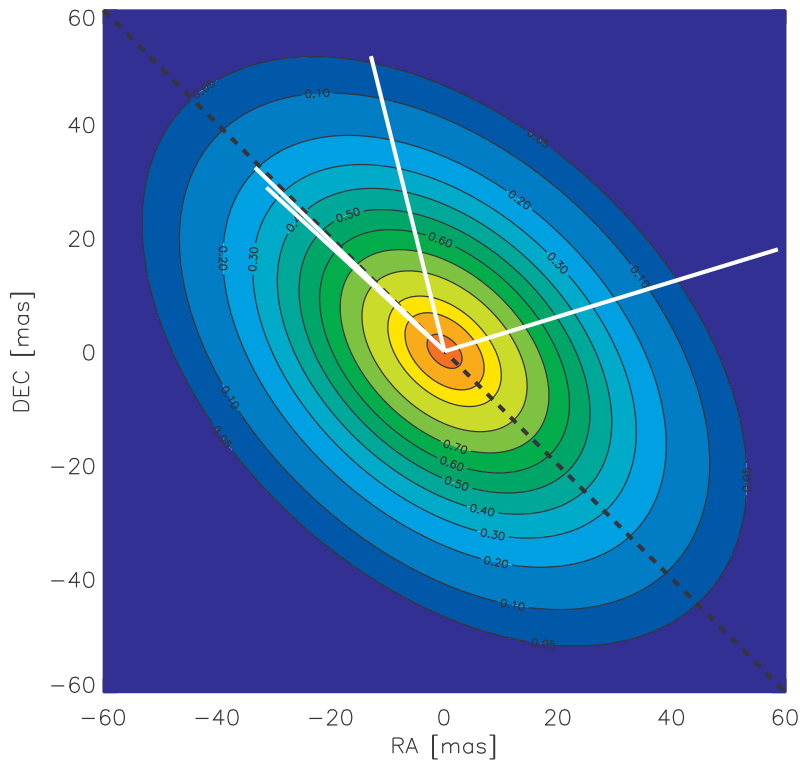


Figure 6.25: 2D-Gaussian normalized intensity distribution fitting the MIDI data. The respective baselines are depicted as white lines whose length corresponds to spatial frequency associated with the respective baseline length. The dashed black line shows the orientation of the major axis of the disk-feature.

Therefore, fits to the data were made using a selection of various combinations of simple shapes. Fig. 6.26 shows the resulting fits. Note that the drawn lines represent horizontal cuts through the (u, v) -plane. Since the curves are for visualization purposes only, the direction of the cut is somewhat arbitrary. Note though that the fitting was done using the full 2D (u, v) -coordinates. The resulting parameters can be found in table 6.4.

The easiest approach to fit the long baseline data is to add a point source which is centered on the Gaussian component. On the other hand, a point source obviously cannot reproduce the significant differences in visibility amplitude of the long baseline data. To solve this, there are two approaches. The first option comprises two centered Gaussian components. This approach can reproduce the long baseline visibility amplitudes (note again that the line only represents a cut through the (u, v) -plane). The parameters found show that the first component has a larger FWHM than in the other models, while the amount of halo flux is significantly reduced. The second, smaller component, on the other hand, would not be resolved by a 10 m aperture like the Keck telescope.

Finally, the data was fitted with a Gaussian component and an inclined ring. The Gaussian component has approximately the same properties as for models without the ring, which is expected, since this part of the model is mainly driven by the short baseline Keck data. Various ring configurations (with different inner radii and width) can reproduce the data.

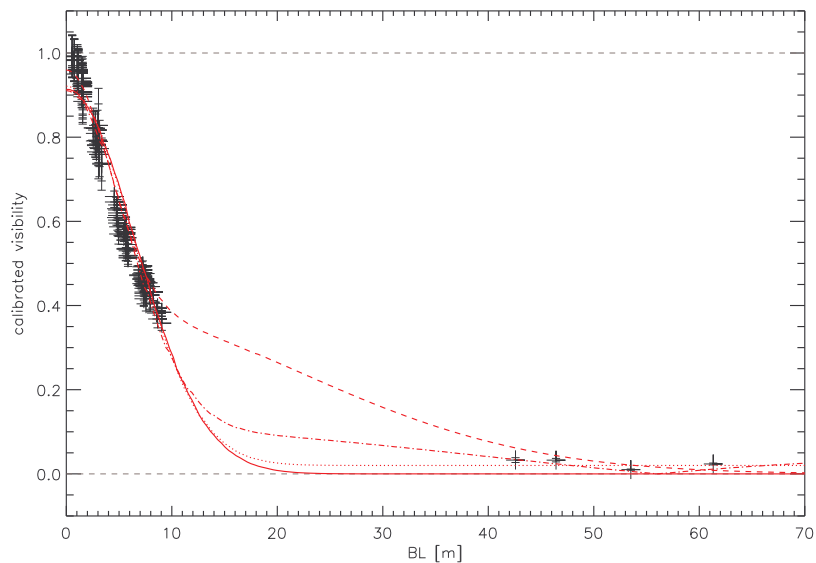


Figure 6.26: (u, v) - plane fits of simple analytic models. Solid line: Gaussian + halo; dotted line: Gaussian + halo + point source; dashed line: 2 Gaussian (differing in FWHM) + halo; dash-dotted line: Gaussian + halo + ring-like structure.

The inner radius and width of the ring mainly determine the zeros for the visibility as a function of baseline. Since the data is not decisive with respect to nulls of the visibility, the inner radius and width of the ring cannot unambiguously be determined. Nevertheless, a ring structure, which can be interpreted as a thin disk, comparable to what was found from the SED fitting (see section 6.3.2, the ring like structure can be identified with the disk) can reproduce the long baseline visibilities.

When comparing these different geometries for all the models, one can identify an extended component. The spatial dimension, as well as the axis ratio and PA are similar to the findings of Monnier et al. (2009). A second, much smaller component is required to reproduce the long baseline data. In addition, it becomes clear that future intermediate baseline data ($BL \approx 15$ - 35 m) will be necessary, since the models differ significantly at these spatial frequencies.

Table 6.4: Fitted parameters of the applied simple geometric models

parameter	value	1σ error
Gaussian + halo		
FWHM [mas]	130	2
axis ratio	1.05	0.01
position angle [$^{\circ}$ EON]	53	5
flux fraction halo		15%
flux fraction Gaussian		85%
Gaussian + point + halo		
FWHM [mas]	130	1
axis ratio	1.06	0.01
position angle [$^{\circ}$ EON]	48	4
flux fraction halo		14%
flux fraction point		2%
flux fraction Gaussian		84%
2 Gaussian + halo		
FWHM ₁ [mas]	218	6
axis ratio ₁	1.11	0.02
FWHM ₂ [mas]	42	1
axis ratio ₂	0.7	0.04
position angle [$^{\circ}$ EON]	41	3
flux fraction halo		7%
flux fraction Gaussian ₁		56%
flux fraction Gaussian ₂		37%
Gaussian + ring + halo		
FWHM [mas]	142	3
axis ratio	1.06	0.02
inner radius ring [mas]	10	1
width ring [mas]	9	1
position angle [$^{\circ}$ EON]	45	10
flux fraction halo		13
flux fraction Gaussian		80
flux fraction ring		7

6.5.4 Shift of the photo center

The wavelength-dependent differential phase data can present in certain cases an additional source of information on the geometry of the target. If the differential phase shows phase jumps of 180° , this is a strong signature for a zero of the visibility amplitude as a function of spatial frequency. It can also be used to discern the location of the companion in a binary system with respect to the primary and the brightness ratio of the two components (Ratzka et al. 2009).

In the case of AFGL 2136, the differential phase is significantly different from zero, but no phase jump of 180° can be observed. There are also no signs of binarity, neither in the Visibility curves nor in the differential phase data. There is a significant signal in the differential phase data for wavelength around $10 \mu\text{m}$, i.e. where the SED shows a deep absorption feature due to small silicates. Such differential phase signals were recently associated with deviations from point symmetry of the targets intensity distribution (Linz et al. 2008). To first order, the differential phase signal can be interpreted by a spatial shift of the photo center within the absorption feature with respect to the continuum photo center.

During the EWS data reduction process, the constant and linear terms of the retrieved phase information are set to zero (Ratzka et al. 2009). The linear term corresponds to a general spatial offset of the source from the expected origin. Therefore, the remaining differential phase signal can be attributed to an additional shift of the photo center. To estimate this photo center shift, the data was fitted by an appropriate function³ separately for each spectral channel of the MIDI data and \overrightarrow{BL} is the baseline vector.

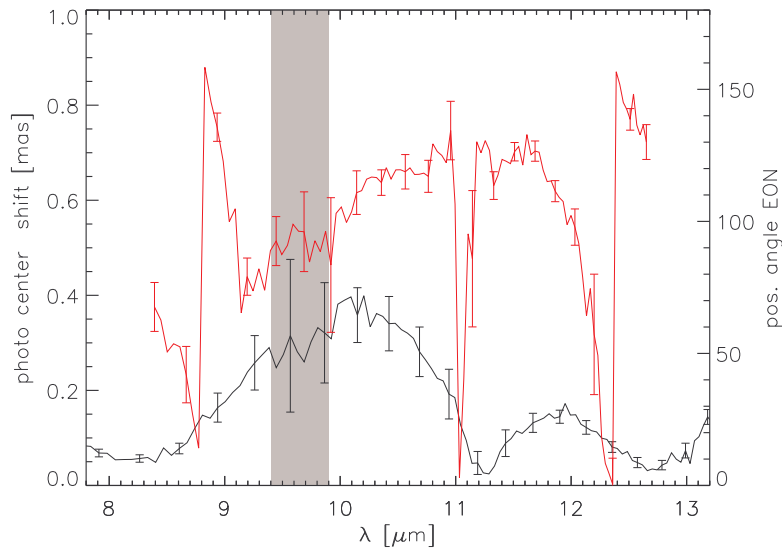


Figure 6.27: Photo center shift of AFGL 2136. The black line depicts the relative magnitude of the shift, while the red curve shows the position angle of the shift vector EON.

Fig. 6.27 shows the results of the fit. The depicted errors denote 3σ . There is a significant shift in the center of the N-band. The position angle of the supposed photo center shift is almost constant in the direction of 120°EON . Note, that this photo center shift denotes a

³ $\Phi(\lambda) = \frac{2\pi}{\lambda} \overrightarrow{BL} \circ \vec{\epsilon}$; where $\vec{\epsilon}$ is the photo center shift

relative shift of the photo center in the absorption feature with respect to the continuum. Thus, the maximum shift occurs in the center of the silicate absorption band at $\approx 10 \mu\text{m}$. Assuming a distance of AFGL 2136 of $\approx 2.3 \text{ kpc}$, the maximum shift of 0.38 mas relates to a shift of the photocenter by 0.87 AU .

One can tentatively identify the photo center shift as a shift in the direction of the illuminated outflow cavity in the dusty envelope of AFGL 2136. The opacity in the N-band changes significantly as a function of wavelength, mainly due to the silicate absorption band. The observed structures depend on the optical depth of the material along the line of sight. At the continuum edges of the silicate absorption band, photons from the innermost regions can penetrate the dusty envelope, while in the center of the absorption band only the outer structures will be visible. In the case of a structure like an elongated, illuminated inner cavity wall this will lead to a shift of the photo center if the line of sight partially penetrates the envelope. This effect also depends on the inclination of the MYSO towards the line of sight. In a face-on configuration, the intensity distribution will remain symmetric, thus, no photo center shift will occur.

Fig. 6.28 illustrates this concept. The single pictures were created by using the `ttsre` radiative transfer code (Whitney et al. 2003b). Note that the maximum intensity is different in each frame for a better illustration. This does not affect the general statement since the visibility amplitude and phase only depend on the normalized intensity distribution. Each picture was created in a narrow spectral band, centered at $\lambda=8 \mu\text{m}$, $\lambda=10 \mu\text{m}$, $\lambda=13 \mu\text{m}$ (left, central and right inset, respectively). The white arrows illustrate the approximate position of the photo center with respect to the central object. Note the significant shift of the photo center in the central inset. This is due to the increased extinction in the center of the $10 \mu\text{m}$ silicate absorption feature. In fact, the central object itself is hard to see in the central inset.

Note, that the spatial scales of the structures as depicted in Fig. 6.28 exceed several 100 AU . Thus, the depicted photo center shift (i.e. the white arrows in Fig. 6.28) is larger than the photo center shift as determined by the differential phase data. This is a further indication that the models used in the *Online SED model fitter* are not able to describe the AFGL 2136. Note, that the analysis of interferometric amplitude data (i.e. the Keck segment tilting experiment data and the MIDI dispersed Visibility curves) showed as well that the structures predicted by the *Online SED model fitter* models are too extended (see section 6.5.5).

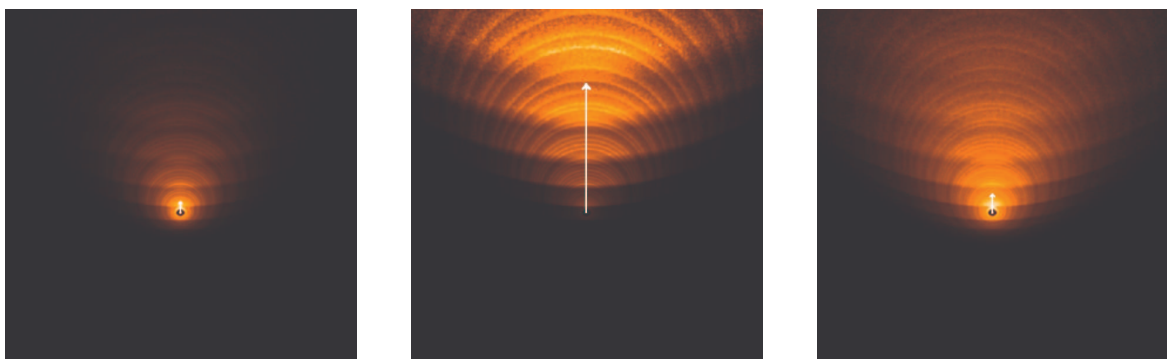


Figure 6.28: Concept of photo center shift. The pictures were created with `ttsre` code (Whitney et al. 2003b). They show the intensity distribution at $\lambda=8 \mu\text{m}$, $\lambda=10 \mu\text{m}$, $\lambda=13 \mu\text{m}$ (left, central and right inset, respectively). The white arrows illustrate the approximate position of the photo center with respect to the central object. Note that the photo center is significantly shifted in the central inset.

6.5.5 Comparison between modeled and measured visibility curves

When comparing the modeled synthetic visibility curves and the measured ones (see Fig. 6.30), the synthetic visibility curves can, in general, not reproduce the measurements. The visibility amplitudes of the models are significantly lower than the measurements. The most apparent structure in the N-band is the very extended illuminated inner cavity wall, which will give almost zero visibilities at the spatial frequencies associated with the baselines of the measurements presented in this chapter. The results are summarized in table 6.5. They are ordered by the χ^2 obtained from the SED fitting. The presented position angle is defined as described section 5.3.2: The modeled frames resulting from the MC RT code are oriented northwards, thus, the position angle remains as a free parameter. It is determined by minimizing the deviation between synthetic and measured visibility curve. Although there is only a very slight variation with position angle, the minimal χ^2 is attained for $\approx 45^\circ$ in all cases, which nicely agrees with the other results.

Table 6.5: χ^2 of the SED fits and χ^2 estimates of modeled visibility curves

Grid model number	SED Fit χ^2	Pos. angle [°]	Visibility χ^2
3005939	2939	44	1677
3003850	3946	43	1747
3011688	4348	47	1567
3006592	4491	44	1483
3015716	4553	45	1687

To further investigate the model predictions, they were compared to data of the Keck segment tilting experiment (see Fig. 6.29). The dashed lines are cuts through the (u, v) -plane in the direction of the largest spatial extension, and the solid lines are in the perpendicular direction.

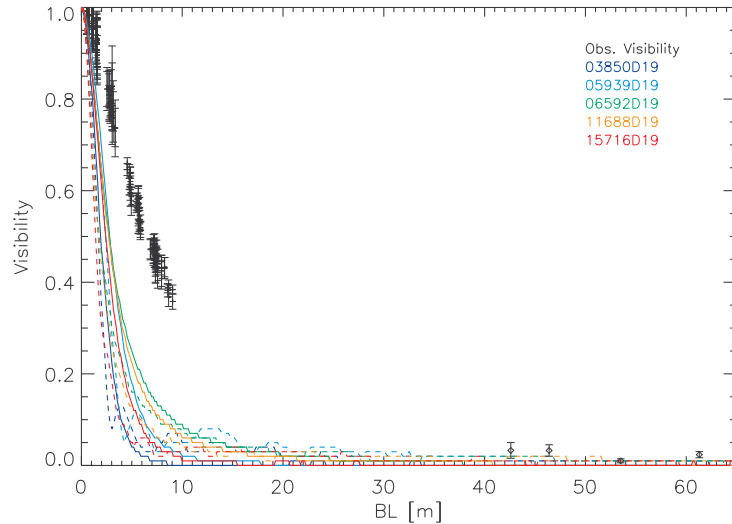


Figure 6.29: Comparison between the Keck segment tilting experiment data (black crosses), MIDI data (black diamonds) and the MC RT models (colored lines). See text for details.

Since the filter used for the Keck segment tilting experiment was rather broad, the respective spectral channels of the MC RT models are averaged, taking into account the respective filter transmission curve. Apparently, the structures predicted by the model are too large (i.e. the visibilities are too low) to reproduce the Keck data. Note that [Monnier et al. \(2009\)](#) claim a $3''$ field of view for the Keck segment tilting experiment, so one can exclude vignetting effects. The difference between measurement and model can have several origins, as explained in chapter 5. In fact, a compact warm structure, as suggested in section 6.4, would probably increase the correlated flux in the N-band significantly. An in depth investigation is not an option within this work, though, due to the complexity of the MC RT models.

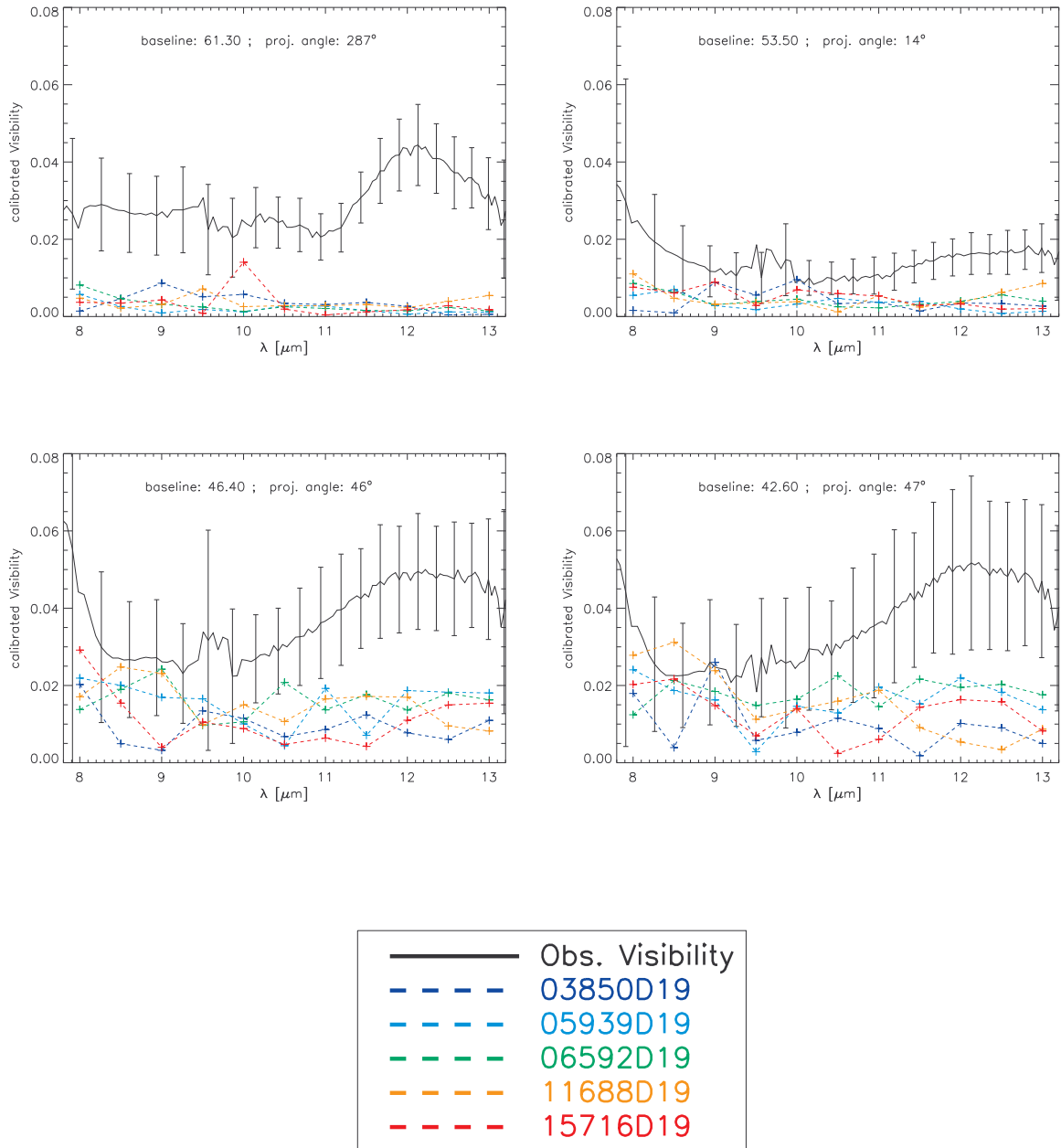


Figure 6.30: Comparison of the observed and synthetic visibilities; each figure represents one baseline configuration. The error bars are 3σ .

6.6 Conclusions

In this chapter, VLTI observations of AFGL 2136 are presented with baselines ranging between 42.6 m and 61.3 m. The target has been overresolved for all baselines, with average visibility amplitudes less than 0.05.

To investigate the nature of AFGL 2136, an SED fit was attempted using the web tool of [Robitaille et al. \(2007\)](#). The resulting information was analyzed in a statistical way to find suitable parameter ranges (see section 6.3). The SED fitting alone does not give a clear answer as to the nature of AFGL 2136. It is probably a heavily - embedded young stellar object with a mass of $15 M_{\odot}$ - $25 M_{\odot}$. The central star could either be cool and bloated, i.e. a scenario suggested by [Hosokawa & Omukai \(2009\)](#) for MYSOs, or more compact with a temperature of $T_{star} \gtrsim 30000$ K. Approximately half of the fitting models do possess a circumstellar disk. Finally, an inclination angle with respect to the line of sight is found, with angles less than 20° is most probable.

Then, various dust grain distributions were fitted to the $9.7 \mu\text{m}$ and $18 \mu\text{m}$ silicate absorption features. The exponent of the power law dust size distribution is comparable to findings of the ISM (-3.5). The minimum radius of the dust grains is not constrained, yet it is also comparable to the ISM ($\lesssim 0.5 \mu\text{m}$). More importantly, one needs a maximum grain size of $\approx 2 \mu\text{m}$ to fit the $10 \mu\text{m}$ absorption feature, while the $18 \mu\text{m}$ absorption feature is consistent with a maximum grain size of $\approx 2 \mu\text{m}$. This is interpreted as an indication that grain growth is taking place in the circumstellar environment of AFGL 2136.

Finally, an analysis of the MIDI data is presented. A fit of the MIDI dispersed visibility curves to an analytic two dimensional Gaussian yields an elongated structure parallel to a disk predicted in the literature ($\text{PA} = 42 \pm 6^{\circ}$). When combined with measurements from the Keck segment tilting experiment, it becomes obvious that 1) models more complex than simple two dimensional Gaussians are needed to fit both data sets and 2) that more interferometric data with baselines in the range of 15 m to 30 m will be necessary to distinguish between the various analytic models. Unfortunately, such an undertaking is still not possible due to the limited performance of the optical guiding on the VLTI auxiliary telescopes which otherwise could deliver such baseline measurements. The analysis of the differential phase data can tentatively be interpreted as a photo center shift perpendicular to the disk structure along the illuminated inner cavity wall of the dusty envelope. The MC RT models did not fit the data very well.

Chapter 7

Outlook

Optical interferometry is currently becoming a valuable tool for observational astronomy. It offers new and unique options for addressing several problems, since it increases significantly the attainable spatial resolution. Nevertheless, interferometry in the optical and infrared is a very young technique of observational astrophysics. Just with the availability of the most recent observatories, i.e. VLTI or the Keck Interferometer, interferometric techniques were applied to various fields of research on a broad variety of targets.

Interferometric observations still face several challenges during daily operations. The technical obstacles which need to be overcome to coherently combine light from several separate apertures are manifold. One of these obstacles is differential piston which can be introduced by, for example, the atmosphere or vibrations in the structure of the observatory and / or the instrument itself. In particular, sophisticated fringe tracking systems attempt to fix the temporal or spatial fringe motion. The efficiency of these systems will be increased; the longer a fringe stabilization can be achieved, the longer the signal can be integrated without suffering from degradations. Thus, fainter sources can be observed. Furthermore, metrology systems as planned for, for example, GRAVITY (see [Eisenhauer et al. \(2011\)](#) for a most recent review), will measure OPD variations along the optical path within the observatory. The information attained in this way will then serve as an additional input for the fringe tracking system. The atmospheric piston simulator presented in this work will allow on the other hand verification of the LINC-NIRVANA fringe tracking system under as realistic as possible conditions.

In upcoming years, the second generation interferometric VLTI instruments GRAVITY ([Eisenhauer et al. 2011](#)) and MATISSE ([Lopez et al. 2008](#)) will introduce many new applications of interferometry. GRAVITY will combine the light of four telescopes operating in the NIR. This allows for a quicker (u, v) -plane coverage. In addition, GRAVITY will introduce a new metrology concept which will allow to measure OPD variations along the light path with the telescope structure. MATISSE will for the first time combine light in the MIR (L, M, N and Q band, 3-25 μm) from up to four telescopes. This will enable us to also measure the closure phase in the MIR which is an important step toward model-unbiased image reconstruction. Both instruments will allow to observe fainter objects as well, compared to their predecessors. Thus, they will both provide the means to increase the sample on high-spatial resolution observations of MYSOs.

LINC-NIRVANA will introduce wide field-of-view Fizeau interferometry as a new tool to the astrophysical community. The wide field-of-view, in conjunction with the high spatial resolution, will allow us, for example, to observe a statistically significant number of YSOs of the same age within young star clusters.

Bibliography

- Abuter, R., Rabien, S., Eisenhauer, F., et al. 2006, in Society of Photo-Optical Instrumentation Engineers (SPIE) Conference Series, Vol. 6268, Society of Photo-Optical Instrumentation Engineers (SPIE) Conference Series [13](#)
- Acke, B., Verhoelst, T., van den Ancker, M. E., et al. 2008, *Astron. & Astrophys.*, 485, 209 [52](#)
- Andrae, R. 2010, ArXiv e-prints, 1012.3754 [90](#), [91](#)
- Berger, J. P. & Segransan, D. 2007, *New Astronomy Reviews*, 51, 576 [51](#)
- Bertram, T. 2007, PhD thesis, Universität zu Köln [10](#), [11](#)
- Bertram, T., Eckart, A., Lindhorst, B., et al. 2008, in Society of Photo-Optical Instrumentation Engineers (SPIE) Conference, Vol. 7013, Society of Photo-Optical Instrumentation Engineers (SPIE) Conference Series [10](#), [18](#)
- Born, M. & Wolf, E. 1999, *Principles of Optics*, ed. Born, M. & Wolf, E. (Cambridge University Press) [3](#)
- Brix, M., Pott, J.-U., Bertram, T., et al. 2010, in Society of Photo-Optical Instrumentation Engineers (SPIE) Conference Series, Vol. 7734, Society of Photo-Optical Instrumentation Engineers (SPIE) Conference Series [11](#)
- Chini, R., Hoffmeister, V. H., Kämpgen, K., et al. 2004, *Astron. & Astrophys.*, 427, 849 [55](#), [56](#), [59](#), [62](#), [64](#), [66](#)
- Churchwell, E., Wolfire, M. G., & Wood, D. O. S. 1990, *Astrophys. J.*, 354, 247 [68](#)
- Conan, J.-M., Rousset, G., & Madec, P.-Y. 1995, *Journal of the Optical Society of America A*, 12, 1559 [1](#), [2](#), [3](#), [4](#)
- Dartois, E., d'Hendecourt, L., Thi, W., Pontoppidan, K. M., & van Dishoeck, E. F. 2002, *Astron. & Astrophys.*, 394, 1057 [77](#)
- de Bonis, F., Bertram, T., Labadie, L., et al. 2010, in Society of Photo-Optical Instrumentation Engineers (SPIE) Conference Series, Vol. 7735, Society of Photo-Optical Instrumentation Engineers (SPIE) Conference Series [46](#), [47](#)
- de Wit, W. J., Hoare, M. G., Oudmaijer, R. D., & Lumsden, S. L. 2010, *Astron. & Astrophys.*, 515, A45 [54](#), [63](#)
- de Wit, W. J., Hoare, M. G., Oudmaijer, R. D., et al. 2011, *Astron. & Astrophys.*, 526, L5 [77](#), [78](#), [79](#), [85](#)

- Di Francesco, J., Johnstone, D., Kirk, H., MacKenzie, T., & Ledwosinska, E. 2008, *Astrophys. J. Suppl*, 175, 277 [81](#)
- Draine, B. T. & Lee, H. M. 1984, *Astrophys. J.*, 285, 89 [90](#)
- Dullemond, C. P., Dominik, C., & Natta, A. 2001, *Astrophys. J.*, 560, 957 [72](#)
- Egan, M. P., Price, S. D., Kraemer, K. E., et al. 2003, *VizieR Online Data Catalog*, 5114, 0 [81](#)
- Eisenhauer, F., Perrin, G., Brandner, W., et al. 2011, *The Messenger*, 143, 16 [107](#)
- Follert, R., Herbst, T. M., Bizenberger, P., & de Bonis, F. 2010a, in *Society of Photo-Optical Instrumentation Engineers (SPIE) Conference Series*, Vol. 7734, *Society of Photo-Optical Instrumentation Engineers (SPIE) Conference Series* [12](#)
- Follert, R., Linz, H., Stecklum, B., et al. 2010b, *Astron. & Astrophys.*, 522, A17 [55](#), [56](#)
- Glindemann, A. 2011, *Principles of Stellar Interferometry*, ed. Glindemann, A. [1](#), [2](#), [4](#), [50](#)
- Grellmann, R., Ratzka, T., Kraus, S., et al. 2011, *Astron. & Astrophys.*, 532, A109+ [52](#)
- Hardy, J. W. 1998, *Adaptive Optics for Astronomical Telescopes*, ed. Hardy, J. W. [3](#)
- Harvey, P. M., Butner, H. M., Colomé, C., Di Francesco, J., & Smith, B. J. 2000, *Astrophys. J.*, 534, 846 [88](#)
- Helou, G. & Walker, D. W., eds. 1988, *Infrared astronomical satellite (IRAS) catalogs and atlases. Volume 7: The small scale structure catalog*, Vol. 7 [81](#)
- Henning, T., Friedemann, C., Guertler, J., & Dorschner, J. 1984, *Astronomische Nachrichten*, 305, 67 [55](#)
- Herbst, T. M., Ragazzoni, R., Eckart, A., & Weigelt, G. 2010, in *Society of Photo-Optical Instrumentation Engineers (SPIE) Conference Series*, Vol. 7734, *Society of Photo-Optical Instrumentation Engineers (SPIE) Conference Series* [10](#)
- Hoffmeister, V. H., Chini, R., Scheyda, C. M., et al. 2008, *Astrophys. J.*, 686, 310 [62](#)
- Hollenbach, D., Johnstone, D., Lizano, S., & Shu, F. 1994, *Astrophys. J.*, 428, 654 [50](#)
- Hollenbach, D. J., Yorke, H. W., & Johnstone, D. 2000, *Protostars and Planets IV*, 401 [50](#)
- Hosokawa, T. & Omukai, K. 2009, *Astrophys. J.*, 691, 823 [54](#), [85](#), [88](#), [106](#)
- Hosokawa, T., Yorke, H. W., & Omukai, K. 2010, *Astrophys. J.*, 721, 478 [85](#), [88](#)
- Isella, A. & Natta, A. 2005, *Astron. & Astrophys.*, 438, 899 [72](#)
- Ishihara, D., Onaka, T., Kataza, H., et al. 2010, *Astron. & Astrophys.*, 514, A1 [81](#)
- Jaffe, W. J. 2004, in *Society of Photo-Optical Instrumentation Engineers (SPIE) Conference*, Vol. 5491, *New Frontiers in Stellar Interferometry*, *Proceedings of SPIE Volume 5491*. Edited by Wesley A. Traub. Bellingham, WA: The International Society for Optical Engineering, 2004., p.715, ed. W. A. Traub, 715 [51](#), [58](#), [77](#)

- Kastner, J. H. & Weintraub, D. A. 1996, *Astrophys. J.*, 466, L103 [83](#), [97](#)
- Kastner, J. H., Weintraub, D. A., & Aspin, C. 1991, in *Bulletin of the American Astronomical Society*, Vol. 23, *Bulletin of the American Astronomical Society*, 1373 [76](#)
- Kastner, J. H., Weintraub, D. A., & Aspin, C. 1992, *Astrophys. J.*, 389, 357 [76](#), [84](#), [85](#), [88](#)
- Kastner, J. H., Weintraub, D. A., Snell, R. L., et al. 1994, *Astrophys. J.*, 425, 695 [76](#), [85](#)
- Kim, S.-H., Martin, P. G., & Hendry, P. D. 1994, *Astrophys. J.*, 422, 164 [61](#)
- Kleinmann, D. E. & Wright, E. L. 1973, *Astrophys. J.*, 185, L131 [55](#)
- Klessen, R. S. 2004, in *Revista Mexicana de Astronomia y Astrofisica*, vol. 27, Vol. 22, *Revista Mexicana de Astronomia y Astrofisica Conference Series*, ed. G. Garcia-Segura, G. Tenorio-Tagle, J. Franco, & H. W. Yorke , 8–12 [49](#)
- Knez, C., Boogert, A. C. A., Pontoppidan, K. M., et al. 2005, *Astrophys. J.*, 635, L145 [93](#)
- Kraus, S., Hofmann, K.-H., Menten, K. M., et al. 2010a, *Nature*, 466, 339 [51](#), [52](#), [53](#)
- Kraus, S., Hofmann, K.-H., Menten, K. M., et al. 2010b, in *Society of Photo-Optical Instrumentation Engineers (SPIE) Conference Series*, Vol. 7734, *Society of Photo-Optical Instrumentation Engineers (SPIE) Conference Series* [52](#)
- Kürster, M., Bertram, T., Borelli, J. L., et al. 2010, in *Society of Photo-Optical Instrumentation Engineers (SPIE) Conference*, Vol. 7734, *Society of Photo-Optical Instrumentation Engineers (SPIE) Conference Series* [7](#)
- Lada, C. J. 1987, in *IAU Symposium*, Vol. 115, *Star Forming Regions*, ed. M. Peimbert & J. Jugaku, 1–17 [50](#)
- Laor, A. & Draine, B. T. 1993, *Astrophys. J.*, 402, 441 [61](#)
- Leinert, C., Graser, U., Waters, L. B. F. M., et al. 2003, in *Interferometry for Optical Astronomy II. Proc. SPIE*, Vol. 4838, ed. W. A. Traub, 893–904 [51](#), [56](#), [77](#)
- Leinert, C., van Boekel, R., Waters, L. B. F. M., et al. 2004, *Astron. & Astrophys.*, 423, 537 [56](#), [77](#)
- Linz, H., Henning, T., Feldt, M., et al. 2009, *Astron. & Astrophys.*, 505, 655 [54](#), [60](#), [84](#), [85](#)
- Linz, H., Stecklum, B., Follert, R., et al. 2008, *Journal of Physics Conference Series*, 131 [51](#), [55](#), [101](#)
- Lopez, B., Antonelli, P., Wolf, S., et al. 2008, in *Society of Photo-Optical Instrumentation Engineers (SPIE) Conference Series*, Vol. 7013, *Society of Photo-Optical Instrumentation Engineers (SPIE) Conference Series* [107](#)
- Markwardt, C. B. 2009, in *Astronomical Society of the Pacific Conference Series*, Vol. 411, *Astronomical Society of the Pacific Conference Series*, ed. D. A. Bohlender, D. Durand, & P. Dowler, 251 [96](#)
- Martins, F., Schaerer, D., & Hillier, D. J. 2005, *Astron. & Astrophys.*, 436, 1049 [67](#)

- Masciadri, E., Stoesz, J., Hagelin, S., & Lascaux, F. 2010, *Mon. Not. R. Astron. Soc.*, 404, 144 [2](#)
- Men'shchikov, A. B. & Henning, T. 1997, *Astron. & Astrophys.*, 318, 879 [88](#)
- Meschke, D., Bizenberger, P., Gaessler, W., et al. 2010, in *Society of Photo-Optical Instrumentation Engineers (SPIE) Conference*, Vol. 7736, *Society of Photo-Optical Instrumentation Engineers (SPIE) Conference Series* [13](#), [45](#), [46](#)
- Millan-Gabet, R., Malbet, F., Akeson, R., et al. 2007, in *Protostars and Planets V*, ed. B. Reipurth, D. Jewitt, & K. Keil, 539 [67](#)
- Millour, F., Petrov, R. G., Vannier, M., & Kraus, S. 2008, in *Society of Photo-Optical Instrumentation Engineers (SPIE) Conference Series*, Vol. 7013, *Society of Photo-Optical Instrumentation Engineers (SPIE) Conference Series* [80](#)
- Minchin, N. R., Hough, J. H., Burton, M. G., & Yamashita, T. 1991, *Mon. Not. R. Astron. Soc.*, 251, 522 [76](#)
- Monnier, J. D., Tuthill, P. G., Ireland, M., et al. 2009, *Astrophys. J.*, 700, 491 [77](#), [78](#), [80](#), [81](#), [86](#), [89](#), [96](#), [97](#), [99](#), [104](#)
- Mueller, K. E., Shirley, Y. L., Evans, II, N. J., & Jacobson, H. R. 2002, *Astrophys. J. Suppl.*, 143, 469 [81](#), [83](#)
- Murakawa, K., Preibisch, T., Kraus, S., & Weigelt, G. 2008, *Astron. & Astrophys.*, 490, 673 [77](#), [97](#)
- Natta, A., Prusti, T., Neri, R., et al. 2001, *Astron. & Astrophys.*, 371, 186 [72](#)
- Pinte, C., Padgett, D. L., Menard, F., et al. 2008, *ArXiv e-prints* [65](#), [88](#)
- Porter, J. M., Drew, J. E., & Lumsden, S. L. 1998, *Astron. & Astrophys.*, 332, 999 [55](#), [56](#), [64](#), [66](#), [75](#)
- Ragazzoni, R. 1995, "Journal of Modern Optics" [3](#)
- Ratzka, T., Schegerer, A. A., Leinert, C., et al. 2009, *Astron. & Astrophys.*, 502, 623 [101](#)
- Reimann, H., Linz, H., Wagner, R., et al. 2000, in *Society of Photo-Optical Instrumentation Engineers (SPIE) Conference Series*, Vol. 4008, *Society of Photo-Optical Instrumentation Engineers (SPIE) Conference Series*, ed. M. Iye & A. F. Moorwood, 1132–1143 [58](#)
- Robitaille, T. P. 2008, in *Astronomical Society of the Pacific Conference Series*, Vol. 387, *Massive Star Formation: Observations Confront Theory*, 290 [60](#)
- Robitaille, T. P., Whitney, B. A., Indebetouw, R., & Wood, K. 2007, *Astrophys. J. Suppl.* [59](#), [60](#), [66](#), [75](#), [84](#), [106](#)
- Robitaille, T. P., Whitney, B. A., Indebetouw, R., Wood, K., & Denzmore, P. 2006, *Astrophys. J. Suppl.*, 167, 256 [54](#), [60](#), [61](#), [73](#), [74](#), [83](#), [86](#), [89](#)
- Siebenmorgen, R., Krügel, E., & Spoon, H. W. W. 2004, *Astron. & Astrophys.*, 414, 123 [59](#)
- Skrutskie, M. F., Cutri, R. M., Stiening, R., et al. 2006, *Astrophys. J.*, 131, 1163 [81](#)

- Sloan, G. C., Kraemer, K. E., Price, S. D., & Shipman, R. F. 2003, *Astrophys. J. Suppl.*, 147, 379 [81](#)
- Tannirkulam, A., Harries, T. J., & Monnier, J. D. 2007, *Astrophys. J.*, 661, 374 [72](#)
- Tatarskii, V. I. 1971, The effects of the turbulent atmosphere on wave propagation. [1](#)
- van Boekel, R., Waters, L. B. F. M., Dominik, C., et al. 2003, *Astron. & Astrophys.*, 400, L21 [91](#)
- van der Tak, F. F. S., van Dishoeck, E. F., Evans, II, N. J., & Blake, G. A. 2000, *Astrophys. J.*, 537, 283 [81](#)
- Weigelt, G., Grinin, V. P., Groh, J. H., et al. 2011, *Astron. & Astrophys.*, 527, A103 [51](#), [52](#)
- Whitney, B. A., Wood, K., Bjorkman, J. E., & Cohen, M. 2003a, *Astrophys. J.*, 598, 1079 [60](#), [61](#), [62](#), [63](#), [75](#), [96](#)
- Whitney, B. A., Wood, K., Bjorkman, J. E., & Wolff, M. J. 2003b, *Astrophys. J.*, 591, 1049 [51](#), [52](#), [54](#), [96](#), [102](#)
- Wu, Y., Zhang, Q., Yu, W., et al. 2006, *Astron. & Astrophys.*, 450, 607 [84](#)
- Zinnecker, H. & Yorke, H. W. 2007, *Annu. Rev. Astro. Astrophys.*, 45, 481 [49](#), [50](#)

Abbreviations

AD card	Analog - to - Digital converter card
AGB	Asymptotic Giant Branch
AIV	Assembly, Integration, Verification
AMBER	Astronomical Multi - BEam combineR
AO	Adaptive Optics
AT	Auxiliary Telescope
ELT	Extremely Large Telescope
EO-PM	Electro - Optical Phase Modulators
EON	East Of North
FC/PC	optical fiber connector type, FC/ Physical Contact
FWHM	Full Width at Half Maximum
GWS	Groundlayer Wavefront control Sensor
IDL	Interactive Data Language
IRAC	Infra Red Array Camera
IRS	Infra Red Spectrograph
LBC	Large Binocular Camera
LBT	Large Binocular Telescope
LBTI	Large Binocular Telescope Interferometer
LED	Light Emitting Diode
LINC - NIRVANA	LBT INterferometric Camera - Near - InfraRed / Visible Adaptive INterferometer for Astronomy
Luci or LUCIFER	LBT near - infrared spectroscopic Utility with Camera and Integral Field unit for Extragalactic Research
MAPS	Multi - Atmospheric Phase screen and Stars
mas	milli - arcsecond
MATISSE	Multi AperTure mid - Infrared SpectroScopic Experiment
MCAO	Multi - Conjugate Adaptive Optics
MCRT	Monte Carlo Radiative Transfer
MIDI	MID - infrared Interferometric instrument
MIR	Mid - InfraRed
MODS	Multi - Object Double Spectrograph
MYSO	Massive Young Stellar Object
NIR	Near - InfraRed
OPD	Optical Path Difference
OVMS	OPD and Vibration Monitoring System
PEPSI	Potsdam Echelle Polarimetric and Spectroscopic Instrument
PM fibers	Polarization Maintaining fibers
PSF	Point Spread Function
RGB	Red - Green - Blue

ROI	R egion O f I nterest
SDK	S oftware D evelopment K it
SED	S pectral E nergy D istribution
UT	U nit T elescope
VLTI	V ery L arge T elescope I nterferometer
YSO	Y oung S tellar O bject

Acknowledgments

First, I would like to thank Tom Herbst. You gave me the opportunity to come to the MPIA and to work on this wonderful project. Your door was always open and you had the time and patience to explain all those things to me. Thank you.

Next, I would like to thank Hendrik Linz, Roy van Boekel and Bringfried Stecklum for helping me through the struggles in my scientific everyday life. You taught me a lot on interferometry, young stars and how find out about the latter by help of the other. You were great co-authors, too.

I would like to thank the whole team of LINC-NIRVANA at the MPIA as well as all our colleagues in Italy. You were always around when something didn't work in the lab. In particular I want to thank Peter Bizenberger for his support with the optical setup, Frank Kittmann, Udo Neumann, Florian Briegel, Jürgen Berwein and Clemenz Storz for helping me tame the Linux beast and making the computer hardware work. Thanks to Lars Mohr and the MPIA electronics workshop for realizing my ideas of the control electronics in a professional way. Thanks to Fulvio DeBonis for helping me designing some of the opto-mechanics and the MPIA mechanics workshop for producing them. And of course thanks to Thomas Bertram and Jörg Uwe Pott for many the discussions on working in the lab in general and on the project in particular. It was a pleasure...

I would like to thank Hans-Walter Rix and Andreas Quirrenbach for refereeing this thesis as well as Hans-Walter Rix, Andreas Quirrenbach, Bernd Jähne and Andreas Glindemann for agreeing to be part of my examination committee.

Many, many thanks to Tom Herbst, Hendrik Linz and Thomas Bertram for reading this thesis although they had many other things to do. You provided me with so many helpful comments, which made the thesis what it is now.

Last but not least, I would like to thank my family and all my friends, who joined me on this long journey. My family for always keeping their faith in me and always supporting me in so many ways. And my friends for not giving up on me and helping and encouraging me during hard times.

If I forgot anyone, don't worry. You know how bad I am with names, so thanks to you, too. Finally, thanks again to everybody, for the wonderful time.

Danksagung

Zunächst möchte ich Tom Herbst danken, dafür, dass er mir die Möglichkeit gegeben hat zum MPIA zu kommen und an diesem wundervollen Projekt zu arbeiten. Deine Tür war immer offen für mich und du hast dir immer die Zeit genommen, mir alles mögliche zu erklären. Danke dafür.

Als nächstes möchte ich Hendrik Linz, Roy van Boekel und Bringfried Stecklum danken dafür danken, dass sie mich durch die Wirren meines wissenschaftlichen Alltags geführt haben. Ihr habt mir viel über Interferometrie, junge Sterne und wie man letztere durch ersteres erforschen kann beigebracht. Außerdem wart ihr großartige Koautoren.

I möchte dem ganzen LINC-NIRVANA Team am MPIA sowie unseren Kollegen aus Italien danken. Ihr wart immer da, wenn irgend etwas im Labor nicht funktioniert hat. Im Besonderen möchte ich Peter Bizenberger für seine Unterstützung bei den Optiken danken, Frank Kittmann, Udo Neumann, Florian Briegel, Jürgen Berwein und Clemenz Storz dafür, dass mir geholfen haben, das Linux Biest zu besänftigen und die Computer Hardware zum Laufen zu kriegen. Dank an Lars Mohr und die Elektronik Werkstatt des MPIA, dafür, dass sie mir geholfen haben, meine Ideen der Kontrollelektronik auf professionelle Art und Weise umzusetzen. Dank an Fulvio DeBonis für seine Hilfe beim Design einiger opto-mechanischer Komponenten und Dank an die Feinmechanikwerkstatt, die die Designs umgesetzt hat. Und natürlich vielen Dank an Thomas Bertram und Jörg Uwe Pott für die vielen Diskussionen um die Laborarbeit im Allgemeinen und mein Projekt im Speziellen. Es war mir eine Ehre, meine Herren...

I möchte Hans-Walter Rix und Andreas Quirrenbach für die Begutachtung dieser Dissertation danken. Weiterhin danke ich Hans-Walter Rix, Andreas Quirrenbach, Bernd Jähne and Andreas Glindemann dafür, Teil meines Prüfungskomitees zu sein.

Vielen, vielen Dank im besonderen an Tom Herbst, Hendrik Linz und Thomas Bertram. Ihr habt euch die Zeit genommen, diese Arbeit zu lesen, obwohl ihr sicher genügend andere Dinge zu tun hattet. Eure vielfältigen Kommentare haben diese Arbeit erst zu dem werden lassen, was sie jetzt ist.

Zu guter Letzt möchte ich meiner Familie und all meinen Freunden danken. Danken dafür, dass ihr mich auf dieser langen Reise begleitet habt. Meiner ganzen Familie, meinen Eltern, meinen Geschwistern, meinen Großeltern, Tanten & Cousins möchte ich dafür danken, dass sie nie den Glauben in mich und das was ich tue verloren haben. Ihr habt mich immer unterstützt, auf die ein oder andere Weise. Danke. Und meinen Freunden Dank dafür, dass ihr mich nie aufgegeben habt, auch wenn ich das ein oder andere Mal ein wenig schwierig war. Dank auch dafür, dass ihr mich immer wieder in schweren Zeiten in meiner Sache bestärkt habt.

Sollte ich jemanden hier vergessen haben, ihr wisst wie schlecht mein Namensgedächtnis ist. Verzeiht, und dank auch euch.

Schließlich und schlussendlich nocheinmal Dank an alle, danke für die schöne Zeit.